

**AN UNDERSTANDING OF EJECTOR FLOW PHENOMENA FOR  
WASTE HEAT DRIVEN COOLING**

A Dissertation  
Presented to  
The Academic Faculty

by

Adrienne Blair Little

In Partial Fulfillment  
of the Requirements for the Degree  
Doctor of Philosophy in Mechanical Engineering

Georgia Institute of Technology  
December 2015

Copyright © 2015 by Adrienne B. Little

# AN UNDERSTANDING OF EJECTOR FLOW PHENOMENA FOR WASTE HEAT DRIVEN COOLING

Approved by:

Dr. Srinivas Garimella, Advisor  
G. W. Woodruff School of Mechanical  
Engineering  
*Georgia Institute of Technology*

Dr. Laurence Jacobs  
School of Civil and Environmental  
Engineering  
*Georgia Institute of Technology*

Dr. Sheldon Jeter  
G. W. Woodruff School of Mechanical  
Engineering  
*Georgia Institute of Technology*

Dr. Yann Bartosiewicz  
Institute of Mechanics, Materials, and  
Civil Engineering  
*Université catholique de Louvain*

Dr. Caroline Genzale  
G. W. Woodruff School of Mechanical  
Engineering  
*Georgia Institute of Technology*

Date Approved: September 21, 2015

*To all of those who are the change they want to see in the world.*

## ACKNOWLEDGEMENTS

I would like to thank the wide network of colleagues and friends at Georgia Tech for their invaluable support during the completion of this work. Thank you to my Ph.D. committee members for their time and thoughtful comments on this dissertation, specifically Dr. Yann Bartosiewicz for hosting me at the Université catholique de Louvain to establish the foundation of this work. Many thanks to Dr. William Wepfer for opening up countless opportunities for me both inside and outside of Georgia Tech. Thank you to Drs. Vicki Birchfield and Seymour Goodman in the Sam Nunn School of International Affairs for adding context and direction to my studies in engineering. Thank you to Steven Sheffield and Louis Boulanger in the ME Machine Shop for their manufacturing expertise. Thank you to Jaime Zahorian, Scott Bair, George Woo, Andrea Marcon, Ianko Chtereov, and Federico Mazzelli for providing critical technical advice at the most challenging points in my Ph.D. Thank you to those at STSL who exhibit excellent work ethic and drive to make a difference, specifically Brian Fronk, Alex Rattner, and Marcel Staedter for countless stimulating chats on subjects technical and otherwise. Thank you to friends old and new who have kept me sane during a long Ph.D.: Daudi Jjingo, Anton Souslov, Kellie Dixon, Nathan Mayercsik, and Panagiotis Antoniadis. Thank you to my father, Gary Little. Above all, I would like to thank my mother, Pamela Little, who gave me the essential foundation I needed to make it here.

I would like to give my deepest thanks to my adviser, Dr. Srinivas Garimella, for providing constant and invaluable guidance in all things technical, professional, and aspirational throughout the entire length of my Ph.D. I look forward to our collaboration and interactions in the years to come.

# TABLE OF CONTENTS

ACKNOWLEDGEMENTS	iv
LIST OF TABLES	ix
LIST OF FIGURES	xi
LIST OF SYMBOLS AND ABBREVIATIONS	xv
SUMMARY	xviii
CHAPTER 1: INTRODUCTION	1
1.1 Motivation	1
1.2 Background	2
1.2.1 Ejector Pump	2
1.3 Ejector-Based Chiller	14
1.4 Organization of Thesis	16
CHAPTER 2: A CRITICAL REVIEW LINKING EJECTOR FLOW PHENOMENA WITH COMPONENT- AND SYSTEM-LEVEL PERFORMANCE	19
2.1 Ejector History and Previous Reviews	19
2.1.1 Early History	19
2.1.2 Previous reviews of ejector work	20
2.2 Ejector Component Modeling	25
2.2.1 Analytical studies	25
2.2.2 Numerical studies	36
2.2.3 Visualization studies	44
2.3 Ejector Systems	46
2.3.1 Ejector-based chillers	46
2.3.2 Ejector-based chiller configuration variations	50

2.3.3 Passive Systems	53
2.4 Future Work	61
2.4.1 Understanding and Modeling Shock Phenomena	61
2.4.2 Two-Phase Flow	62
2.5 Conclusions	63
<b>CHAPTER 3: VISUALIZATION AND VALIDATION OF EJECTOR FLOW FIELD WITH COMPUTATIONAL AND FIRST-PRINCIPLES ANALYSIS</b>	<b>67</b>
3.1 Introduction	68
3.2 Experimental Approach	69
3.3 Computational Modeling	73
3.4 Analytical modeling	77
3.5 Results and Discussion	85
3.5.1 Comparison of Global Flow Features	85
3.5.2 Comparison of Local Flow Features	87
3.6 Conclusions	96
<b>CHAPTER 4: SHADOWGRAPH VISUALIZATION OF CONDENSING R134A FLOWS THROUGH EJECTORS</b>	<b>100</b>
4.1 Introduction	100
4.2 Experimental Approach	103
4.2.1 Ejector-Based Chiller	103
4.2.2 Transparent Ejector Test Section	104
4.2.3 Shadowgraph Flow Visualization	107
4.3 Modeling and Data Reduction	110
4.3.1 Analytical Model	110

4.3.2 CFD Model	114
4.4 Results and Discussion	114
4.4.1 Effect of condensation on MER	114
4.4.2 Analytical model performance	116
4.4.3 Numerical model performance	120
4.5 Conclusions	121
<b>CHAPTER 5: COMBINED EFFECTS OF FLUID SELECTION AND FLOW CONDENSATION ON EJECTOR OPERATION IN AN EJECTOR-BASED CHILLER</b>	<b>123</b>
5.1 Introduction	123
5.2 Experimental Approach	125
5.3 Analytical Modeling	129
5.3.1 Motive Nozzle Analysis	129
5.3.2 Control Volume Analysis	134
5.4 Results and Discussion	141
5.4.1 Motive Jet Properties	143
5.4.2 Maximum Jet Power	149
5.4.3 Effect of Fluid Type	151
5.4.4 Effect of Phase Change	155
5.5 Conclusions	161
<b>CHAPTER 6: CONCLUSIONS AND RECOMMENDATIONS</b>	<b>164</b>
6.1 Recommendations for Future Work	166
<b>APPENDIX A: Shadowgraph Visualization Setup Instructions</b>	<b>169</b>
A.1 Attach components to optics rail	170

A.2 Set up concentrated point light source	170
A.3 Find correct position of plano-convex lens	171
A.4 Camera placement	172
A.5 Insert cube beam splitter	172
A.6 Checking for image distortion	172
A.7 Checking for image resolution and optical aberration	173
APPENDIX B: EJECTOR-BASED CHILLER OPERATIONAL PROCEDURES	176
B.1 Test Facility Charging	176
B.2 Operational Procedure	177
B.3 Data Point Capture	178
APPENDIX C: SAMPLE CALCULATION AND UNCERTAINTY ANALYSIS	179
C.1 Motive Nozzle Inlet Enthalpy	179
C.2 Ejector Component Heat Loss	182
C.3 Uncertainty Analysis	182
C.4 Cycle State Point Calculations	183
APPENDIX D: NUMERICAL MODEL CONSIDERATIONS	186
D.1 Mesh Development	186
D.2 Three-Dimensional Flow Effects	188
D.3 Unsteady Flow Effects	188
REFERENCES	189



## LIST OF TABLES

	Page
Table 1.1: Candidate fluids for ejector-based chiller.	11
Table 2.1: Overview of previous review papers and key contributions.	22
Table 2.2: Component-level analytical modeling studies and key contributions.	33
Table 2.3: CFD studies of ejector flow phenomena.	43
Table 2.4: System-level studies. Source and cooling temperatures, as well as operational COP values are given for each study, along with key contributions.	58
Table 3.1: Description and position of each measurement taken on ejector test facility with corresponding exact value measured under experimental conditions. These values are the boundary conditions used for all presented CFD models.	74
Table 3.2: Flow conditions taken from CFD flow field and used to define correction coefficients. Locations at which properties are taken are indicated in the bottom graph of Fig. 3.6.	80
Table 3.3: Comparison of CFD and experimental values for global parameters of motive and suction mass flow rates.	85
Table 3.4: Correction coefficients used to match idealized first-principles analysis to flow conditions identified in Table 3.2. Values in parentheses represent the change in coefficient caused by a $\pm 5\%$ change in the flow property to which the coefficient corresponds.	93
Table 4.1: Experimental motive inlet conditions and resulting MER values. Motive inlet enthalpy is calculated using measured $T$ and $P$ for superheated conditions, and an energy balance about the boiler for saturated conditions.	108
Table 4.2: Comparison of experimentally measured back pressure values to those predicted by analytical and CFD models.	117
Table 5.1: Tabulated experimental results for ejector-based chiller operation with R134a for different degrees of superheat at the motive nozzle inlet. Change in COP and realized cooling load can be seen to change with the degree of superheat, with the peak value of COP being 0.153. COP values are presented graphically at the top of Fig. 5.5.	129

Table 5.2: Tabulated experimental results for ejector-based chiller operation with R245fa for different degrees of superheat at the motive nozzle inlet. Change in COP and realized cooling load can be seen to change with the degree of superheat, with the peak value of COP being 0.160. COP values are presented graphically at the bottom of Fig. 5.5. 130

Table 5.3: Motive jet properties at outlet of motive nozzle operating with R134a. Density values indicated as ‘wet’ calculated as average of liquid and vapor fractions. Speed of sound for frozen flow model is approximated as  $c=\sqrt{\gamma RT}$ . Starred values are the conditions expected based on the analysis in Section 5.4.1.2. 149

Table 5.4: Motive jet properties at outlet of motive nozzle operating with R245fa. Density values indicated as ‘wet’ calculated as average of liquid and vapor fractions. Speed of sound for frozen flow model is approximated as  $c=\sqrt{\gamma RT}$ . Starred values are the conditions expected based on the analysis in Section 5.4.1.2. 150

Table C.1: Piping heat loss values from the temperature measurement location at the boiler inlet to the motive nozzle inlet for the lowest superheat condition in Table 5.1 (Row 5). 181

Table C.2: Sample state point calculations for saturated condition given in last row of Table 5.1 for the R134a test matrix in Chapter 5. 184

## LIST OF FIGURES

	Page
Figure 1.1: Schematic of ejector with corresponding qualitative pressure and velocity profiles, adapted from Srisastra and Aphornratana (2005).	3
Figure 1.2: Schematic of motive jet geometry.	7
Figure 1.3: Qualitative $T$ - $s$ diagrams for (a) wet and (b) dry fluids.	9
Figure 1.4: Qualitative ejector characteristic curve at a set motive and suction inlet pressure. On- and off-design regions are labeled, as well as the critical point at the threshold between these two regions.	12
Figure 1.5: (a) Schematic of the ejector-based chiller cycle and (b) qualitative $P$ - $h$ diagrams with cycle state points indicated for dry and wet jet operation with wet fluid.	15
Figure 2.1: (a) Schematic of a double cascaded-ejector setup, and (b) the resulting composite operating curve as a superposition of the MER vs. outlet pressure graph for each ejector.	52
Figure 2.2: Comparison of ejector-based chillers studies including boosted, bottoming VC, and passive systems derivatives. Lift is defined as the difference between condenser (ambient) and evaporator (cooling) temperatures. Studies are color-coded based on the boiler (source) temperature used. In some cases, the peak COP is reported, and in others a range of conditions is given as part of a parametric study.	56
Figure 3.1: (a) Photograph of the visualization section, and (b) dimensioned drawing of same section showing exact 3D geometry of motive nozzle, suction nozzle, mixing section, and diffuser. Dotted line in (b) indicates the area available for visualization. Shaded areas indicate the computational domain and region visualized in shadowgraph images.	70
Figure 3.2: Schematic of overall system indicating locations of pressure and temperature measurements, and orifice plates for flow rate measurement. Inset shows schematic of shadowgraph visualization setup.	72
Figure 3.3: Experimental characteristic curve of ejector operation for $P_{\text{motive}} = 3.5$ bar and $P_{\text{suction}} = 1$ bar shown by dotted line. Diamond-shaped data points indicate MER values for CFD simulations for the one on-design and one off-design condition considered for comparison in this study.	75

Figure 3.4: Centerline static pressure vs. axial position for  $k$ - $\epsilon$  turbulence model. An ~18% increase in the number of elements shows negligible change in the solutions. 76

Figure 3.5: Centerline static pressure vs. axial position for  $k$ - $\omega$  turbulence model. An ~18% increase in the number of elements shows negligible change in the solutions. 77

Figure 3.6: (Top) Image from off-design CFD simulation ( $P_{\text{motive}} = 3.5$  bar,  $P_{\text{suction}} = 1$  bar, and  $P_{\text{outlet}} = 1.5$  bar) using  $k$ - $\epsilon$  RNG turbulence model indicating Region locations. (Middle) Schematic used for analytical model, identifying important geometric values. (Bottom) Graph shows contours of static pressure along the motive jet center and jet boundary, indicating specific points where data were taken for States 3 through 6 in Table 3.2. 79

Figure 3.7: Experimental image and CFD data for on-design condition with  $P_{\text{motive}} = 3.5$  bar,  $P_{\text{suction}} = 1$  bar, and  $P_{\text{outlet}} = 1.2$  bar. Visual comparison using contours produced by  $k$ - $\epsilon$  RNG turbulence model. Bottom graph shows static pressure along ejector central axis, comparing values for  $k$ - $\epsilon$  RNG to  $k$ - $\omega$  SST data. Three major flow features are indicated at  $x = -22.6$  mm (expansion),  $x = -13.0$  mm (compression), and  $x = -5.8$  mm (expansion). 88

Figure 3.8: Experimental image and CFD data for off-design condition with  $P_{\text{motive}} = 3.5$  bar,  $P_{\text{suction}} = 1$  bar, and  $P_{\text{outlet}} = 1.5$  bar. Visual comparison using contours produced by  $k$ - $\epsilon$  RNG turbulence model. Bottom graph shows static pressure along ejector central axis, comparing values for  $k$ - $\epsilon$  RNG to  $k$ - $\omega$  SST data. Three major flow features are indicated at  $x = -22.6$  mm (expansion),  $x \approx -13.2$  mm (compression), and  $x \approx -7.1$  mm (expansion). 92

Figure 4.1: Schematic of motive jet geometry. Green lines indicate a compression shock and red lines indicate expansion waves. Pressure across the jet boundary is constant such that  $P_{\text{back}} = P_{\text{suction outlet}}$ . Inset shows the decomposition of the motive flow velocity vector with respect to the first shock at angle  $\theta$ . 102

Figure 4.2: Schematic of ejector-based chiller test facility used to provide desired inlet and outlet conditions to transparent ejector test section. Motive flow enters the ejector at state 1, and suction flow enters at state 7. Locations of temperature,  $T$ , pressure,  $P$ , and mass flow rate. 104

Figure 4.3: Schematic of ejector plate showing ejector geometry and the area of interest for visualization highlighted. All dimensions are in mm. 105

Figure 4.4: Exploded view of transparent ejector test section showing major components (front plate, back plate, ejector plate) and minor components (mirror, sight/window, gaskets). Motive and suction inlet ports are indicated in the back plate where suction inlet is split in two to maintain flow symmetry. Outlet flow port is also shown in back plate. 106

- Figure 4.5: Photographs of assembled transparent ejector test section, designed specifically for undistorted flow visualization of high temperature and high pressure refrigerant flows. 107
- Figure 4.6: Schematic of shadowgraph visualization setup. Major visualization components include a condensed light source, plano-convex lens, flat mirror within the ejector test section, cube beam splitter, and high-speed camera with magnification lens. 109
- Figure 4.7: Sample set of ejector test section images showing (a) raw image with zero flow, (b) raw image with flow, and (c) corrected image with flow. 111
- Figure 4.8: Images of ejector flow at decreasing motive inlet superheat with experimental values of MER. Motive nozzle outlet quality values according to the equilibrium analytical model are also given. Exact flow conditions can be found in Table 4.1. 115
- Figure 4.9: Comparison of first three superheat conditions with clear motive jet flow features. Dotted lines indicate angles measured for analytical and CFD analyses, given in Table 4.2. 118
- Figure 5.1: Photograph of ejector-based chiller test facility with major components labeled. 126
- Figure 5.2: Schematic of ejector geometry used for experiments with (a) R134a and (b) R245fa. All dimensions are in mm. 127
- Figure 5.3: Experimental state points for (a) R134a and (b) R245fa plotted on a  $T-h$  diagram. Red, blue, green, and pink points indicate the locus of states for the motive nozzle inlet, motive nozzle outlet, ejector outlet, and suction inlet states, respectively. The test matrix starts with right-most points at the highest motive inlet enthalpy and superheat. All ejector outlet conditions are maintained at the same pressure. 128
- Figure 5.4: (a) CV of whole ejector, (b) CV of motive jet flow only with zero mass flux boundary. 135
- Figure 5.5: Experimental change in COP vs. motive inlet enthalpy for (a) R134a and (b) R245fa. The degree of superheat for each superheated data point is indicated in data labels. System shows peak performance at saturated inlet conditions for both fluids. 142
- Figure 5.6: Predicted variation in (top) density, (middle) temperature, and (bottom) pressure for R134a (left) and R245fa (right) near motive nozzle throat for the highest superheat case. Comparison is made between analytical frozen and equilibrium flow models as well as 2D CFD simulation in ANSYS FLUENT. 144

Figure 5.7: Results from 1D analytical models for (a) R134a and (b) R245fa. Flow conditions transition from frozen flow conditions to equilibrium flow conditions across a condensation shock.	147
Figure 5.8: Plots of MER and MER <sub>max</sub> for (a) R134a and (b) R245fa.	153
Figure 5.9: MER/MER <sub>max</sub> for (a) R134a and (b) R245fa.	154
Figure 5.10: Plots of normalized exergy destroyed, $\dot{X}_{destroyed} / (\dot{m}_m h_m)$ , for (a) R134a and (b) R245fa.	156
Figure 5.11: Plots of $\dot{W}_{jet}$ and $\dot{Q}_{jet}$ for (a) R134a and (b) R245fa.	157
Figure 5.12: Plots of $\dot{W}_{jet}$ normalized by the total energy needed to drive the suction flow at maximum entrainment conditions, $\dot{W}_{jet} / (\dot{m}_{s,max} (h_o - h_s))$ , for (a) R134a and (b) R245fa.	158
Figure 5.13: Plots of quality at the motive nozzle inlet, motive nozzle outlet, and ejector outlet for (a) R134a and (b) R245fa.	159
Figure A.1: Sample precision alignment of optical components using laser guide. Dotted red line shows sample optical blurring effect that would occur from an imperfection in the flat mirror component.	174
Figure A.2: Sample optical aberration effect where a given flow feature (left) would be blurred (right). While this may lead to errors in measurement of the width of the flow feature, measuring the feature angle is not affected appreciably.	174
Figure D.1: Sample mesh at the exit of the motive nozzle for the ejector from Chapter 3 operating with air in a rectangular cross-section ejector. Conditions are $P_{motive} = 3.5$ bar, $P_{suction} = 1$ bar, and $P_{outlet} = 1.2$ bar using the $k-\epsilon$ RNG turbulence model. Mesh includes $\sim 108$ k elements, and the maximum face area is $7.5E-3$ m <sup>2</sup> .	187

## LIST OF SYMBOLS AND ABBREVIATIONS

### Symbols

$A_c$	Cross-sectional area ( $\text{m}^2$ )
$A_s$	Surface area ( $\text{m}^2$ )
$a$	Speed of sound ( $\text{m s}^{-1}$ )
$COP$	Coefficient of Performance (-)
$c_p$	Specific heat at constant pressure ( $\text{J kg}^{-1} \text{K}^{-1}$ )
$Gr$	Grashof number (-)
$h$	Specific enthalpy ( $\text{J kg}^{-1}$ )
$M$	Mach number (-)
$\dot{m}$	Mass flow rate ( $\text{kg s}^{-1}$ )
$MER$	Mass Entrainment Ratio (-)
$P$	Pressure (Pa)
$Pr$	Prandtl number (-)
$\dot{Q}$	Heat transfer rate (W)
$R$	Gas constant ( $\text{J kg}^{-1} \text{K}^{-1}$ )
$s$	Specific entropy ( $\text{J kg}^{-1} \text{K}^{-1}$ )
$\dot{S}_{gen}$	Entropy generation rate ( $\text{W K}^{-1}$ )
$SPR$	Suction Pressure Ratio (-)
$T$	Static temperature (K)
$UA$	Overall heat transfer coefficient multiplied by heat transfer surface area ( $\text{W K}^{-1}$ )
$V$	Velocity ( $\text{m s}^{-1}$ )
$\dot{W}$	Work (W)
$x$	Quality (-)

Z Z-Factor (-)

### **Greek Letters**

$\alpha$  Flow direction angle with respect to horizontal (deg)

$\gamma$  Specific heat ratio (-)

$\eta$  Efficiency (-)

$\mu$  Mach wave angle with respect to the horizontal (deg),  
dynamic viscosity ( $\text{N s m}^{-2}$ )

$\nu$  Turning angle with respect to the initial flow direction  
(deg)

$\rho$  Density ( $\text{kg m}^{-3}$ )

$\theta$  Shock angle with respect to the horizontal (deg)

$\Psi_M$  Correction factor for Mach number (-)

$\Psi_P$  Correction factor for static pressure (-)

$\Psi_T$  Correction factor for static temperature (-)

$\sigma$  Stefan-Boltzmann constant ( $\text{W m}^{-2} \text{K}^{-4}$ )

$\tau$  Shear stress ( $\text{N m}^{-2}$ )

### **Subscripts and Superscripts**

3,4,5,6 Motive jet region labels

amb Ambient

avg Average

ext External

fg Enthalpy of vaporization

i Ideal state

K Boundary



m	Motive inlet
n	Normal component of velocity vector
o	Ejector outlet
s	Suction inlet
sat	Saturation
sup	Superheat
t	Tangent component of velocity vector
tot	Total pressure or total temperature
total	Total

#### **Abbreviations**

CFD	Computational Fluid Dynamics
LES	Large Eddy Simulation
RSM	Reynolds Stress Model
VC	Vapor Compression cycle

## SUMMARY

In an attempt to reduce the dependence on fossil fuels, a variety of research initiatives has focused on increasing the efficiency of conventional energy systems. One such approach is to use waste heat recovery to reclaim energy that is typically lost in the form of dissipative heat. An example of such reclamation is the use of waste heat recovery systems that take low-temperature heat and deliver cooling in space-conditioning applications. In this work, an ejector-based chiller driven by waste heat will be studied from the system to component to sub-component levels, with a specific focus on the ejector. The ejector is a passive device used to compress refrigerants in waste heat driven heat pumps without the use of high grade electricity or wear-prone complex moving parts. With such ejectors, the electrical input for the overall system can be reduced or eliminated entirely under certain conditions, and package sizes can be significantly reduced, allowing for a cooling system that can operate in off-grid, mobile, or remote applications. The performance of this system, measured typically as a coefficient of performance, is primarily dependent on the performance of the ejector pump. This work uses analytical and numerical modeling techniques combined with flow visualization to determine the exact mechanisms of ejector operation, and makes suggestions for ejector performance improvement. Specifically, forcing the presence of two-phase flow has been suggested as a potential tool for performance enhancement. This study determines the effect of two-phase flow on momentum transfer characteristics inside the ejector while operating with refrigerants R134a and R245fa. It is found that reducing the superheat at motive nozzle inlet results in a 12-13% increase in COP with a 14-16 K decrease in driving waste heat temperature. The mechanisms of this improvement are found to be a combination of two

effects: the choice of operating fluid (wet vs. dry) and the effect of two-phase flow on the effectiveness of momentum transfer. It is recommended that ejector-based chillers be operated such that the motive nozzle inlet is near saturation, and environmentally friendly dry fluids such as R245fa be used to improve performance. This work provides critical methods for ejector modeling and validation through visualization, as well as guidance on measures to improve ejector design with commensurate beneficial effects on cooling system COP.

# CHAPTER 1

## INTRODUCTION

As worldwide electricity demand increases and stresses electricity grids to the point of collapse, energy-saving devices have assumed increasing importance for demand-side management. To reduce the use of high-grade electrical energy, waste heat recovery systems are increasingly considered for applications in air conditioning and refrigeration. The drawback of many waste heat recovery systems is the unfortunate combination of large components and low efficiencies, mostly due to the low waste heat temperatures used  $\leq 150^{\circ}\text{C}$ . The ejector-based chiller considered in this work mitigates these issues by offering a solution that is scalable, and has operational and mechanical simplicity. It replaces a large and complex compressor component with an ejector pump, and does so using a pure, non-toxic refrigerant with low global warming potential. It obviates the need for lubricating oils, maintenance, or expensive repairs, and allows for waste heat recovery in previously inaccessible applications, including the mobile and/or remote applications that are characteristic of waste heat recovery applications. The heart of the ejector-based chiller is the ejector component itself. This work investigates the ejector on a fundamental level, exploring the nuances of flow inside the ejector in an effort to improve its efficiency and related performance of the ejector-based chiller as a whole.

### 1.1 Motivation

Ejector-based chillers have long been studied and developed for their utility as simple devices that can produce cooling from commonly available waste heat sources. The COP of a basic ejector-based chiller is typically low, between 0.2 and 0.6. While this depends

on the waste heat, ambient, and desired cooling temperatures, the COP also depends heavily on the performance of the ejector pump. As such, development of the ejector has the most potential to increase the system performance. Unfortunately, detailed understanding of the ejector has been challenging because of the underlying complex flow phenomena, to the point that various investigators have described ejector design and operation as more of an art than a science. This work attempts to shed light on these flow phenomena.

It has been hypothesized that two-phase flow in the ejector at some operational conditions can be used to passively change momentum transfer characteristics by augmenting losses within the ejector. This work will focus specifically on the two-phase flow effect, and test this hypothesis directly with experimental adjustment of the degree of superheat of flow entering the ejector. Coupling of these results with analytical flow models will describe the mechanisms of ejector performance change to provide suggestions for improvement in ejector operation and design.

## **1.2 Background**

### **1.2.1 Ejector Pump**

The heart of the ejector-based chiller is the ejector component itself. It operates on the principle of momentum transfer from a high speed supersonic jet to entrain a second, lower-potential flow to create a pumping effect. The operation of an ejector at an idealized on-design condition (defined in Section 1.2.1.4) is shown qualitatively in Fig. 1.1, where the variation in pressure and velocity is given at the axial positions indicated in the upper ejector schematic. From axial positions  $M \rightarrow i \rightarrow ii$ , a high-temperature and pressure motive refrigerant flow expands through a converging-diverging nozzle to produce a

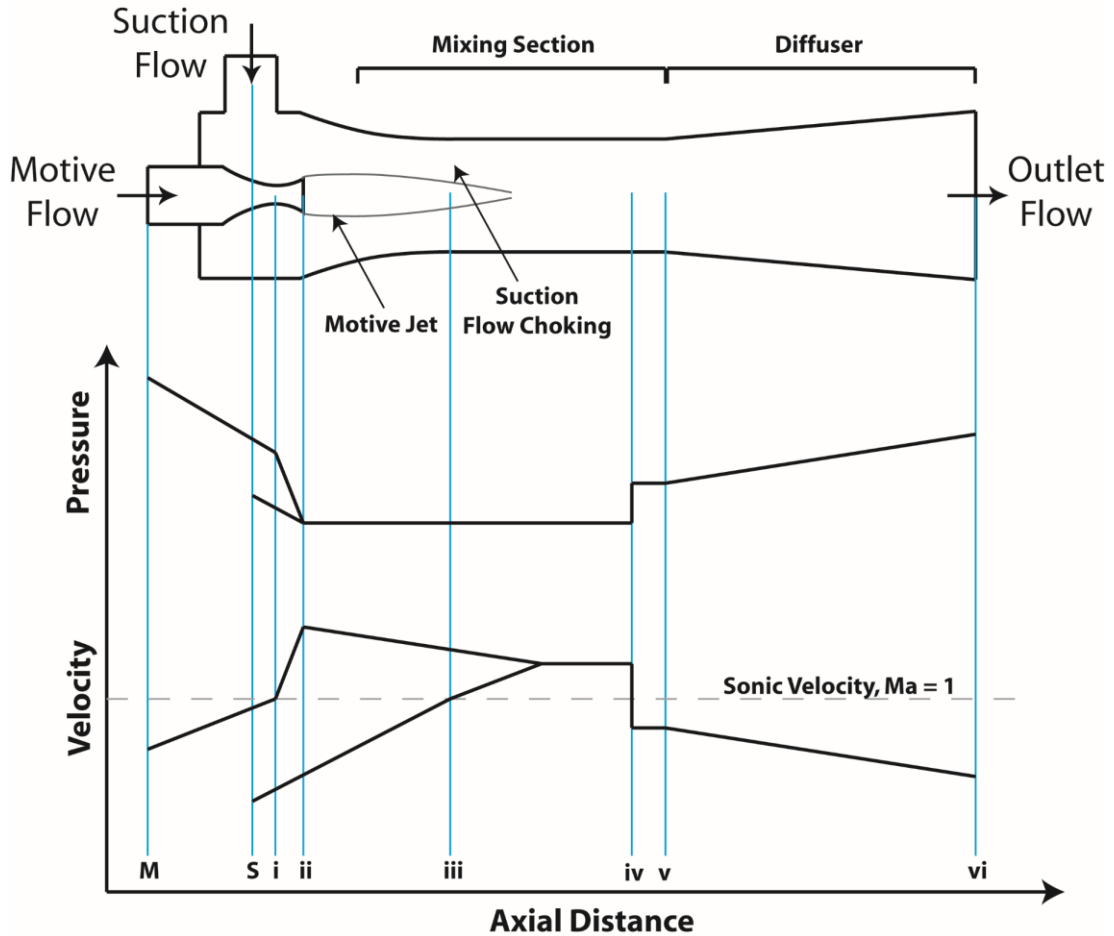


**Figure 1.1: Schematic of ejector with corresponding qualitative pressure and velocity profiles, adapted from Srisastra and Aphornratana (2005).**

supersonic jet at the motive nozzle exit. This supersonic flow entrains a suction flow entering from  $S \rightarrow ii$ . In the ejector mixing section  $ii \rightarrow iii \rightarrow iv$ , the motive and suction flows interact and mix until the combined flow nominally reaches a supersonic velocity. At  $iv$ , the flow must adjust to conditions at the ejector outlet, producing a set of shocks depicted in Fig. 1.1 as an idealized normal shock at  $iv$ , before the beginning of the diffuser at  $v$ . From  $v \rightarrow vi$ , pressure is recovered as the total flow decelerates to a low velocity at the ejector outlet. The desired compression effect produced by the ejector is the rise in pressure from the suction inlet  $S$  to the ejector outlet  $vi$ .

The two critical sections are the motive nozzle and the mixing section. Conditions inside the motive nozzle dictate the flow geometry of the motive jet and determine whether or not there is two-phase flow in applications using refrigerants. Interactions between the motive and suction flows inside the mixing section dictate the overall performance of the ejector.

### **1.2.1.1 Motive Nozzle**

The flow behavior inside the motive nozzle changes based on the relative magnitudes of the inlet and outlet pressures at states  $M$  and  $ii$  in Fig. 1.1. At a zero difference between the inlet and outlet pressures, there is no flow through the nozzle. As the outlet pressure drops, the flow rate through the nozzle increases, and the pressure of the fluid along the length of the nozzle decreases as it accelerates through the converging part of the nozzle, and rises as it decelerates through the diverging part of the nozzle. This is normal subsonic behavior. But as the back pressure is decreased past a critical point, sonic velocity is achieved at the nozzle throat where the flow chokes, and a further decrease in outlet pressure does not change the flow rate through the nozzle. The flow in the divergent section accelerates until it either shocks before the exit of the nozzle (in which case the fluid will exit the nozzle at a subsonic velocity), or if the outlet pressure is low enough, continues to accelerate for the entire length of the divergent section and exits the nozzle as a supersonic jet. The latter case explains the nominal operating condition for the motive nozzle flow. Under these conditions, many interesting phenomena occur at the nozzle exit depending on the back pressure present there. The specifics of these phenomena are explained in detail in Section 1.2.1.2.

When operating with a refrigerant, as is of interest in this work, additional complications arise when the flow has the potential to condense or evaporate inside the nozzle. If the expansion inside the motive nozzle is extreme enough, the thermodynamic state of the flow can enter the saturation dome, or exit the dome and become superheated. But since the expansion experienced in such a nozzle is at high transonic velocities, the residence time of the flow at a given condition ( $\sim 1$  to  $10 \mu\text{s}$ ) is similar to the time needed for the kinetics of liquid drop formation or evaporation (Carey, 2008). As such, the flow may exit the motive nozzle in a supersaturated state, making it necessary to consider the influences of metastable states on the motive flow. The complexities of metastable states and two-phase flow make a direct understanding of this type of flow difficult, especially for fluids other than air. Methods are developed in this work to predict flow conditions using a combination of two models: one assuming that the flow behaves as an ideal gas with no phase change, and another that assumes the flow reaches full thermodynamic equilibrium instantly with the associated quality if inside the saturation dome, as shown in Chapter 5 (Little and Garimella, 2015). The real flow conditions lie somewhere between those predicted by these two models, and a condensation shock marks the transition from one flow model to the next in the case of a condensing flow. Across a condensation shock, there is a sharp rise in pressure and temperature as droplets form, and conditions after the shock more closely resemble equilibrium conditions. With this, the likelihood of condensation at the entrance of the mixing section can be assessed and used to explain potential changes in ejector performance.



### **1.2.1.2 Mixing Section**

The high-velocity motive jet exiting the motive nozzle enters the mixing section (defined here to be the constant-area section where the motive jet first comes into contact with the suction flow) and transfers momentum to the suction flow through a jet boundary shear layer. Inherent to this process is a large velocity and temperature mismatch between the motive and suction flows that results in viscous losses and heat transfer, as well as multiple irreversible oblique shocks in the motive jet and diffuser. These flow characteristics are together responsible for the typically low ejector efficiency. In addition to all of these effects is the highly unknown contribution of phase change and its influence on heat and momentum transfer characteristics.

The mixing section is the region of the most complicated flow phenomena. A mixing section can be designed to have a constant-area or constant-pressure geometry, or a combination of both. The constant-pressure mixing section is designed such that the average static pressure within the mixing section remains constant, yielding better ejector performance (Keenan *et al.*, 1950). Unfortunately, they are difficult to design, model, and fabricate; therefore, the majority of ejector studies, including this work, use constant-area mixing sections.

The motive stream typically enters the mixing section at a supersonic velocity and forms a supersonic jet. In general, the ratio between the motive nozzle outlet pressure and back pressure determines the basic geometry of the motive jet flow in the mixing section. If the motive jet is overexpanded such that the nozzle outlet pressure is less than the back pressure (back pressure effectively being the suction nozzle outlet pressure, state *ii* in Fig. 1.1), the jet converges at the motive nozzle exit, where the first set of jet flow features are

oblique shocks issuing from the motive nozzle outlet, as in the top of Fig. 1.2. However if the motive jet is underexpanded, the outlet pressure exceeds the back pressure, resulting in a jet that diverges at the motive nozzle exit and forms an initial expansion fan at the motive nozzle exit, as in lower part of Fig. 1.2. Depending on which case occurs, these expansions and compressions reflect off both the constant-pressure boundary formed at the shear layer between the motive jet and suction flow, and the centerline boundary. This centerline boundary acts much like a solid wall in that any compression or expansion incident upon it is reflected as a wave of the same family under perfectly symmetric conditions. But the opposite is true at the boundary of the motive jet. This boundary acts as a constant-pressure boundary, and reflected waves are of the opposite family (John, 1984; Saad, 1993). This reflection of compression and expansion waves occurs many times, but eventually fades as the jet interacts with the suction flow through turbulent mixing and the development of a pressure equilibrium to the point where the flow at the mixing section exit is ideally

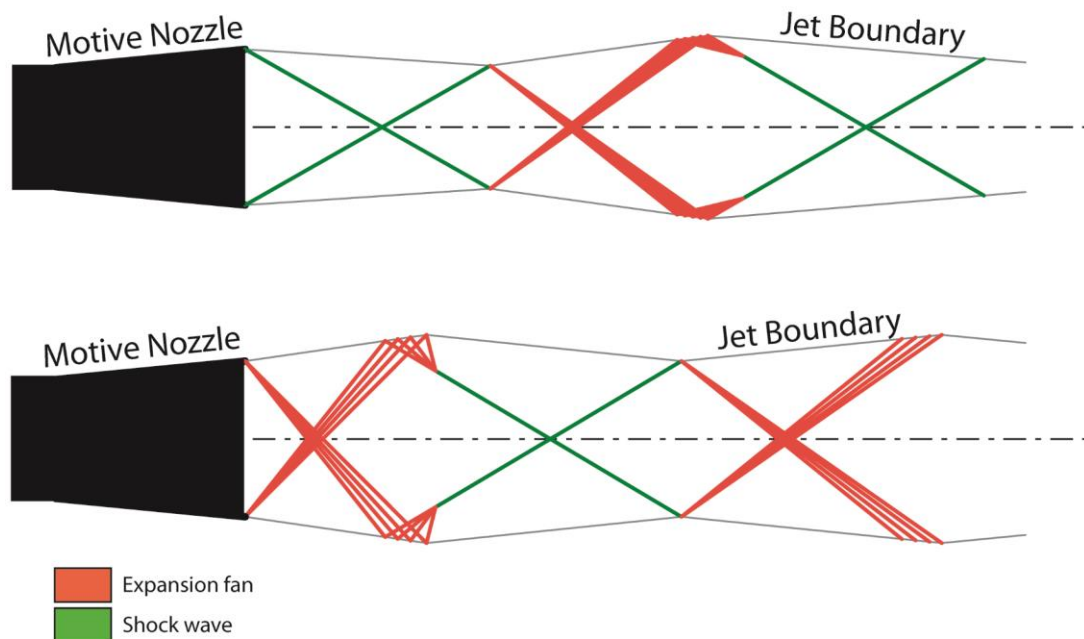


**Figure 1.2: Schematic of motive jet geometry.**

uniform. The result is a characteristic oscillation in static pressure along the centerline of the mixing section as the jet equalizes to an intermediate condition between the motive and suction inlet states.

Additional complexity is introduced when two phases are present in the flow. The speed of sound in a two-phase mixture is lower than that in either the vapor or liquid phases, decreasing the strength of shocks. Because maximum entrainment of the suction flow coincides with choking (see Section 1.2.1.4), the decrease in the speed of sound can result in a lower suction mass flow rate (Lear *et al.*, 2002).

To approximate the complex flow inside the mixing section, many assumptions are commonly used to simplify calculations, including approximating the combination of shock cells in the motive jet as a single normal shock, and lumping shock and other losses into one simple isentropic efficiency coefficient for the mixing section as a whole. Other methods employ numerical modeling techniques to simulate the flow more directly. Both analytical and computational methods are discussed in this study.

### **1.2.1.3 Working Fluid Selection**

The choice of working fluid is important when considering the stability and efficiency of operation because phase change as well as heat and momentum transfer between the suction and motive flows can vary significantly. Working fluids are generally grouped into two categories, often referred to as “wet fluids” and “dry fluids.” The differentiation between these two is the behavior of the fluid as it is expanded isentropically from a saturated vapor state. If the fluid flashes during expansion, it is known as a wet fluid, and if it does not, it is a dry fluid. The key difference between the two fluids can be understood by observing the shape of the vapor-liquid dome. For example, in Fig. 1.3 (a), the right-

side of the saturation dome has a negative slope; therefore, when the fluid is expanded from a saturated vapor state, it flashes and enters the vapor dome. Conversely, in Fig. 1.3 (b) the slope of the right-side of the saturation dome is positive, allowing the fluid to remain in the vapor phase as it expands isentropically. This property enables prediction of the potential for phase change inside an ejector. If a dry fluid is used, the motive flow evaporates instead of condensing as it passes through the motive nozzle. With a wet fluid, it would be more likely to condense.

The exact effect of this phase change in ejectors has been the source for some debate. Chen *et al.* (1998) state that droplet formation at the outlet of the ejector would

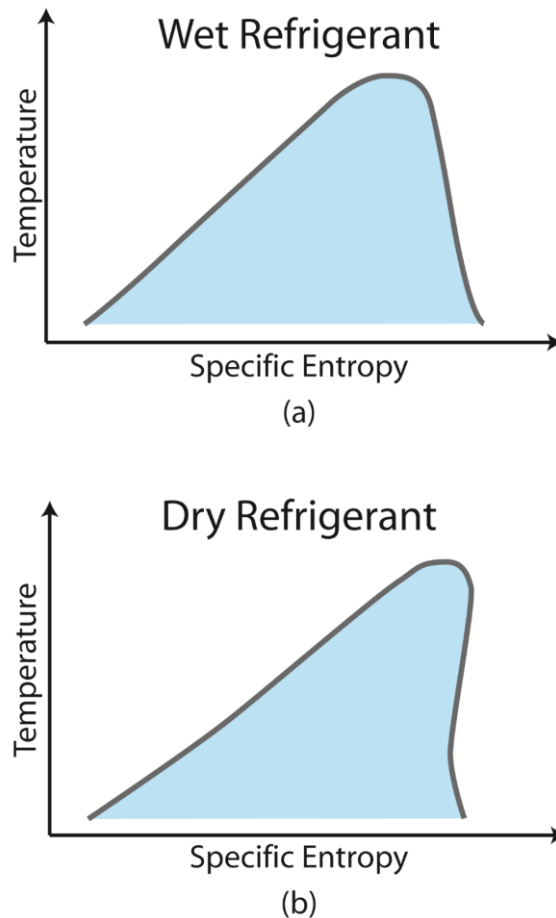


**Figure 1.3: Qualitative  $T-s$  diagrams for (a) wet and (b) dry fluids.**

restrict flow and cause damage, and Dahmani *et al.* (2011) suggest that condensation may decrease performance because of an increase of interphase friction and slowing of flow. However, Al-Ansary and Jeter (2004) and Hemidi *et al.* (2009a) state that the existence of liquid droplets in ejector flows may aid in the momentum transfer and result in a higher ejector performance, and have experimentally demonstrated an increase in performance at some conditions.

There are other fluid properties that are universally accepted as beneficial to ejector and ejector system operation. A large latent heat of vaporization is desirable to minimize the circulation rate needed for a given cooling capacity. A low vaporization pressure and temperature allow for safer operation and lighter cycle construction, and the use of lower-quality waste heat sources to vaporize the motive flow. A large difference in molecular mass between the motive and suction flows aids in momentum transfer, resulting in a higher suction flow entrainment. And as is the case with any refrigerant, it is desirable to have a fluid that is a chemically stable, non-toxic, non-corrosive, environmentally friendly, and inexpensive, with a high thermal conductivity. Eames *et al.* (2007), Chunnanond and Aphornratana (2004), and Grazzini *et al.* (2012) provide fluid property tables that compare multiple candidate fluids side by side to discuss their advantages and disadvantages. Table 1.1 provided here is a compilation of most of these data.

While Chunnanond and Aphornratana (2004) have suggested that fluids with lower viscosity are beneficial for system performance, there likely exists an optimum value for viscosity when considering operation of the ejector component. While lower viscosity fluids would have the advantage of lower pressure losses due to friction with the ejector walls, higher values of viscosity would aid in suction flow entrainment because momentum

**Table 1.1: Candidate fluids for ejector-based chiller.**

	<b>R11</b>	<b>R12</b>	<b>R113</b>	<b>R123</b>	<b>R134a</b>	<b>R141b</b>	<b>R245fa</b>	<b>R744 (CO<sub>2</sub>)</b>	<b>R718b (Water)</b>
<b>Boiling point at 1 atm [°C]</b>	23.7	-29.8	47.5	27.7	-26.1	32.0	15.1	-	99.9
<b>Pressure at 100°C [kPa]</b>	817	3342	438	787	3975	677	1269	-	101
<b>Molecular mass [kg kmol<sup>-1</sup>]</b>	137.4	120.9	187.4	152.9	102.0	117.0	134.0	44.0	18.0
<b>Latent heat at 10°C [kJ kg<sup>-1</sup>]</b>	185.3	146.4	155.4	177.9	190.8	233.3	212.8	197.1	2476.9
<b>Global warming potential (GWP)</b>	4000	2400	4800	0.02	1300	630	950.0	1	0
<b>Ozone depletion potential (ODP)</b>	1	1	0.8	0.02	0	0.11	0	0	0
<b>Wet/dry fluid</b>	Wet	Wet	Dry	Dry	Wet	Dry	Dry	Wet	Wet

transfer from the motive to suction flow occurs through a viscous shear layer. A rigorous study focusing on the effect of viscosity is missing in the literature, and could be explored using available computational techniques.

Water has historically been a popular choice for an ejector working fluid, mostly because of the early use of ejectors for replenishing water in reservoirs for steam engine boilers, or to provide emergency cooling to nuclear reactors. The limitations of relatively high freezing and boiling points of water tend to lead to low performance values, and require larger heat exchangers (Eames *et al.*, 2007). Air has also been used, but for applications different from those of interest to the present study. HCFC refrigerants have been popular working fluids for ejectors because of their utility in refrigeration systems, but face increasing pressures from environmental considerations, and are in the process of being phased out. Therefore, current popular working fluids include air and water for many studies on fundamental flow characteristics, but other fluids such as ammonia, R134a, R141b, R142b, R245fa, and R744 (CO<sub>2</sub>) are more suitable, especially for chiller applications. R245fa is of particular interest because it is a good candidate for chiller cycles for its low global warming potential and low boiling temperatures. R744 is desirable

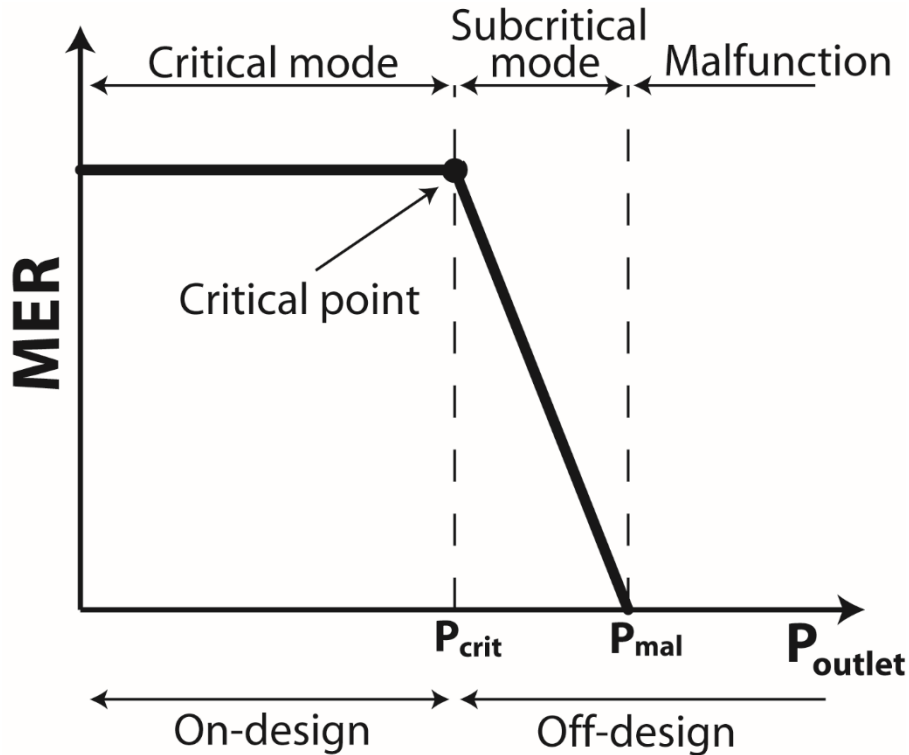


**Figure 1.4: Qualitative ejector characteristic curve at a set motive and suction inlet pressure. On- and off-design regions are labeled, as well as the critical point at the threshold between these two regions.**

because of its low global warming potential, and also for the large difference between typical high and low operating pressures and the use of lower mean driving temperature differences needed during supercritical operation (Tischendorf *et al.*, 2010).

#### **1.2.1.4 Operational Metrics and Characteristics**

Properties of the flow in the motive nozzle and mixing section have a strong impact on the way the ejector operates. First, choking of the motive flow in the motive nozzle defines the maximum possible motive flow rate. Second, conditions at the outlet of the ejector define whether or not the suction flow will choke. Figure 1.4 shows what is commonly called a *characteristic curve*. It shows the change in mass entrainment ratio, MER, with ejector outlet pressure, where MER is defined as

$$MER = \frac{\dot{m}_{suction}}{\dot{m}_{motive}} \quad (1.1)$$

At high outlet pressures, the suction flow has not yet choked, and a change in outlet pressure translates to a change in suction mass flow rate. This is called the *off-design* operating regime because the maximum suction flow rate has not yet been realized. But with decreasing outlet pressure, a critical point is reached at which the suction flow becomes choked, and further decrease of the outlet pressure no longer has an effect on suction mass flow rate. The flat part of the curve at low outlet pressures is called the *on-design* operating regime where the maximum possible suction flow rate is reached.

The suction flow rate that can be entrained (capacity), as well as the pressure rise from suction inlet conditions to ejector outlet conditions (lift), are of great importance when quantifying ejector performance. While MER defines the capacity of the ejector, suction pressure ratio, SPR, defines the lift.

$$SPR = \frac{P_{ejector\ outlet}}{P_{suction\ inlet}} \quad (1.2)$$

where the ejector outlet and suction inlet pressures are taken at positions  $vi$  and  $S$ , respectively, in Fig. 1.1. It is also commonly desirable to define an ejector efficiency. There is much discussion in the literature as to how exactly define ejector efficiency, as the definition can depend heavily on the application for which the ejector is used. One version, used in the ASHRAE handbook (ASHRAE, 1983) on steam-jet refrigeration equipment, is:



$$\eta_{ejector} = \frac{(h_{ejector\ outlet} - h_{suction\ inlet})(\dot{m}_{motive} + \dot{m}_{suction})}{\dot{m}_{motive}(h_{motive\ inlet} - h_{suction\ inlet})} \quad (1.3)$$

where the numerator is the actual compression energy recovered, and the denominator is the theoretical energy available in the motive stream. A comparison of other ejector efficiency definitions can be found in the review by Liu (2014), including efficiencies related to the ejector working as a turbine or compressor only, as well as exergetic efficiencies.

To maximize MER and SPR and related efficiency, the conditions inside the mixing section should be established in a manner that promotes momentum transfer from the motive to suction flow. As mentioned above, control of phase-change phenomena, fluid selection, and geometry optimization has the potential to do so.

### 1.3 Ejector-Based Chiller

The basic cooling cycle configuration under consideration in this work is shown in Fig. 1.5

(a). An upper loop boils a refrigerant flow, to the desired state point 1. It then enters the ejector through the motive nozzle where it expands to state 2, defined as the exit of the motive nozzle. It then mixes with the suction flow entering from the bottom loop to state 3, and recovers pressure to the ejector outlet at state 4. This total flow enters the condenser where heat is rejected to the ambient until slightly subcooled conditions are reached. At this point, the flow splits, one part being pumped through the upper loop to state 8 at the inlet of the boiler, and the other part expanding through the expansion valve in the bottom loop to the inlet of the evaporator. From states 6 to 7, heat is removed from the conditioned space to produce the desired cooling effect. The flow at state 7 is entrained into the ejector through the suction nozzle to mix with the motive flow from the upper loop. In essence,

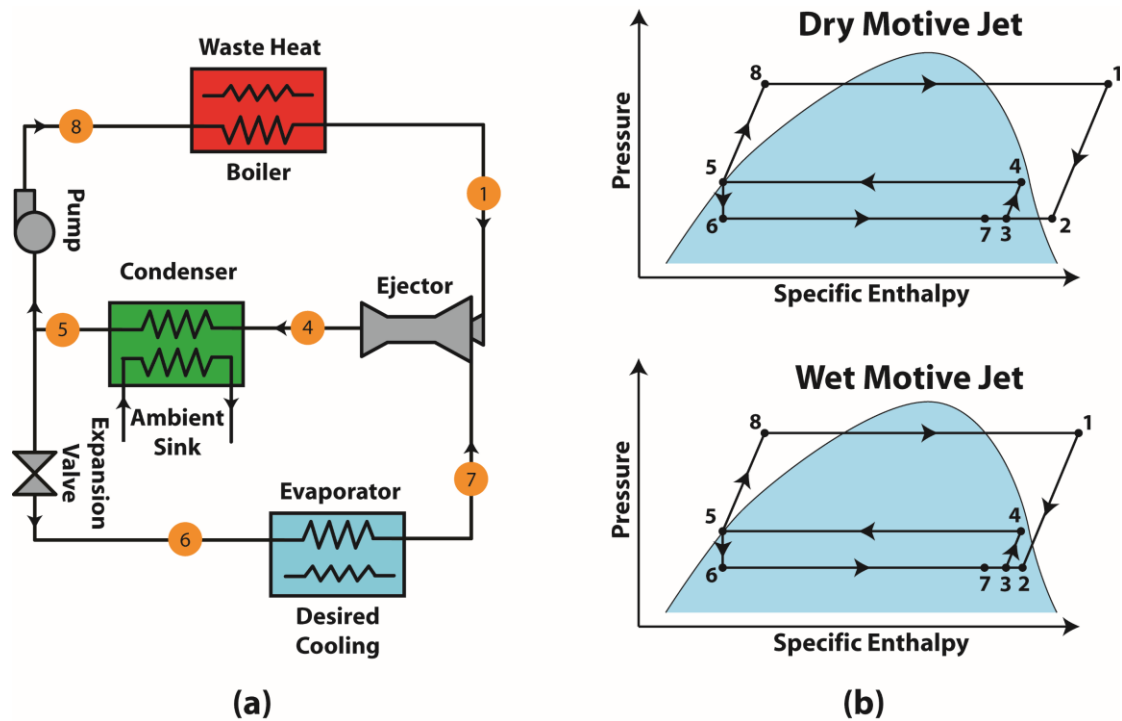


**Figure 1.5: (a) Schematic of the ejector-based chiller cycle and (b) qualitative  $P$ - $h$  diagrams with cycle state points indicated for dry and wet jet operation with wet fluid.**

the work produced from the expansion of refrigerant from state 1 to 2 is used to directly power the compression effect needed in the bottom loop to produce cooling at the evaporator. In this way, the ejector accomplishes the function of both a turbine and a compressor, extracting work from the upper loop (turbine functionality) and using that work to drive cooling in the bottom loop (compressor functionality).

The coefficient of performance, COP, of the cycle is used as the typical performance metric, and can be defined in terms of MER:

$$COP = MER \frac{h_{\text{evaporator outlet}} - h_{\text{condenser outlet}}}{h_{\text{boiler outlet}} - h_{\text{condenser outlet}}} \quad (1.4)$$

The exact properties of state point 1 are of great importance. Conventional operation of the cycle dictates that state 1 be significantly superheated by  $>10$  K (typically between 25 and 30 K for gas turbines (ASME, 1992; Boyce, 2006)). This practice is taken from typical operational procedures for radial and axial expanders where condensing flow is avoided because it can cause significant damage to rotating machinery due to detrimental droplet impingement effects on sensitive, high-speed components. Because of the mechanical simplicity of the ejector, these effects are not a significant concern, and a wider range of conditions are allowable at state 1 for safe operation.

Based on the above discussion, determining the effect of phase change on ejector-based chiller performance requires the following:

- Design and fabrication of a functioning ejector-based chiller
- Development of a visualization method to observe flow phenomena in the ejector mixing section
- Design and fabrication of a functioning ejector with optical access
- Development of a CFD model of ejector flow
- Development of an analytical model of ejector flow
- Combination of visual, CFD, and analytical results to evaluate phase change, heat transfer, and momentum transfer effects
- Determination of the relationship between these effects and overall cycle COP.

#### **1.4 Organization of Thesis**

The remainder of this thesis is organized as follows:

- Chapter 2 presents a review of the literature on the ejector component, focusing on analytical, numerical, and visualization techniques used to understand fundamental flow characteristics. A review of cycle-level studies is then presented to introduce previous configurations for ejector-based chillers and their optimization. The basis and motivation for this work is given here.
- Chapter 3 presents work on a large-scale air ejector used for the development of a local visualization measurement technique. A CFD model of the observed flow field is developed in conjunction with a 2D analytical model of the motive jet to pinpoint locations of non-ideal mixing and heat transfer effects.
- Using the visualization and CFD techniques from Chapter 3, Chapter 4 presents the development of a transparent ejector test section, designed to give undistorted visual access to high temperature and high pressure refrigerant ejector flows. A study of flow images with corresponding MER values and CFD simulations helps provide a basis for model validation, and allows for the first images of two-phase refrigerant flows in ejectors under operating conditions representative of an ejector-based chiller.
- Chapter 5 demonstrates ejector-based chiller performance improvement at conditions of lower motive nozzle inlet superheat. To explain the observed trends, a 1D analytical model of the motive nozzle is formulated to approximate the presence and degree of condensation. This model is used with a control volume analysis to determine the roles of phase change, heat transfer, and momentum transfer effectiveness in the mixing section where suction flow entrainment occurs.

- Chapter 6 draws conclusions based on the insight gained in this study on the effects of phase change and fluid selection on cycle-level performance. Suggestions are made for best design and operational practices for the ejector-based chiller to maximize COP. Recommendations are made for future research activities.

## CHAPTER 2

### A CRITICAL REVIEW LINKING EJECTOR FLOW PHENOMENA WITH COMPONENT- AND SYSTEM-LEVEL PERFORMANCE

Ejectors have been used in a wide variety of applications in the chemical process, nuclear reactor, and chiller industries. In the process industry, they have been used to pump corrosive liquids, slurries, fumes, or other hazardous fluids that are difficult to circulate with conventional pumps and compressors. In nuclear reactors, they have been used to provide emergency cooling in the event of reactor failure (Beithou and Aybar, 2000). In power plants, they are used to remove non-condensables from air-cooled condensers. In chillers, the subject of this work, they are used to reduce the need for, or eliminate, mechanical compression. This chapter addresses studies focused on the ejector component, and on ejector usage in chillers. Section 2.1 discusses the development of ejector technology. Section 2.2 reviews the literature on ejector component modeling, subdivided into analytical studies, numerical studies, and visualization studies. Section 2.3 reviews the literature on ejector-based chillers and passive system configurations. Section 2.4 concludes by establishing the basis for future work, emphasizing the need for a better understanding of phase-change phenomena to determine the relationship between local ejector characteristics and global system-level effects.

#### **2.1 Ejector History and Previous Reviews**

##### **2.1.1 Early History**

Ejectors are by no means a new technology, but their simplicity and passive operation has led to renewed interest, especially for use in chiller systems. In 1858, Henry Giffard invented the first condensing ejector to replenish the water reservoir of a steam engine

boiler. The reliability of mechanical pumps was very low at the time, thus making this a major advancement in steam engine design. The ejector used by Giffard had only a converging nozzle and did not employ supersonic flow. In 1869, Schau was the first to use a converging-diverging nozzle in his ejector design, and in 1901, Sir Charles Parsons used an ejector to remove non-condensable gases from steam condensers. Then in 1910, Maurice Leblanc used the first steam ejector in a chiller system (Elbel and Hrnjak, 2008).

In the 1930s, the use of ejector-based chillers increased significantly for use in large buildings, but came to a standstill with the advent of vapor compression systems when they proved to be more cost effective and efficient. In the 1950s, the growing nuclear industry took an interest in ejectors for emergency cooling systems for nuclear reactors, using vaporized water from an accident to circulate liquid water from a cooling reservoir. This resulted in much research on ejector flow phenomena, including the popular Keenan papers: Keenan and Neumann (1942) and Keenan *et al.* (1950). Later, in the 1970s, and again more recently in the early 2000s, fluctuating fuel costs sparked new interest in ejector technology for its ability to reduce primary energy consumption, especially in chiller systems.

### **2.1.2 Previous reviews of ejector work**

The significant volume of papers that have been published on ejectors since the late 1990s reflects the renewed interest in ejector fundamentals and application. The foci of these papers have ranged from the specifics of ejector flow phenomena to more general system-wide studies on ejector applications. This large volume of papers and the wide breadth of their subject material has led to a few review papers. These are summarized in this section and are presented in Table 2.1 based on the types of ejector models and chiller cycles

covered. Of the chiller cycle types listed, the bottoming vapor compression (VC) cycle couples a vapor compression cycle to the evaporator of the ejector-based chiller to produce additional cooling. The boosted cycle uses a compressor (booster) to assist the ejector. The augmented VC cycle is a normal vapor compression cycle where some of the expansion losses in the expansion valve are recovered with an ejector. These cycles, as well as the use of cascaded ejectors, solar powered cycles, and passive cycles omitting the need for a fluid pump are all covered in Section 2.3. Schematics of each type of cycle can be found in (Sokolov and Hershgal, 1990a).



**Table 2.1: Overview of previous review papers and key contributions.**

Article	Ejector Component Model Type			Ejector-Based Chiller Cycle (see Sokolov and Hershgal (1990a) for system schematics)							Key Contributions
	1D	2D	CFD	Bottoming VC	Boosted	Augmented VC	Cascaded Ejectors	Solar Powered	Passive	Other	
<b>Sun and Eames (1995)</b>	x	x		x			x	x		x	Review of technology before 1995; lacks information on CFD and working fluids
<b>Chunnanond and Aphornratana (2004)</b>	x			x	x			x	x	x	Introduces many different applications for ejectors; little mention of CFD analyses or two-phase flow
<b>Elbel and Hrnjak (2008)</b>				x		x				x	Includes historical background; focus on transcritical R744 cycles
<b>Elbel (2010)</b>						x				x	Similar to Elbel and Hrnjak (2008), but with coverage of studies with two-phase ejectors as well as some experimental results
<b>Abdulateef <i>et al.</i> (2009)</b>				x			x	x		x	Focus on applications using solar heat
<b>Matsuo <i>et al.</i> (1999)</b>	x		x								Coverage of fluid flow phenomena inside ejectors

Sun and Eames (1995) wrote one of the earliest review papers. Their review primarily discussed the different analytical models for constant-pressure and constant-area ejector designs. Studies that include 1D as well as 2D models were cited. Many of the included 2D studies were analytical, while three of them were early numerical studies. It was stated that there were no CFD models at that time that considered the whole ejector component, reflecting the lack of adequate computing power before 1995. The review also cited many studies for various ejector applications such as steam-jet refrigeration, solar-powered refrigeration, and combined ejector-absorption refrigeration, with a special section dedicated to ejector chiller cycles using halocarbon compounds. Due to the ban and phaseout of several of the refrigerants considered, some of that information is no longer applicable.

Since the Sun and Eames review, a few others were written that focused mostly on ejector application rather than on flow fundamentals. Chunnanond and Aphornratana (2004) published a review of the application of ejectors in refrigeration systems. The applications considered were categorized as steam-jet refrigeration, solar-powered, compression-enhanced, and hybrid ejector-absorption cycles. No information was included on passive systems operating without electrical input from a pump, the development of numerical models, or the exploration of two-phase phenomena. This was because before 2004, there had been minimal work in these areas. Other review papers on ejector application were written by Elbel and Hrnjak (2008) and Elbel (2010), and reported the development of ejector technology with a focus on transcritical CO<sub>2</sub> ejector refrigeration systems. Attention was given to the ejector as a tool to recover expansion work and energy from low-grade temperature sources, and Elbel (2010) provided coverage of studies using

two-phase ejectors. Abdulateef *et al.* (2009) focused specifically on solar-driven ejector refrigeration cycles. The discussed categories included single- and multi-stage ejector-based chiller systems, ejector-based chillers with boosters or compressors, and solar-driven combined ejector and absorption/adsorption chiller systems. These categories are similar to those in the review paper by Chunnanond and Aphornratana (2004), but there was also mention of the use of cascaded ejectors and adsorption applications. Between 2004 and 2009, there were a few studies on completely passive cycles as well as work on CFD modeling. Abdulateef *et al.* (2009) does not mention these, representing a gap in the review.

The aforementioned reviews provide only rudimentary information on ejector flow fundamentals. Such simple explanation of ejector flow is sufficient for many applications, but it does not provide guidance on the internal measures necessary to improve ejector performance. The only review paper that has approached these questions is by Matsuo *et al.* (1999). The focus of that review is exclusively on internal gas flow in constant-area channels, but there is a section dedicated to ejector flow. Because the flow phenomena in constant-area channels are similar to the phenomena seen in ejectors, the explanations for how and why certain flow structures form are helpful from an ejector standpoint.

No paper has yet provided a review of CFD modeling of ejectors or of the potentially important effects of two-phase flow. The sections below provide such a review and couple it to studies on the use of ejectors in chiller cycles. The main objective is to provide a practical component-to-system level understanding of the advances and deficiencies in ejector modeling, and determine the improvements in existing tools necessary to improve performance of ejectors and systems that employ them.

## 2.2 Ejector Component Modeling

### 2.2.1 Analytical studies

This section provides a review of analytical studies on the ejector component. The majority of these papers have utilized simplified, 1D models of fluid flow phenomena. The typical analytical study uses many assumptions that are universal across authors, including ideal gas behavior of the working fluid, steady-state operation, adiabatic walls, zero inlet velocities, and uniform cross-sectional temperature and velocity profiles. Other common simplifications include either a constant-pressure or constant-area mixing section, approximation of oblique shocks as normal shocks, the use of isentropic efficiency coefficients for each ejector section to account for losses, assuming homogeneous characteristics for two-phase mixtures, and the starting of mixing at the aerodynamic throat formed by the motive stream.

Many of these assumptions originate from the two key studies by Keenan *et al.* (Keenan and Neumann, 1942; Keenan *et al.*, 1950). These are the first studies to develop a simplified model of an ejector and use it to explore the characteristics of ejector operation. They formulate a basic model of an ejector using many of the assumptions listed above, including ideal-gas air for both motive and suction flows, adiabatic walls, and all isentropic processes. Normal shocks are accounted for and discussed. The ejector in Keenan and Neumann (1942) is a simplified ejector with a constant-area mixing section and no diffuser, whereas multiple geometries are considered in Keenan *et al.* (1950) that include different motive nozzle and mixing section geometries.

Their model divides the ejector into its basic subcomponents: the motive nozzle, suction nozzle, mixing section, and diffuser. For both the motive and the suction nozzles,

it is assumed that the fluid expands reversibly and adiabatically, and that inlet velocities are zero. Momentum, energy, and mass balances are combined to find the exit state of the mixing section. Then for the diffuser section, the ejector outlet state is found with the conventional relation for pressure rise in a reversible, adiabatic, and subsonic diffuser.

The predictions of this simplified model are validated experimentally and show good agreement at low MERs, with the model always over-predicting pressure recovery in the diffuser. At higher MERs, errors increase significantly because the model is not able to predict the losses that become more prominent at higher flow velocities. The inability of this model to account for these losses as well as its specific application for ideal gas flow has spurred many subsequent studies, all of which have improved upon the Keenan models in various ways. One such example is an early paper by Fabri and Siestrunk (1958) that focuses more on the aerodynamic theory of ejector flow, and includes effects of flow separation, friction, and the formation of an aerodynamic throat for the suction flow. Detailed performance curves are generated to predict ejector flow patterns, alluding to the existence of motive jet flow features, and important parameters for ejector design optimization. Another early study by Munday and Bagster (1977) focuses on an ejector for a steam-jet refrigeration application. A previous method outlined by Stoecker (1958) was augmented to account for an aerodynamic throat for the suction flow, much like that seen in Fabri and Siestrunk (1958).

Building on the model by Fabri and Siestrunk, a paper by Dutton *et al.* (1982) models a constant-area air ejector. This model is slightly different from the standard analytical models above because it divides the mixing section into three control volumes to account for effects of suction choking, assuming that the motive and suction flows do

not mix for a designated inviscid interaction region. One control volume contains the motive stream before mixing, another is the suction stream before mixing, and the last addresses the two streams combined for the remainder of the mixing section. This method exhibits errors between 15-22% for SPR when compared to experiments, and higher errors for MER. These discrepancies are due to the neglect of prominent flow phenomena inside the mixing section that contribute significantly to losses, including boundary layer separation and shock wave-boundary layer interactions.

Part two of a three part study by Sokolov and Hershgal (1990b) adapts the Keenan model for use with fluids other than air in a constant-pressure mixing section ejector. Similarly, Ouzzane and Aidoun (2003) and Chen *et al.* (2013) develop a model that is validated for both on- and off-design regimes. Also building upon the Keenan model, a study by Eames *et al.* (1995) accounts for frictional losses in the motive nozzle, mixing section, and diffuser with experimentally based isentropic efficiency terms that are incorporated into the mass, momentum, and energy balances. This is a major improvement over the Keenan model, because it has been shown, for example in Dutton *et al.* (1982), that losses from friction and shocks can significantly affect ejector flow. Even though the working fluid for this study was steam, the ideal gas assumption was still used in the governing equations for the model. It was found that the ejector model always over-predicts MER, and does so with 30% error or less, indicating that the model still employs too many assumptions.

A similar model used by Huang *et al.* (1999) also assumes ideal gas behavior, choking of the suction flow at an aerodynamic throat formed by the motive stream, and a mixing section that is constant-pressure and constant-area, and accounts for frictional and

mixing losses with isentropic efficiency coefficients. The model was compared with results from multiple experimental runs with eleven different ejector geometries operating under various conditions with R141b. Geometries range from motive nozzle throat diameters from 2.6 to 2.8 mm, motive nozzle exit diameters from 4.5 to 5.1 mm, mixing section outlet diameter from 6.7 to 9.2 mm, mixing section converging angles from 60 to 68°, motive nozzle inlet pressures from 0.4 to 0.6 MPa, and saturated vapor temperatures corresponding to the critical back pressure (ejector exit pressure) from 24.4 to 42.5°C. The values of the isentropic efficiency coefficients are determined by matching this 1D model to the experimental data under the conditions listed above. Specifically,  $\eta_m$ , the isentropic efficiency of the motive nozzle flow, is found to be 0.98, and  $\eta_s$ , the isentropic efficiency of the suction nozzle flow, found to be 0.85. The  $\phi_m$  coefficient accounts for losses in the motive flow due to viscous effects, slipping, and change in flow area between the outlet of the motive nozzle and the aerodynamic throat location in the mixing section, and is found to be 0.88. Finally, the  $\phi_s$  coefficient accounts for frictional losses in the suction flow. The value of  $\phi_s$  varies with the ratio of mixing section exit area to motive nozzle throat area.

The values indicated above for isentropic efficiencies and loss coefficients have been used widely in subsequent studies. For example, Yu *et al.* (2007), Liu and Groll (2008), and Guo and Shen (2009) use a model combining those of Keenan and Huang *et al.* Whereas Huang *et al.* accounts for friction and other losses with empirical coefficients, studies by Balamurugan *et al.* (Balamurugan *et al.*, 2006; Balamurugan *et al.*, 2007) are able to directly evaluate some of these effects with the use of head loss coefficients based on subcomponent geometry and two-phase pressure drops.

A semi-empirical model by Cizungu *et al.* (2001), similar to that of Huang *et al.* (1999), does not assume ideal gas properties. This model is first validated with experimental data from the literature using R11, after which more modern working fluids are simulated to determine performance. R123, R134a, R152a, and R717 (ammonia) are considered, all of them showing similar performance with varying ejector geometry and operating conditions, except at lower motive stream temperatures where R717 does not perform as well. This is one of the first studies to compare ejector performance with different working fluids, specifically those that are meant for use in ejector-based chiller systems. Parts of this model were adopted in a later study, also by Cizungu *et al.* (2005), to optimize ejector performance with ammonia, and ammonia-water mixtures.

With the use of refrigerant working fluids comes the potential for two-phase flow. Subsequent studies using steam-water or air-water analogues help pinpoint the exact characteristics of the two phases. Deberne *et al.* (1999) presented a model of a two-phase ejector using liquid water as the motive stream and steam as the suction stream. The model covers the mixing section and diffuser only. Assuming that the outlet states of the motive and suction nozzles are known a priori, it predicts the ejector performance to within 15% accuracy. The mixing section model includes details such as condensation rate, void fraction, and an adjusted speed of sound for two-phase flow. It is assumed that there is a normal shock at the interface between the mixing and diffuser sections, across which complete condensation of the flow occurs. (This phenomenon is known as a *condensation shock*, and is explored in various studies such as those by Bergander (2006) and Grazzini *et al.* (2011).) The accompanying single-phase model of liquid water in the diffuser is standard and includes a loss coefficient for a conical diffuser. This is one of the first studies



to focus specifically on the existence of two phases. It asserts that in the first part of the mixing section, before the motive and suction streams mix, momentum transfer is important. As the motive stream disintegrates into small droplets and forms a homogeneous two-phase flow, heat and mass transfer effects become more prominent as relative velocity decreases, and available surface area between the two phases increases. A study by Butrymowicz (2009) also studies an ejector with a liquid water motive jet and air suction flow. Two-phase models of the mixing and diffuser sections, as well as momentum loss coefficients for them, are determined through a comparison between experimental data and the incorporation of geometric parameters.

Lear *et al.* (2002) also studied two-phase ejector flow, but with R134a. All subcomponents were assumed to be isentropic except for the mixing section, and the shocks were assumed to be normal. Their model used the standard control-volume analysis around each subcomponent with mass-averaged properties. In previous papers, the location and existence of shocks was assumed, but this paper contains a discussion on where shocks form and how two-phase flow affects shock formation. Specifically, much attention is given to the concept of a Fabri limit, defined as the limit of suction flow experienced when it chokes in the aerodynamic throat formed by the motive flow, as defined in Fabri and Siestrunk (1958). Unfortunately, the results from this model are not validated experimentally; therefore, the accuracy of certain assumptions is unknown. However, it is the first paper to explore suction flow choking as a result of the suction flow entering the two-phase regime. A similar study was presented by Rogdakis and Alexis (2000), but the model developed does not account for the effects of two-phase flow on choking, or the existence of an aerodynamic throat.

Other studies that consider two-phase flow are those by Jelinek *et al.* (2002) and Levy *et al.* (2002). Levy *et al.* used a continuum model to approximate two-phase flow in a diffuser, accounting for the presence of individual liquid droplets. Jelinek *et al.* used this same model to predict the performance of an ejector in a triple-pressure-level absorption cycle.

A novel study by Zhu *et al.* (2007b) uses a very different approach. Unlike the aforementioned studies, their study considers mixing section flow in two dimensions to account for the presence of the motive jet and wall boundary layer. Ideal gas relations are used with isentropic efficiency coefficients to determine the exit states of the motive and suction nozzles. In the mixing section, a velocity profile is estimated, assuming an infinitely thin annulus of  $M = 1$  at the boundary between the motive and suction flows where the motive jet boundary is, and an exponential velocity distribution in the suction flow region. Comparing the results of this study to that of Huang *et al.* (1999), the results of the 2D shock circle model are significantly better with errors always below 15% as compared to the Huang *et al.* method that had errors up to 25%. Furthermore, the Zhu *et al.* model only requires 14 equations with two isentropic coefficients as compared to the 18 equations and four isentropic coefficients needed by the Huang *et al.* model. This same model was applied for use in a Solid Oxide Fuel Cell (SOFC) system for fuel injection and recirculation (Zhu *et al.*, 2007a), and compared to data collected by Marsano *et al.* (2004), with errors of 1.94% or less in mass flow rates and entrainment ratios.

Although there have been many other modeling studies, the papers presented above show the characteristic progression of model sophistication and the challenges that are present with such analytical treatment of ejector flow. A compilation of the ejector

component studies is included in Table 2.2, listing assumptions, ranges, and major contributions of each paper. In general, most models are based directly or indirectly on the Keenan model where the ejector is divided into the typical four subcomponents with appropriate mass, energy, and momentum balances. Although the Keenan model is a good start, ideal gas, normal shock, and isentropic flow assumptions all make it inaccurate for a wide range of conditions. Improvements have been made in three general ways: including loss coefficients, removing the ideal gas assumption, and modeling fluids other than air. One assumption that has been maintained throughout the progression of models is the formation of normal shocks. Only the study by Zhu *et al.* (2007b) has attempted to account for more realistic oblique shocks.

**Table 2.2: Component-level analytical modeling studies and key contributions.**

Article	# of Phases		Experimental	Working Fluid	Analytical Model Assumptions						Key Contribution
	1 Phase	2 Phase			1D	2D	Constant P Mix	Constant A Mix	Normal Shocks	Ideal Gas	
<b>Keenan and Neumann (1943)</b>	x		x	Air	x		x	x		x	First paper to make analytical model of ejector mixing section; most commonly referenced
<b>Keenan <i>et al.</i> (1950)</b>	x		x	Air	x		x	x	x	x	First paper to make analytical model of whole ejector; most commonly referenced
<b>Fabri and Siestrunck (1958)</b>	x		x	Air	x			x		x	Fundamental study of ejector flow phenomena from first principles including effects of aerodynamic Fabri choking
<b>Dutton and Carroll (1986)</b>	x		x	Air	x			x		x	Optimization including molecular weight of motive and suction streams
<b>Balamurugan <i>et al.</i> (2006, 2007)</b>		x	x	Air and Water	x			x		x	Model details two-phase pressure drop; detailed literature review tables include correlations from previous studies
<b>Owen <i>et al.</i> (1992)</b>		x	x	Air and Water	x					x	Finds diffuser pressure recovery coefficient that matches well with two-phase data; explores effect of void fraction on performance
<b>Levy <i>et al.</i> (2002)</b>	x	x		R125-DMEU and -DMETEG	x						Uses two-phase continuum model to predict conditions inside diffuser
<b>Grazzini and Rocchetti (2002)</b>	x			R718	x					x	Develops code for ejector geometry and overall cycle optimization
<b>Cizungu <i>et al.</i> (2005)</b>	x	x		Ammonia and Ammonia-Water	x		x				Compares results from single- and two-component refrigerants
<b>Munday and Bagster (1977)</b>	x		x	Water	x		x		x		One of first papers to account directly for shock losses
<b>Dutton <i>et al.</i> (1982)</b>	x		x	Air	x			x		x	Considers ejectors where suction stream enters at a supersonic velocity; considers effects of boundary layers on ejector operation

**Table 2.2: Component-level analytical modeling studies and key contributions.**

Article	# of Phases		Experimental	Working Fluid	Analytical Model Assumptions						Key Contribution
	1 Phase	2 Phase			1D	2D	Constant P Mix	Constant A Mix	Normal Shocks	Ideal Gas	
<b>Sokolov and Hershgal (1990b) Part 2</b>	x			N/A	x		x		x		Optimization of ejector refrigeration cycle; commentary of the importance of heat exchanger sizing
<b>Eames <i>et al.</i> (1995)</b>	x			Water	x			x	x	x	First paper to establish well-defined operating curves of an ejector refrigeration cycle given a specific ejector geometry
<b>Huang <i>et al.</i> (1999)</b>	x		x	R141b	x		x		x	x	Detail of semi-empirical equations for ejector modeling; experiments calculate isentropic efficiency values used in subsequent studies
<b>Rogdakis and Alexis (2000)</b>	x			Ammonia	x			x			Parametric analysis of ejector refrigeration cycle
<b>Zhang and Wang (2002)</b>	x			Zeolite-water	x		x			x	Combines adsorption system with ejector refrigeration cycle to produce hot water at 45 °C and air conditioning; derives transient models of components
<b>Guo and Shen (2009)</b>	x			R134a	x			x	x	x	Uses "dynamic mode" to evaluate ejector, finding performance at intervals throughout the day as ambient conditions change
<b>Deberne <i>et al.</i> (1999)</b>		x	x	Water	x				x		Set of equations needs only one empirical value, making equations more independent than the typical 1D model
<b>Cizungu <i>et al.</i> (2001)</b>		x		R123, R134a, R152a, R717	x			x	x		Compares performance with four different environmentally-friendly working fluids; performance depends mostly on ejector geometry and compression ratio
<b>Jelinek <i>et al.</i> (2002)</b>		x		R125-N,N'-dimethylethylurea	x						Models individual droplets in two phase flow, accounts for drag and heat transfer
<b>Lear <i>et al.</i> (2002)</b>		x		R134a	x			x	x		One of first papers to model two-phase choking
<b>Bergander (2006)</b>		x	x	R22	x			x			Focus on modeling condensation shocks; defines need for compressibility term in fundamental equations
<b>Yu <i>et al.</i> (2007)</b>		x		R142b	x		x			x	Provides simplified analysis of two-phase ejector for low-level analysis

**Table 2.2: Component-level analytical modeling studies and key contributions.**

Article	# of Phases		Experimental	Working Fluid	Analytical Model Assumptions						Key Contribution
	1 Phase	2 Phase			1D	2D	Constant P Mix	Constant A Mix	Normal Shocks	Ideal Gas	
<b>Liu and Groll (2008)</b>		x	x	CO <sub>2</sub>	x			x	x		Provides simplified analysis of ejector for low-level analysis
<b>Butrymowicz (2009)</b>		x	x	Air-water	x			x		x	Model for two-phase ejector flow including momentum loss parameter
<b>Zhu et al. (2007)</b>	x			Air		x		x		x	Develops model simpler than most 1D models; accounts for velocity variation within mixing chamber from oblique shock

Another common characteristic is the difference between local and global performance. All of the analytical studies reviewed are primarily concerned with the ability to predict global performance, meaning that they validate results based on global properties such as MER, SPR, and ejector inlet and outlet conditions. Only the studies by Zhu *et al.* come close to predicting local quantities, such as the radial velocity profile of flow inside the mixing section.

Despite efforts to improve upon the Keenan model, a large degree of uncertainty and error still exists in results. Part of this is from a lack of understanding of fundamental flow phenomena, and the source of most losses has been overlooked and addressed by empirical coefficients that are specific to fluid and geometry. Some studies have calculated a few of these losses directly, but the complexity of flow, especially inside the mixing section, is difficult to capture accurately with analytical models. Therefore, many recent studies have turned to the use of CFD to better understand ejector fluid flow phenomena.

### **2.2.2 Numerical studies**

The goal of numerical studies on the ejector component is to reduce the number of, or eliminate assumptions previously necessary to develop analytical models. CFD modeling of ejectors only began recently, as the first detailed models started appearing around 2004. Before this time, there was a desire for such models, as expressed by Sun and Eames (1995), but computing technology limited the ability to do so. When the review paper by Matsuo *et al.* (1999) was written, only a handful of papers had attempted some sort of numerical modeling of shock trains, not specific to ejector operation (Carroll *et al.*, 1993; Hataue, 1989; Lin *et al.*, 1991a, b; Yamane *et al.*, 1995).

Significantly more computing power and sophistication of CFD software appeared later, and has enabled studies that are noticeably more accurate and detailed. Studies are increasingly able to incorporate the use of better turbulence models, finer adapted meshes, and complex geometries. One such study by Desevaux and Lanzetta (2004), based on a previous visualization study (Desevaux, 2001b), uses the CFD package FLUENT to model the flow inside an air ejector with no suction flow, assuming ideal gas behavior. The experimental basis for this comparison came from a novel measuring technique introduced by Desevaux *et al.* (1994) using a capillary tube inserted into the center of the motive flow to measure static pressure distributions along the centerline of the ejector. The best agreement with the experimental data obtained with this method is achieved with the standard  $k$ - $\epsilon$  turbulence model, but with two major discrepancies. The first is that the pressure at the outlet of the motive nozzle is under predicted by about 20%. This is partially attributed to the presence of the capillary tube measurement device and to the condensation of air humidity, both of which were not included in the computational model. As the pressure of the motive flow increases and the effects of condensation become more important, these discrepancies become more prominent. The other discrepancy is the frequency and magnitude of the pressure changes within the motive jet at varying axial positions. Such patterns in centerline pressure are expected from alternating high- and low-pressure regions caused by the reflection of the expansion and shock waves inside the motive jet. The simulation consistently under-predicts the low-pressure regions, whereas the high-pressure regions usually match very well. At higher motive flow pressures, the specific location of each region is slightly off. A major strength of this paper is its ability to accurately predict the motive jet length to within 12%. This is an important value to



know when designing the mixing section because it must be long enough to allow full mixing of the two flows.

More recent work by Bartosiewicz *et al.* (2005) studies the discrepancies found in Desevaux and Lanzetta (2004). A FLUENT CFD model was formulated using an adaptive mesh to increase the number of cells at the ejector walls as well as the locations of large property gradients. The model is validated with pressure measurements taken along the length of the mixing section axis, and from this, the accuracy of shock length, strength, and average pressure recovery is determined. To examine the effect of the turbulence model, six models are compared for the case of no suction flow:  $k$ - $\epsilon$ , realizable  $k$ - $\epsilon$ , renormalized group  $k$ - $\epsilon$  model, RSM,  $k$ - $\omega$ , and  $k$ - $\omega$ -sst. The RNG and  $k$ - $\omega$ -sst models prove to be the best when predicting pressure variation strength, location, and mean pressure, and the  $k$ - $\omega$ -sst model is best to predict the length of the motive jet.

To explore the intrusive effects of the capillary probe, a new mesh that included the probe in the domain geometry was used. It was found to have a small but noticeable effect on the flow at the local level, and the error of the improved model with probe included is about 10% for expansion and 35-50% for compression. As stated by Desevaux and Lanzetta (2004), remaining error is attributed to condensation effects that may result in less extreme maxima and minima in pressure within the motive jet, as seen in experimental results. This sets the stage for further CFD work that incorporates two-phase flow phenomena, specifically condensation effects. It was also found that when the outlet pressure is decreased past the point where secondary flow choking occurs, the MER does not remain constant but instead drops slightly. This effect is attributed to the existence of two modes of suction flow entrainment, one from the development of a low-pressure

region, and the other from interfacial friction. At low motive stream inlet pressures, the motive jet converges after it exits the motive nozzle. As a result, choking of the suction flow happens much further downstream and friction between the two streams is much more prominent because of the large surface area available. For the higher motive stream inlet pressures, the motive jet diverges and is more likely to form an aerodynamic throat for the suction flow, reducing the contact area for friction between the two streams.

With very good global agreement between experimental and numerical results, especially at high motive pressures, the modeling of ejector flow with more modern computational packages has proved itself to be useful. But there are still a few specific problems that must be addressed. One is the improvement of turbulence models, and the other is the understanding of the influence of two-phase flow on flow characteristics.

The effects of two-phase flow were explored experimentally by Al-Ansary and Jeter (2004). Their study used air as the working fluid and included a non-zero suction flow, unlike Desevaux and Lanzetta (2004). The effects of two-phase flow are explored experimentally by adding atomized liquid droplets to the motive flow. Because most ejector losses are the result of a velocity mismatch between the motive and suction flows, the addition of liquid droplets is an effort to reduce the difference in velocity while maintaining motive jet momentum. The single-phase model for their study uses a standard and renormalized  $k$ - $\epsilon$  turbulence model and assumes air behaves as an ideal gas. These simulations show a few very important phenomena that, until this point, had not been captured by any model. First, the alternation between supersonic and subsonic flow in the motive jet is captured along with boundary layer separation in both the motive and suction nozzles. Suction flow choking is also seen with the expansion of the supersonic region over

the entire width of the domain. As mentioned in Section 2.2.1, the vast majority of analytical studies assume the formation of a normal shock at the end of the mixing section and beginning of the diffuser. From the models of Al-Ansary and Jeter, there is no evidence of a normal shock, but instead an oblique shock train, similar to that seen at the exit of the motive nozzle. The suction stream mass flow rate was validated against experimental results for a range of motive stream inlet pressures, and agreement was very good. The local properties, such as motive jet length and axial pressure variation, were not validated and therefore could not be confirmed, but the detail of the model as well as the fact that many previously ignored flow phenomena are accounted for here is promising.

Hemidi *et al.* (2009b) also model ejector flow phenomena in FLUENT using  $k$ - $\epsilon$  and  $k$ - $\omega$ -sst turbulence models, showing that the  $k$ - $\epsilon$  model provides better flow predictions. The accuracy of predictions was found to depend heavily on motive pressure and operational mode (on- or off-design). Similarly, Zhu *et al.* (2009) compare turbulence models by modeling ejector flow with realizable  $k$ - $\epsilon$ , RNG  $k$ - $\epsilon$ , and  $k$ - $\omega$ -sst turbulence models. The RNG  $k$ - $\epsilon$  model predicts the performance best when it is compared with experimental data for a range of primary flow pressures, outlet pressures, and suction flow temperatures, and validation with MER values resulted in less than 9.29% error.

One of the most recent ejector CFD studies by Hemidi *et al.* (2009a) provides an in-depth commentary on the work by Al-Ansary and Jeter (2004) - the only known previous study to have attempted exploration of the experimental effects of two-phase flow on ejectors. An ejector is modeled in FLUENT first using ideal gas air, then air with water droplets in the motive flow, as was done experimentally by Al-Ansary and Jeter (2004). The two-phase simulation includes viscous dissipation and a discrete second phase in the

Lagrangian frame, assuming spherical water droplets. A source term for momentum is included as well as a force balance on liquid droplets that includes drag effects. Two turbulence models were compared,  $k-\varepsilon$ , yielding better results with error mostly less than 10%, and  $k-\omega$ -sst, with errors often more than 20% but with better performance for off-design operation conditions. It is found in the simulations that the addition of water droplets slightly decreases ejector performance.

Through a comparison of findings with Al-Ansary and Jeter (2004), it is indicated that the MER calculation in Al-Ansary and Jeter does not include the water inserted in the motive flow, or the air needed to atomize the water. Furthermore, no correction was made for water that condensed or accumulated within the ejector itself. To mitigate these effects, Hemidi *et al.* (2009a) used an ultrasonic atomizer to generate fine water droplets without the use of additional air. The experimental results show off-design improvement in operation from 10-40% especially with smaller droplets, suggesting that the addition of liquid droplets, which could occur naturally from condensation in the motive nozzle jet, would improve operation. This finding is consistent with that of Al-Ansary and Jeter (2004), and contradicts conventional thought and CFD simulations indicating that condensation would deteriorate performance. It is hypothesized that this increase in performance is due to decreased momentum irreversibilities between the two flows, but also to droplet deposition into a film, annular water spray from nozzle outlet, or spray breakup coming from the film arrachement. Subsequent work has been dedicated to the development of a better two-phase model for ejector flow, including a study by Bulinski *et al.* (2010) that presents a two-phase model of transonic CO<sub>2</sub> ejector flow, comparing heterogeneous and homogenous models of flow to experimental measurements. As of now,

more sophisticated RSM (Reynolds Stress Model) and LES (Large Eddy Simulation) approaches have not been thoroughly explored, although Mazzelli *et al.* (2015) compare RSM simulations of ejector flow to more typical two-equation eddy viscosity approaches.

The studies reviewed above are compiled in Table 2.3, providing a comparison of CFD studies with detail on the turbulence models considered, geometric dimensions, and key contributions from each study.

**Table 2.3: CFD studies of ejector flow phenomena.**

Article	# of Phases		Experimental	Working Fluid	Turbulence Model	Geometry [mm]				Key Contribution
	1 Phase	2 Phase				Nozzle Throat Diameter	Mixing Section Diameter	Diffuser Exit Diameter	Overall Length	
<b>Desevaux and Lanzetta (2004)</b>	x			humid air	Standard $k-\epsilon$ Realizable $k-\epsilon$ RSM	8	24	N/A	240	Combines visualization with CFD study; focus on predicting length of motive jet for proper design of mixing section length within 12%
<b>Bartosiewicz et al. (2005)</b>	x		x	air	$k-\epsilon$ Realizable $k-\epsilon$ RNG $k-\epsilon$ RSM $k-\omega$ $k-\omega$ -sst	N/A	N/A	N/A	~200	Discusses negative effects of boundary layer separation; pressure measurements conducted with capillary tube; in-depth discussion of different turbulence models
<b>Eames et al. (2007)</b>	x		x	R245fa	Constant-rate momentum change method	2.2 and 2.6	7.5	20	265	Shows that R245fa can be used successfully as working fluid for ejector cycle
<b>Zhu et al. (2009)</b>	x		x	R141b (Freon)	Realizable $k-\epsilon$ RNG $k-\epsilon$ $k-\omega$ -sst	2.8	8	14	~120	Uses CFD model to optimize NXP; accurate prediction of global ejector parameters to within 10%
<b>Al-Ansary and Jeter (2004)</b>	x	x	x	air and water droplets	Standard $k-\epsilon$ RNG $k-\epsilon$	7.9	14	20.9	229	Hypothesizes that existence of water droplets would increase ejector efficiency; considers two-phase ejector flow
<b>Hemidi et al. (2009a)</b>	x	x	x	air and water droplets	$k-\epsilon$ $k-\omega$ -sst	3.3	7.6	N/A	22.5	Provides insight into study by Al-Ansary and Jeter (2004); places emphasis on need for two-phase ejector research
<b>Hemidi et al. (2009b)</b>	x		x	air	$k-\epsilon$ $k-\omega$ -sst	3.3	7.6	N/A	22.5	Finds that $k-\epsilon$ model predicts flow best; accuracy has strong dependence on motive pressure and operational mode
<b>Bulinski et al. (2010)</b>		x		CO <sub>2</sub>	RNG $k-\epsilon$	N/A	N/A	N/A	0.1	Compares two-phase CFD results using heterogeneous and homogeneous models

### **2.2.3 Visualization studies**

Visualization of ejector flows has become increasingly popular in an effort to validate existing CFD models and visualize effects that may not be possible to capture with available computational or analytical tools. Many visualization studies in the literature have been conducted for the purpose of understanding internal flow in constant cross-sectional area ducts (Matsuo *et al.*, 1999). Visualization studies pertaining to ejector flow are much less common.

Early visualization studies utilized the classic visualization technique of Schlieren imaging to detect changes in the refractive index of fluid at different densities. The original Keenan *et al.* study (1950) provides a set of sharp images of ejector flows that show the presence of strong 2D shocks propagating from motive nozzle outlet, as well as streamlines of suction flow for different outlet pressures. Dvorak and Safarik (2005) also capture high-quality Schlieren images of ejector flow that are compared with the results of CFD simulations. Matsuo *et al.* (1982) use Schlieren imaging to visualize similar flow structures, but also the presence of bifurcated shocks in both the motive nozzle and diffuser sections. Schlieren imaging has also been used for visualization of ejectors for other applications, such as in the study by Zare-Behtash *et al.* (2011) where a motive jet was studied for thrust augmentation applications.

Other than Schlieren imaging, two key studies by Desevaux *et al.* (Desevaux, 2001a, b) use different visualization methods to observe ejector flow with humid air. Visualization is performed using two different types of tracers with laser sheet illumination using an Argon laser. The first type of tracer is natural condensation droplets, using

Rayleigh scattering to detect their location. Unfortunately, because condensation occurs in the mixing region only, this was the only part of the flow that could be visualized. The second type of tracer is fluorescent particles added to the suction flow, where dark regions indicate locations where there has not yet been mixing with the suction flow. The set of images provided in the paper compare the images using the two different tracers side by side, as well as images that result from transformation techniques used to accentuate flow characteristics. A later study by Bouhanguel *et al.* (2011) uses oil droplets to seed the flow, and presents some images that display inherent instabilities and turbulent structures in the motive jet.

These images do show the general shape of the motive jet, and are therefore sufficient to determine its length. But the location and existence of specific compressions and expansions is not clear. Furthermore, this visualization method does not work for cases with higher suction flow rates because the light intensity of the tracer particles is not high enough for clear imaging. Also, as already mentioned, the natural tracers relied on condensation of the flow that was only present in the mixing region. Therefore, these methods for visualization are promising, but still suffer from many limitations.

Since the work of Bouhanguel *et al.*, this visualization technique has been improved and enhanced by Rao and Jagadeesh (2014), combining the use of time-resolved Schlieren and laser scattering images to characterize mixing in the ejector and detect oscillations in the position and shape of shock cells. Images are detailed and able to resolve specific flow features inside the motive jet.



Although not strictly for the study of ejectors, other work by Alkislar *et al.* (2003) and Moreno *et al.* (2004) uses state-of-the-art stereoscopic PIV (particle image velocimetry) methods to visualize the structure of a supersonic screeching rectangular jet. In Alkislar *et al.*, the spatial and temporal evolution of the jet is realized, as well as turbulence quantities and deformation of flow structures. Moreno *et al.* uses these data to obtain approximate models of such jets using the proper orthogonal decomposition (POD) technique. A review of such PIV techniques for supersonic flows can be found in the review paper by Scarano (2008).

These PIV techniques have been shown to provide impressive images of supersonic jets, but they have yet to be applied specifically to ejector flow. Schlieren imaging has also proven to be a useful diagnostic visualization method, but has not been fully exploited to visualize ejector flow. Therefore, development of visualization methods must continue for reliable validation of flow phenomena predicted by CFD studies.

## **2.3 Ejector Systems**

Ejectors have been used in a wide variety of systems because of their properties as low maintenance passive devices with no moving parts, and the ability to reduce or completely eliminate compressor load. Of interest in this review is application in chiller systems, specifically the basic configuration shown in Fig. 1.5 (a). This section reviews papers that have explored this ejector-based chiller configuration and its variations, concluding with an evaluation of the state-of-the-art, and the potential future and usefulness of these cycles.

### **2.3.1 Ejector-based chillers**

The ejector-based chiller cycle, shown in Fig. 1.5 (a) is the most common application for ejectors in cooling systems. Many studies have focused on modeling, fabricating, and

studying the effects of varying parameters on ejector-based chiller configuration. The scientists credited with the first development of this cycle are LeBlanc and Parsons in 1901 (Elbel and Hrnjak, 2008). Since then, many studies have focused on parametric analyses of the ejector-based chiller to determine its sensitivity to fluctuating source, sink, and ambient conditions, and to best design ejector and heat exchanger components for optimized operation. One such study by Rogdakis and Alexis (2000) finds that at a constant evaporator temperature, the COP increases with an increase in generator temperature and decrease in condenser temperature. This is an important and common result from studies on ejector-based chillers. Cizungu *et al.* (2001) perform a parametric analysis on the ejector-based chiller, including the effects of varying  $\phi$ , the ratio of mixing section to motive nozzle throat cross-sectional area, and different working fluids. Similar to the findings of Rogdakis and Alexis (2000), the cycle COP is found to decrease with increase in compression ratio. This is because at a fixed condenser temperature, an increase in evaporator temperature reduces the ejector SPR, or the needed pressure lift for the bottoming cycle.

A study by Grazzini and Rocchetti (2002) augments the ejector-based chiller such that the boiler feeds into the ejector through two motive inlets. An optimization scheme is developed that not only includes ejector parameters, but heat exchanger design parameters and temperature differences within them. At relatively high boiler temperatures of 109°C and 120°C, the COP is 0.131 and 0.53, respectively, when using R718. Furthermore, the evaporator heat exchanger design has a strong influence on system COP, and low heat exchanger efficiencies can be tolerated for the condenser and boiler while still maintaining the best COPs. A later study by Grazzini *et al.* (2012) develops a design procedure for an

ejector-based chiller, accounting for both heat exchangers and the ejector itself, and providing a comparison of first and second law efficiency performance with different working fluids. Another optimization is performed by Dahmani *et al.* (2011), taking into account parameters of boiler refrigerant pressure and temperature difference in the heat exchangers for operation with R134a, R152a, R290, and R600a.

The importance of heat exchanger design is also emphasized by Bejan *et al.* (1995) with a focus specifically on condenser design. The study finds the optimal way to divide a specified heat exchanger surface area between the three heat exchangers in an ejector-based chiller to get the highest cooling load. They conclude that the condenser requires half of the available heat exchanger UA, independent of the ratio of boiler temperature to ambient temperature, or the ratio of evaporator temperature to ambient temperature.

Yapici and Yetişen (2007) built a full ejector-based chiller system for use with source temperatures between 90 and 102°C using R11. A parametric analysis is performed on evaporator, condenser, and boiler temperatures, and results similar to those from the studies listed above are found. Their study also examines the effect of using the ejector at off-design conditions on cycle COP. Eames *et al.* (2007) perform a similar experimental study using R245fa. This fluid is of particular interest because it is an organic fluid that has desirable traits such as low global warming potential as well as lower boiling temperatures and pressures, making it a likely future choice for use in systems that use low source temperatures. This study is valuable because it presents performance contours specifically for R245fa, showing COPs between 0.25 and 0.7 for boiler temperatures between 100 and 120°C, and utilizing some regenerative heat exchange within the ejector-based chiller cycle. Emphasis is given to the proper design of an ejector-based chiller such that the

critical pressure, as defined in Fig. 1.4, is reached at the condenser. This means that the pressure in the condenser (i.e., the outlet pressure of the ejector) should enforce critical conditions in the ejector such that choking conditions are met.

Huang *et al.* (1985) examine the effects of regenerative heat exchange in an ejector-based chiller through a direct comparison of two operational modes on the same system. The performance curves show that on average, the COP is better using regenerative heat exchange, especially at low evaporator temperatures and high generator and condenser temperatures. For example, at boiler, condenser, and evaporator temperatures of 80, 30, and 15°C respectively, the COP with and without regenerative heat exchange is about 0.14 and 0.11, respectively.

Guo and Shen (2009) developed an analytical model of a 6-kW ejector-based chiller operating with R134a, focusing on a specific application for an office building during working hours between 8 AM and 4 PM. A low boiler temperature of about 85°C (from vacuum tube solar collectors), an evaporator temperature of 8°C, and an ambient condenser temperature varying throughout the day (28 - 34°C) are used. It is found that the formation of shocks in the ejector results in an energy loss and decreased performance at boiler temperatures above the design point. Furthermore, condenser temperature has greater effect on performance than does boiler temperature. Considering the efficiency of solar collectors, heat loss from the storage tank and piping, and heat transfer efficiencies in the boiler, they predict an unusually high average COP of 0.48 between 8 AM and 4 PM, assuming idealized entrainment conditions inside the ejector. Pollerberg *et al.* (2009) perform a similar study that examines the transient response to the varying conditions experienced by an actual system. The model includes parabolic trough collectors, solar

energy storage, the potential use of cascaded ejectors, and the typical ambient and boiler temperature fluctuations during one day of operation. A 1-kW system using water as the working fluid with an evaporator temperature of 6°C is modeled first, followed by experimental validation with a full system with good agreement. The model is then scaled to a more realistic 100-kW case with emphasis on startup and dynamic system performance.

Pollerberg *et al.* point out that no ejector-based chillers have yet been implemented in industry. The extent of practical application has been small, table-top systems to validate analytical models. The main purpose for their study, and also the motivation behind Guo and Shen (2009), is to discuss the use of ejector-based chillers for many applications, and to address practical concerns such as startup and stable operation, which would lead to technological viability of such systems.

### **2.3.2 Ejector-based chiller configuration variations**

Among waste heat recovery techniques, the ejector-based chiller is an excellent candidate for cooling applications. Yet the relatively low COPs of this system, usually around 0.2, leave questions about whether or not it will see widespread use. A series of three papers by Sokolov and Hershgal (Sokolov and Hershgal, 1990a, b, 1991) discusses the relative merits of the ejector-based chiller against the more efficient and widely used vapor compression cycle. Part 1 (Sokolov and Hershgal, 1990a) compares a vapor compression and ejector-based chiller cycle run between the same source and sink temperatures. It is found that the latter must run at conditions that are close to optimum without much freedom in source, sink, or ambient temperature fluctuations to be as competitive as possible with vapor compression systems. To overcome this challenge, a few changes to the basic

ejector-based chiller cycle are presented. The first is the boosted ejector-based chiller that adds a booster (or compressor) before the suction flow inlet to the ejector to provide a two-stage compression of that stream. This results in a higher MER and higher COP because less pressure rise is required in the ejector, although at the cost of electrical input and system complexity. The other change is to add a bottoming vapor compression cycle coupled to the evaporator of the basic ejector-based chiller cycle. With this, the capacity of the intercooler can compensate for fluctuations in working conditions, and if the intercooler combines heat and mass transfer, the bottoming cycle can provide pre-conditioned interbalancing effects. Finally, a combination of these two changes can be used in a hybrid cycle.

Sokolov and Hershgal (1990a) provide a comparison of these cycles. For example, using the same refrigerant R114 in the basic cycle, the same source, cooling, and ambient temperatures at 86, -8, and 30°C respectively, and a booster compression ratio of 2.08, the COP of the basic vapor-jet refrigeration, boosted, and hybrid cycles are 0.252, 0.767, and 0.812 respectively (using R22 in the vapor compression bottoming cycle). The boosting alone provides an increase in COP of over 300%, and adding the bottoming vapor compression cycle helps raise the COP by another 20%. Of course, the inherent disadvantages of these measures are that electrical energy input would be needed to power the compressor(s), and the superheating needed for fluid passing through the booster would add an extra load to the condenser. Furthermore, the addition of a bottoming vapor compression cycle would add another heat exchanger, compressor, and expansion valve, all of which add to initial and operating costs.

Part 2 (Sokolov and Hershgal, 1990b) primarily addresses ejector design and optimization, but also includes a section discussing optimization of the boosted ejector-based chiller. As shown by many other studies, an increase in condenser temperature and pressure decreases system COP and necessary condenser heat exchanger area, but increases the mechanical work needed by the booster. The study also explores the use of cascaded ejectors. In a cascaded ejector setup, multiple ejectors of different geometry are connected in parallel, as shown in Fig. 2.1. A valve selects the ejector that is used at the given operating conditions such that the chosen ejector operates at on-design, or near-on-design conditions. This allows for an ejector-based chiller design that is versatile because it allows for the wide range of source, sink, and ambient operating conditions found in practical applications.

Finally, in Part 3 (Sokolov and Hershgal, 1991), the ejector-based chiller with boosting, double-cascaded ejectors, and some internal heat exchange is designed and

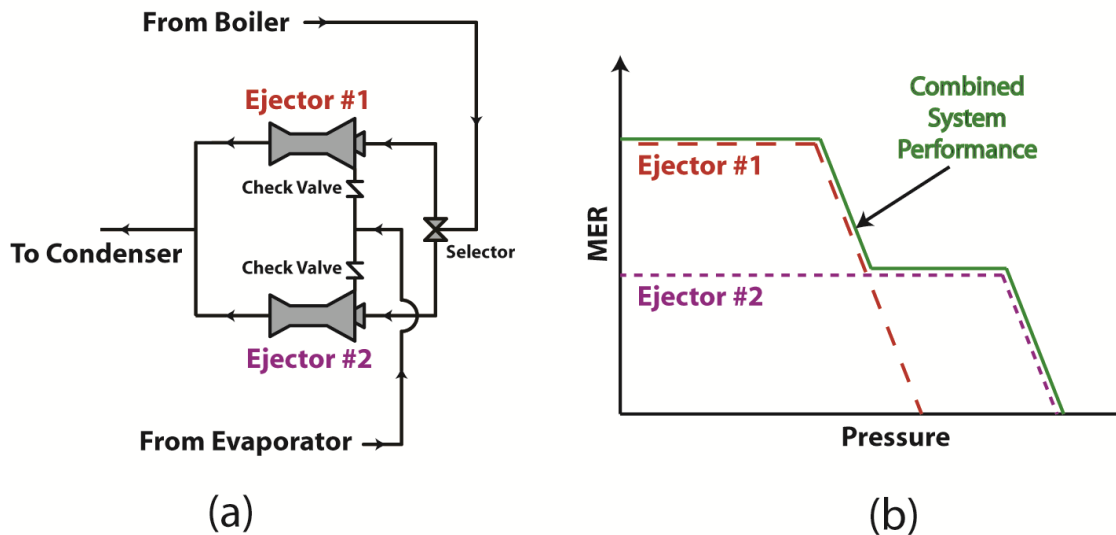


**Figure 2.1: (a) Schematic of a double cascaded-ejector setup, and (b) the resulting composite operating curve as a superposition of the MER vs. outlet pressure graph for each ejector.**

constructed to a refined operational level. Startup, steady-state, and shutdown operation is successfully performed with the necessary controls and a simple “on-off” switch for the air-conditioning unit. With boiler, condenser, and evaporator temperatures of about 93, 53, and 9°C respectively, and R114 as the working fluid, COPs of 0.417 and 0.321 with cooling loads of 2930 and 2051 W, respectively, are realized for two different operating conditions depending on the ejector used in the cascaded system. With a total mechanical work input of about 500 W, this system results in highly efficient use of electrical energy.

A subsequent paper by Arbel and Sokolov (2004) examines the basic ejector-based chiller with the bottoming vapor compression cycle only. Because the original R114 refrigerant considered is now unavailable, a new refrigerant R142b is tested as an alternative. The new refrigerant is found to perform better than R114 with an overall COP of 1.085 at boiler, condenser, and evaporator temperatures of 99.5, 40, and 4°C, respectively.

These cycles all prove to be better than the basic ejector-based chiller in terms of COP, and have been developed to an advanced level as demonstrated by Sokolov and Hershgal (1991). But these improvements come at the price of both initial equipment costs and operation costs needed to run the compressors, and increased system complexity.

### **2.3.3 Passive Systems**

Although the typical configuration of an ejector-based chiller eliminates the need for a compressor, a circulating pump is still necessary. Some investigators have studied modifications to the basic cycle that eliminate the need for this mechanical work input. Such cycles allow off-grid application with a relatively simple design. Nguyen *et al.* (2001) designed a passive system to provide 7 kW of cooling to an office building without the use



of mechanical energy or moving parts. The need for a feed pump is eliminated by establishing a large gravity head between the condenser and the generator to produce the required pressure difference. The required height, using water as the working fluid, is seven meters. The system is designed for boiler, condenser, and evaporator temperatures of 90, 35 and 10°C, respectively, and the actual on-site installation runs at a boiler temperature of 80°C, varying ambient temperatures, and a 1.7°C evaporator temperature with a COP of 0.3. Startup, steady-state, and shutdown operation is performed successfully with some controls that actuate a valve and air fan at appropriate times.

Alternatives to the use of gravity head for fluid circulation have been explored because of the difficulty in implementing large height differences between the boiler and condenser. Srisastra *et al.* (2008) address this by replacing the mechanical feed pump with a storage tank and set of valves. A cyclic process fills the tank with condensate from the condenser, charges the tank with high-pressure vapor from the boiler, and then uses that pressure and gravity head between the tank and the boiler to discharge liquid into the boiler. This process is known as Workless Generator Feeding (WGF). Experimental results show that, in comparison to the basic vapor-jet refrigeration cycle using a mechanical feed pump, 10 to 15% more heat input is needed at the boiler to account for the heat lost in the storage tank thermal mass as it is reheated during each cycle. Furthermore, as the frequency of operation increases, so does the necessary heat input at the boiler. For boiler and evaporator temperatures of 105 and 10°C respectively, an operational frequency of 25 cycles/hour, and at condenser pressures low enough to cause choking in the ejector, the COP of the system with two feeding tanks operating in parallel is about 0.18. The basic system with the mechanical pump has a COP of about 0.21.

A similar study by Srisastra and Aphornratana (2005) uses a WGF system with water (instead of the R141b used by Srisastra *et al.* (2008)), and the performance of this system was comparable to that of the basic mechanical system. This is because the higher heat of vaporization of water allows for a lower working fluid flow rate to accomplish the same amount of cooling. Therefore, a lower frequency of operation can be used, which was shown by Srisastra *et al.* (2008) to improve performance.

Huang *et al.* (2006) use a Multi-Function Generator (MFG) to eliminate the need for a mechanical pump. Much like the WGF process (Srisastra and Aphornratana, 2005; Srisastra *et al.*, 2008), each individual MFG operates in a cyclic fashion. This study describes the use of two MFGs, set to operate out of phase with each other, such that the combination of the two is able to provide a constant cooling load. Solenoid valves are used to activate the operation of the two MFGs, and four additional check valves control other processes. A proof-of-concept unit using R141b is built with a single MFG, and boiler, condenser, and evaporator temperatures of 90, 32.4, and 8.2°C, respectively. The MFG cycle generates 0.786 kW of cooling with a COP of 0.185 at these conditions. Results show that at a constant evaporator temperature, increasing boiler temperature results in lower COP, but at the same time, condenser pressure can be increased to allow for operation at varying ambient conditions. Wang *et al.* (2009) extended this work by using two MFGs, and the necessary controls to maintain steady operation. At boiler, condenser, and evaporator temperatures of 90, 37, and 8.5°C respectively, a COP of 0.19 is realized for 0.75 kW of cooling. The use of refrigerant R365mfc is tested as an alternative to R141b, but shows no change in performance with appropriate redesigning of the ejector.

These systems have been developed and tested with startup and steady-state operation. Small amounts of electrical input are needed to power controllers and valves, but because of the small electrical demand of these components, the power could be supplied by a battery or solar photovoltaics. All systems also use liquid-cooled condensers that require a pump for the coupling fluid and a fan for heat rejection to air, as necessary. It appears that such nearly passive systems could be implemented in selected off-grid applications.

The papers discussed in this section are summarized in Table 2.4, indicating the types of cycles considered, working fluids and conditions, and operating COPs. A visual representation of the investigations of the ejector-based chiller and its variants is given in Fig. 2.2, organized based on COP and lift, defined as the difference between condenser (ambient) and evaporator (cooling) temperatures. It can be seen that source temperatures <

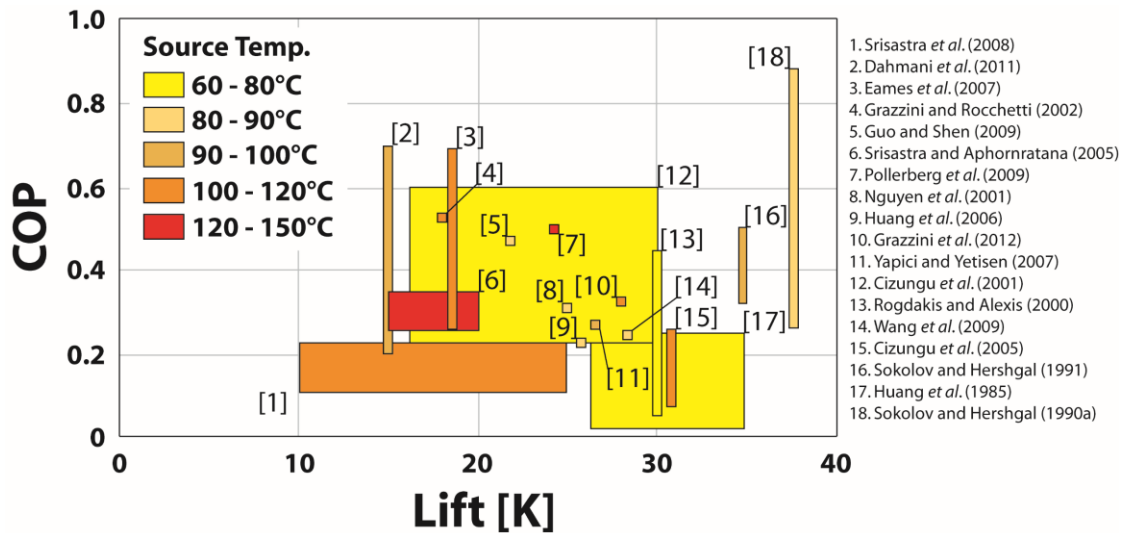


**Figure 2.2: Comparison of ejector-based chillers studies including boosted, bottoming VC, and passive systems derivatives. Lift is defined as the difference between condenser (ambient) and evaporator (cooling) temperatures. Studies are color-coded based on the boiler (source) temperature used. In some cases, the peak COP is reported, and in others a range of conditions is given as part of a parametric study.**

100°C are typically used, and COP is typically around 0.4 at a lift of about 25 K (e.g., a cooling temperature of 5°C at an ambient temperature of 30°C). The best performance is realized by cycles benefiting from a bottoming VC or boosters, as in Sokolov and Hershgal (Sokolov and Hershgal, 1990a, 1991). The lowest performance is more typical of passive systems, even at higher driving source temperatures, such as those by Srisastra *et al.* (Srisastra and Aphornratana, 2005; Srisastra *et al.*, 2008), but with the benefit of requiring little external electrical or mechanical energy input.

**Table 2.4: System-level studies. Source and cooling temperatures, as well as operational COP values are given for each study, along with key contributions.**

Article	Ejector Cycle						Working Fluid	Experiment	Global Cycle Properties		COP	Key Contribution
	Basic	Bottoming VC	Boosted	Augmented VC	Passive	Other			T Source [°C]	T Cooling [°C]		
<b>Bejan <i>et al.</i> (1995)</b>	x						N/A		N/A	N/A	N/A	Detailed study of heat exchanger footprint allocation in ejector-based chillers to attain highest COP or lowest cost
<b>Rogdakis and Alexis (2000)</b>	x						Ammonia		76.11 to 79.57	4 to 12	0.05 to 0.45	Parametric analysis of ejector refrigeration cycle
<b>Cizungu <i>et al.</i> (2001)</b>	x						R123, R134a, R152a, R717		60 to 80	-0.5 to 13.5	0.22 to 0.6	Compares performance of four different low GWP fluids; performance depends mostly on ejector geometry and compression ratio
<b>Grazzini and Rocchetti (2002)</b>	x						R718		120	12	0.529	Detailed optimization strategy accounts for ejector geometry and cycle parameters; study of three-port ejector
<b>Grazzini <i>et al.</i> (2012)</b>	x						R245fa		115	7	0.325	Develops design procedure accounting for both heat exchanger and ejector parameters
<b>Dahmani <i>et al.</i> (2011)</b>	x						R134a, R152a, R290, R600a		95	5	0.2 to 0.7	Optimization including boiler refrigerant pressure and temperature differences in heat exchangers
<b>Cizungu <i>et al.</i> (2005)</b>	x						Ammonia Ammonia-Water		70 to 126	4	0.08 to 0.26	Optimization strategy for designing ejector component; considered single- and two-component mixtures
<b>Yapici and Yetisen (2007)</b>	x						R11	x	90 to 102	0 to 16	0.25	Parametric analysis of ejector refrigeration cycle
<b>Eames <i>et al.</i> (2007)</b>	x						R245fa	x	120	15	0.25 to 0.7	R245fa found to be a viable refrigerant for the ejector-based chiller; performance maps included for system design

**Table 2.4: System-level studies. Source and cooling temperatures, as well as operational COP values are given for each study, along with key contributions.**

Article	Ejector Cycle						Working Fluid	Experiment	Global Cycle Properties		COP	Key Contribution
	Basic	Bottoming VC	Boosted	Augmented VC	Passive	Other			T Source [°C]	T Cooling [°C]		
Huang <i>et al.</i> (1985)	x						Freon-113	x	65 to 80	5.2 to 14.9	0.05 to 0.25	Direct comparison of ejector-based chiller performance with and without regenerative heat exchange
Guo and Shen (2009)	x						R134a		85	8	0.48	Uses "dynamic mode" to evaluate ejector; performance evaluated at intervals throughout a typical day
Nguyen <i>et al.</i> (2001)	x				x		water	x	90	10	0.3	Gravity head used to eliminate need for feed water pump in ejector-based chiller cycle
Pollerberg <i>et al.</i> (2009)	x						water	x	150	6	0.5	1-kW ejector-based chiller cycle built and tested; transient system model
Sokolov and Hershgal (1990a) Part 1	x	x	x				R114		86	-8	0.252 to 0.860	Changes to basic ejector-based chiller to attain COP values competitive with vapor compression system
Sokolov and Hershgal (1990b) Part 2			x				N/A		N/A	N/A	N/A	Optimization of ejector-based chiller cycle; commentary of the importance of heat exchanger size
Sokolov and Hershgal (1991) Part 3			x				R114	x	98.3	8.8	0.417 and 0.321	Cycle includes controls to adapt to different generator temperatures
Bergander (2006)				x			R22	x	N/A	N/A	4.9 and 3.53	Explores relationship between two-phase flow and shock formation and behavior; reports 38% theoretical improvement over conventional vapor compression cycle
Chaiwongsa and Wongwises (2007)				x			R134a	x	26.5 to 38.5	8 to 16	2.5 to 6	Explores effects of motive nozzle throat diameter on performance; demonstrates capabilities of augmented vapor compression cycle
Arbel and Sokolov (2004)		x					R142b		100 to 106	4	0.32 to 1.52	Lower GWP refrigerant R142b produces better results than R114; includes details of solar panel design

**Table 2.4: System-level studies. Source and cooling temperatures, as well as operational COP values are given for each study, along with key contributions.**

Article	Ejector Cycle						Working Fluid	Experiment	Global Cycle Properties		COP	Key Contribution
	Basic	Bottoming VC	Boosted	Augmented VC	Passive	Other			T Source [°C]	T Cooling [°C]		
Huang <i>et al.</i> (2006)					x		R141b	x	90	8.2	0.218	Developed MFG (multi-function generator) and successfully tested experimentally
Srisastra <i>et al.</i> (2008)					x		R141b	x	90 to 120	5 to 20	0.12 to 0.21	Developed WGF (workless generator feeding) cycle and successfully tested experimentally
Srisastra and Aphornratana (2005)					x		Water	x	110 to 140	5	0.25 and 0.35	Compares WGF operation with water to basic system with mechanical pump
Wang <i>et al.</i> (2009)					x		R141b and R365mfc	x	90	8.5	0.225	Develops switching technique for MFG system from Huang <i>et al.</i> (2006); shows R365mfc can perform as well as R141b
Yu <i>et al.</i> (2007)						x	R142b		90	5	0.24	Cycle includes subcooling loop with a second ejector to increase system COP
Wu and Eames (1998)						x	LiBr-Water	x	198	5	1.2	Novel ejector absorption cycle that compresses high pressure stream to produce more steam
Jelinek <i>et al.</i> (2002)						x	R125-N,N'-dimethylethylurea		70 to 140	-10 to 0	0.35 to 0.595	Uses ejector in triple-pressure absorption cycle; 20% performance increase in comparison to typical absorption cycle
Sözen and Özalp (2005)						x	Ammonia-Water		90	5	0.739	Cycle model used with detailed solar data from various locations in Turkey to determine necessary solar panel area
Zhang and Wang (2002)						x	Zeolite-water		100	5	0.33	Combines adsorption system with ejector-based chiller to produce hot water and air conditioning; transient models of components

## **2.4 Future Work**

The understanding of ejector operation, design, and flow phenomena has come a long way since the first major analytical model on ejectors in the Keenan studies (Keenan and Neumann, 1942; Keenan *et al.*, 1950). The CFD-based studies for detailed modeling of motive jet and suction flow choking have shown a very detailed modeling of flow phenomena. But there are a few unresolved issues that need further investigation.

### **2.4.1 Understanding and Modeling Shock Phenomena**

In the review paper by Matsuo *et al.* (1999) on shock train and pseudo-shock phenomena in internal gas flows, it is specifically stated that shock phenomena are not well understood despite a large research effort, and that unsolved problems can be answered with more systematic experiments and sophisticated numerical calculations. Since 1999 when the Matsuo *et al.* review paper was written, some of this work has appeared in the CFD studies reviewed in Section 2.2.2. Many shock phenomena have been captured, including successive compressions and expansions in the motive jet, suction flow choking, and changing position of these shocks with change in operating conditions. These are all factors important in determining ejector performance, and can only realistically be captured through detailed CFD models. Al-Ansary and Jeter (2004) state that the common normal shock assumption made in many 1D models overestimates the loss of pressure recovery in the mixing section, and that CFD studies are necessary to attain acceptable accuracy. Despite these advances in CFD modeling, it is still difficult to pick an appropriate turbulence model, and even the best turbulence models have not been fully successful in accurately predicting flow characteristics, as pointed out by Desevaux and Lanzetta (2004) and Bartosiewicz *et al.* (2005). This indicates that alternate methods should be used to model ejector flow, including RSM and LES approaches that are better able to capture the



underlying physics of the ejector flow directly. Furthermore, under conditions where there is the potential for two-phase flow, the prediction of such flow features is considerably more difficult.

#### **2.4.2 Two-Phase Flow**

One of the areas of active discussion is the effect of two-phase flow on ejector performance. Investigators have only recently included the presence of two phases in governing equations for mass, momentum, and energy balances, as shown in Hemidi *et al.* (2009a) and Bulinski *et al.* (2010). However, predicted trends are often opposite to those obtained through experiments. Many early studies, especially those using 1D analytical models to study single-phase flow, predict that condensation inside the ejector would have a negative effect on performance. They state that liquid droplets could obstruct flow through subcomponents, especially the motive nozzle throat. The liquid droplets could also damage certain subcomponents (ASHRAE, 1983; Chen *et al.*, 1998) or increase losses from the separation of two-phase flow that tends to occur in ducts of changing cross-sectional area. To avoid these presumed problems, some studies have examined the effect of superheating the motive flow to avoid the possibility of condensation. Huang *et al.* (1999) found that superheating does not influence ejector performance, whereas Sokolov and Hershgal (1990a) and the ASHRAE equipment handbook (1983) state that superheating would be detrimental to performance. However, Bergander (2006) states that two-phase ejectors are more efficient than their single-phase counterparts, and experiments performed by Al-Ansary and Jeter (2004) and Hemidi *et al.* (2009a) have both found that there is an increase in off-design performance with the presence of small liquid droplets in the motive flow.

These two-phase phenomena have been challenging to study because the specific location and extent of condensation effects is largely unknown, especially for the range of nozzle inlet conditions, back pressures, and fluids found in ejectors. The lower pressure that is accompanied with higher velocity flow could cause condensation in the motive nozzle as expansion into the vapor-liquid dome occurs, and the change in properties across a shock could result in a significant change in quality. If metastable states are also taken into account, these effects become even more difficult to predict. Berana *et al.* (2009) study these effects, specifically of two-phase flow on shocks in converging-diverging nozzles, with an exploration of nonequilibrium effects. Bakhtar *et al.* (2005) provide a more general discussion of metastable states and classical droplet nucleation theory, but without specific application to ejectors. These studies have provided some insights; however, there has yet to be a rigorous study that examines the specific conditions at which condensation occurs, and the effects of different degrees of condensation on overall ejector performance under expected operating conditions.

## **2.5 Conclusions**

Ejectors have been found to be useful for a variety of applications as a passive pumping device. Originally used to replenish water reservoirs in steam engine boilers, they have become popular for many other applications, especially for chiller technology. The advantage of such a device is that little external mechanical input is necessary, making operational costs significantly less than those for typical vapor compression refrigeration systems. Furthermore, the absence of moving parts allows for easy maintenance and operation, and reduces or entirely eliminates the need for a compressor.

Due to the presence of two inlet streams, supersonic flows, and changing cross-sectional area, the flow phenomena inside ejectors are very complicated and difficult to model analytically, especially for the typically wide range of operating conditions and fluids. Early efforts to model ejectors were all analytical, with the first modeling treatment by Keenan and Neumann (1942) and Keenan *et al.* (1950). These early models are all 1D, and many of them assume ideal gas, normal shocks, and/or isentropic flow. Although later analytical models were able to predict global (inlet and outlet) properties more accurately by accounting for additional flow phenomena such as suction flow choking from the formation of an aerodynamic throat, or losses due to shocks, mixing, or friction, the precise flow patterns inside the ejector could still not be captured.

As the limitations of analytical modeling were reached, more insightful and accurate CFD models emerged, with progressively increasing detail through better turbulence models and finer computational meshes. CFD models are now able to capture motive jet features, suction flow choking, and flow separation on the local scale. In comparison with experimental results, some inaccuracies are found, especially when predicting static pressure variations within the motive jet. These inaccuracies are attributed to error in the turbulence models used, as well as the presence of two-phase flow inside the ejector that has not yet been accurately captured with available CFD tools.

In the vast majority of the studies in the literature, two-phase effects have been ignored or assumed to be negligible. For those few studies that have considered two-phase flow effects, conclusions have diverged. Studies such as those by Al-Ansary and Jeter (2004) and Hemidi *et al.* (2009a) have attempted modeling and experimentation with two-phase flow without appreciable success, pointing to a need for better understanding of the

effects of two-phase flow. Such work may include the examination of two-phase flow effects on ejectors with detailed visualization experiments to determine the relative importance of phenomena such as droplet formation, film deposition, and film arrachement.

Beyond the focus on ejector flows, the role of ejectors at the system level has also been explored. The COP of ejector-based chillers is usually in the range of 0.2 to 0.3 with source temperatures between 80 and 100°C to provide cooling between temperatures of 5 and 12°C. In comparison to the COP of a typical vapor compression cycle operating between the same ambient and cooling temperatures, these values are very low, primarily due to large losses inherent in the ejector flow. These systems have been built and tested for startup, steady-state, and shutdown sequences, demonstrating sustainable operation with proper valve controls. Ejectors have also been used for increasing the COP of absorption and vapor compression systems by recovering energy typically lost in expansion valves.

Because ejector operation can be sensitive to fluctuations in inlet conditions and back pressure, precise design of ejectors is needed for accurate predictions of system performance under realistic conditions where the source, ambient, or sink temperatures may fluctuate (especially for the common case where solar heat is used to drive the cycle). This necessitates precise ejector modeling that takes into account all flow phenomena. Therefore, research must concentrate on predicting the effects of shocks, and especially the effects of two-phase flow on ejectors. The understanding of internal flows in ejectors and their implementation in chillers has been steadily improving, but fine-tuning is still necessary, especially to identify and characterize their performance in appropriate niche

applications, such as off-grid systems, where electricity is not readily available, and maintenance-free operation is critical.

From the above review of the pertinent literature, the objectives of the present study are as follows:

1. Develop a method to visualize flow inside an ejector operating with refrigerant at temperatures and pressures representative of ejector-based chiller operation. Use this flow visualization to validate the accuracy of various numerical models, and help better determine the nature of shock phenomena in ejector flows.
2. Develop a model that is able to determine the effects of two-phase flow on ejector operation.
3. Determine whether the presence of two-phase flow has positive or negative effect on overall ejector-based chiller performance. Use this information to make suggestions for best optimization of ejector geometry and operational parameters.

## CHAPTER 3

### VISUALIZATION AND VALIDATION OF EJECTOR FLOW FIELD WITH COMPUTATIONAL AND FIRST-PRINCIPLES ANALYSIS

In an effort to obtain insights into ejector flow phenomena, and to evaluate the effectiveness of commonly used computational and analytical tools in predicting ejector conditions, this chapter presents a set of shadowgraph images of flow inside a large-scale air ejector, and compares them to both computational and first-principles-based analytical models of the same flow. The computational simulations used for comparison apply  $k$ - $\epsilon$  RNG and  $k$ - $\omega$  SST turbulence models to 2D, locally-refined rectangular meshes for ideal gas air flow. A complementary analytical model is constructed from first principles to approximate the ejector flow field. Results show that on-design ejector operation is predicted with reasonable accuracy, but accuracy with the same models is not adequate at off-design conditions. Exploration of local flow features shows that the  $k$ - $\omega$  SST model predicts the location of flow features, as well as global inlet mass flow rates, with greater accuracy. The first-principles model demonstrates a method for resolving the ejector flow field from relatively little visual data, and shows the evolving importance of mixing, momentum, and heat exchange with the suction flow with distance from the motive nozzle exit. Such detailed global and local exploration of ejector flow helps guide the selection of appropriate turbulence models for future ejector design purposes, predicts locations of important flow phenomena, and allows for more efficient ejector design and operation. The visualization technique, as well as the numerical and first-principles models developed here are employed to obtain insights into ejector phenomena, as described in subsequent chapters.

### 3.1 Introduction

Being able to predict ejector flow phenomena has been challenging, both in terms of modeling the flow phenomena accurately, and in being able to validate model results. The small sizes of ejectors as well as the high operating pressures have typically made optical access difficult. This chapter provides data taken on a large-scale ejector test setup specifically designed for visualization purposes, and compares these data with predictions from computations and a first-principles analysis.

A basic shadowgraph imaging technique is used to compare experimental ejector flow with detailed CFD simulations using common turbulence modeling packages in ANSYS FLUENT. A subsequent combination of CFD simulation data and a first-principles analysis provides a method for resolving the ejector flow field from visual data alone, and allows for the identification of flow non-idealities. To the authors' knowledge, this is the first study that attempts to make quantitative measurements from visual images, and uses these quantitative measurements to produce a detailed commentary on specific flow features and interactions inside the ejector motive jet. This insight, paired with an evaluation of turbulence models, provides valuable guidance on how turbulence modeling can be adjusted for most accurate flow prediction.

The experiments, simulations, and models presented here are for an ejector with a rectangular cross-section, whereas most ejectors in previous studies had circular cross-sections. It is possible that the cross-sectional geometry of the ejector has an impact on ejector flow characteristics, as is mentioned later in this study. But to minimize these impacts, the ejector used for this study was designed so that the contact area between the motive and suction streams is approximately equal to that of an ejector of the same capacity

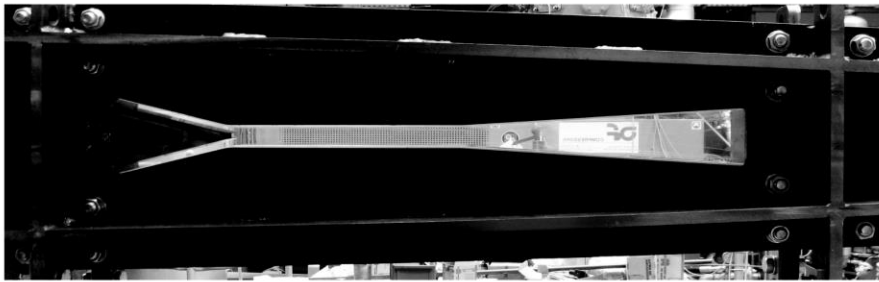
with a circular cross-section. This ejector cross section affords more accurate visualization and quantification without the effects of optical distortion that would typically be seen with circular cross sections. With the ejector designed in this manner, this study provides the first detailed examination and evaluation of flow features inside an operating ejector.

### **3.2 Experimental Approach**

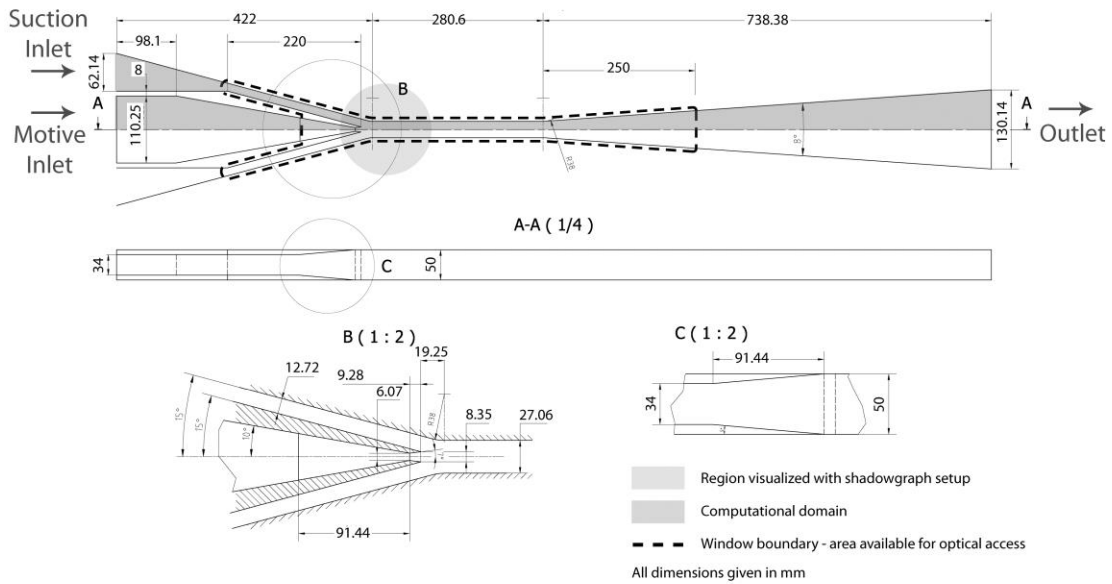
Visualization images as well as global ejector operation conditions were obtained on a large-scale ejector test facility. A photograph and schematic of the visualization test section are provided in Fig. 3.1, showing the specific dimensions of the ejector, the optically-accessible area for visualization, location of the visualization images, and the domain considered for CFD simulations. This ejector has a rectangular cross-section to avoid visual distortion effects, and the side walls are made of Plexiglas for optical access. The motive flow enters through a converging-diverging nozzle with a throat height and depth of 6.1 and 50.0 mm respectively, and a mixing section height and depth of 27.1 and 50.0 mm, respectively. The nozzle exit position, or distance between the motive nozzle tip and the start of the constant-area mixing section, is 19.3 mm.

The air flow is supplied to the motive nozzle inlet by an industrial Ateliers François compressor (Model CE46B with a capacity of 1320 m<sup>3</sup> hr<sup>-1</sup> FAD and power of 250 kW) and regulated by a Bellofram T-2000 pneumatic valve based on controller input. The maximum motive inlet pressure is limited to 6 bars, at which the maximum motive air mass flow rate is 0.35 kg s<sup>-1</sup>. The suction flow is taken from the ambient for all test conditions, and based on the geometry of this specific ejector, the suction air mass flow rate can reach up to 0.18 kg s<sup>-1</sup>. The outlet of the ejector also leads to the ambient, and a butterfly valve





(a)



(b)

**Figure 3.1: (a) Photograph of the visualization section, and (b) dimensioned drawing of same section showing exact 3D geometry of motive nozzle, suction nozzle, mixing section, and diffuser. Dotted line in (b) indicates the area available for visualization. Shaded areas indicate the computational domain and region visualized in shadowgraph images.**

regulates the exit pressure of the visualization section between ambient pressure and the desired set point.

Figure 3.2 shows a schematic of the entire ejector test setup, providing the locations of pressure and temperature measurements, as well as the locations of the air compressor inlet, suction inlet, outlet valve, visualization section, and shadowgraph visualization equipment. Temperature measurements were taken using PT100 RTD temperature probes (uncertainty  $\pm 0.5^\circ\text{C}$ ), while pressure measurements were taken using Endress Hauser and Kistler pressure transducers (uncertainty  $<\pm 300$  Pa). The temperature and pressure measurements provide boundary conditions for comparison with CFD results, and also provide the necessary data to calculate mass flow rates for each inlet and outlet flow using orifice plates with ISO standard 5167 (uncertainty  $<\pm 0.8\%$  reading). The MER and SPR are calculated as follows:

$$MER = \frac{\dot{m}_{suction}}{\dot{m}_{motive}} = \frac{M2}{M1} \quad (3.1)$$

$$SPR = \frac{P_{outlet}}{P_{suction\ inlet}} = \frac{P301}{P202} \quad (3.2)$$

Note that the pressures used to calculate SPR are static pressures, and the pressure used for the suction inlet is the one that is closer to the visualization section inlet for the most accurate comparison of CFD, analytical, and experimental results.

For all visualization data, a simple shadowgraph system was used to detect the density changes within the ejector flow. A bird's-eye view schematic of this setup (inset of Fig. 3.2) shows the four main components of the system. The first is the light source, nominally a point light source, produced by a positional fiber-optic lamp and attenuated by a pinhole slit. The second is a 150 mm diameter spherical mirror with a 300 mm focal

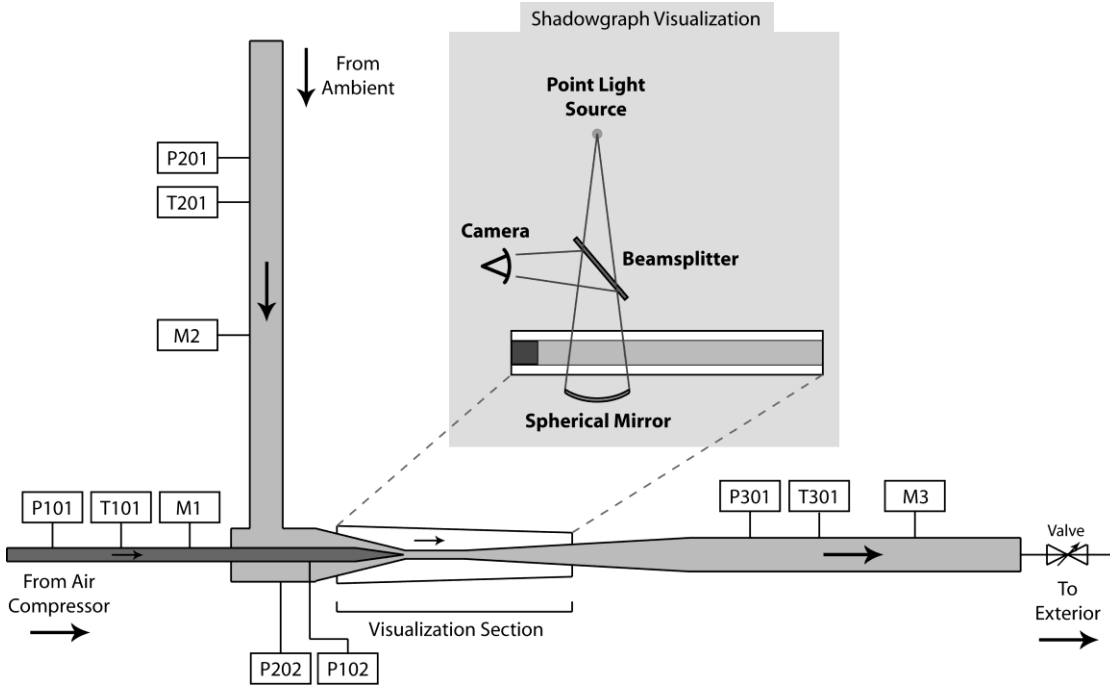


**Figure 3.2: Schematic of overall system indicating locations of pressure and temperature measurements, and orifice plates for flow rate measurement. Inset shows schematic of shadowgraph visualization setup.**

length, placed behind the test section and responsible for reflecting the light back through the test section and focusing it for capture with the camera. The third item is a Nikon D5000 digital SLR camera, while the fourth is a beam splitter. The beam splitter reflects 50% and transmits 50% of the incident light, resulting in 25% of total light supplied by the light source reaching the camera after passing through the beam splitter twice. The beam splitter reduces distortion effects such as double-imaging and skewing from asymmetric light beam paths. The images presented in this work show the small region near the outlet of the motive nozzle, as indicated in Fig. 3.1, where flow features were strong enough to be visible with this technique. A grid target was used to check for correct alignment of the system and trueness of the captured images. Upon close observation, there was very slight distortion of the image at the outer edges of the visualization area because the light rays passing

through the test section were not perfectly parallel. At the center of the visualization area, where the flow feature images were taken, these effects were not noticeable and are considered negligible for the purposes of this study.

To compare visual and experimental results, it was necessary to post-process the CFD results to show exactly the same phenomena as indicated by the shadowgraph imaging method. In shadowgraphy, refracted light casts shadows or bright spots as the different light rays diverge or converge, respectively. Unlike a Schlieren image that shows the gradient of refractive index, a shadowgraph shows the change in this refractive index gradient, or in other words, the Laplacian of the refractive index. For air, there is a linear relationship between refractive index and density (Settles, 2001). Therefore, light and dark regions of a shadowgraph are proportional to the Laplacian of density, and contours of this value from CFD results are used for comparison with the shadowgraph images from experiments. Therefore, an expansion appears as a thin light region followed by a thin dark region, and vice versa for a compression or shock (Saad, 1993).

### **3.3 Computational Modeling**

Two cases are chosen for comparison with visual data. One case is for on-design operation, defined as a condition where both motive and suction flows are choked inside the ejector. At this condition, a change in downstream or outlet conditions does not change the MER of the ejector. The specific on-design point chosen for comparison is based on a nominal motive pressure of 3.5 bar, suction pressure of 1 bar, and outlet pressure of 1.2 bar. Similarly, one off-design condition, where the motive flow has choked but the secondary has not, is used for comparison with experimental results for a nominal motive pressure of 3.5 bar, suction pressure of 1 bar, and outlet pressure of 1.5 bar. The exact temperature and

**Table 3.1: Description and position of each measurement taken on ejector test facility with corresponding exact value measured under experimental conditions. These values are the boundary conditions used for all presented CFD models.**

Description	Position (Fig. 3.2)	Nominal Motive Pressure	
		$P_{\text{outlet}} = 1.2 \text{ bar}$ (On-design)	$P_{\text{outlet}} = 1.5 \text{ bar}$ (Off-design)
$P_{\text{motive inlet}}$ [bar]	P102	3.50	3.49
$T_{\text{motive inlet}}$ [°C]	T101	10.5	10.4
$P_{\text{suction inlet}}$ [bar]	P202	0.95	0.99
$T_{\text{suction inlet}}$ [°C]	T201	17.2	17.3
$P_{\text{outlet}}$ [bar]	P301	1.20	1.50
$T_{\text{outlet}}$ [°C]	T301	13.2	12.5

pressure conditions that correspond to the actual experimental conditions are provided in Table 3.1, and the corresponding MER is plotted in Fig. 3.3 vs. outlet static pressure to show the position of each point in the on- or off-design region. Note that the additional experimental data points shown in Fig. 3.3 are necessary to obtain the characteristic curve for the ejector at a nominal motive pressure of 3.5 bar, but are not used in the following comparative analysis.

The values in Table 3.1 were used as the boundary conditions for the CFD simulations. It should be noted that these pressures are static pressure measurements, whereas the inlet boundary condition input for ANSYS FLUENT is total pressure. Considering that the inlet and outlet velocities of the visualization section were relatively low (by design) at the boundary condition locations indicated in Fig. 3.1, the difference between static and total pressure is considered negligible. Furthermore, the physical location of the experimental pressure measurements in Fig. 3.2 is different from what is identified as the beginning of the computational domain in Fig 3.1. Accounting for pressure drop from frictional losses, as well as the change in pressure from slight changes in cross-sectional area, it is found that the maximum difference in pressure between any one

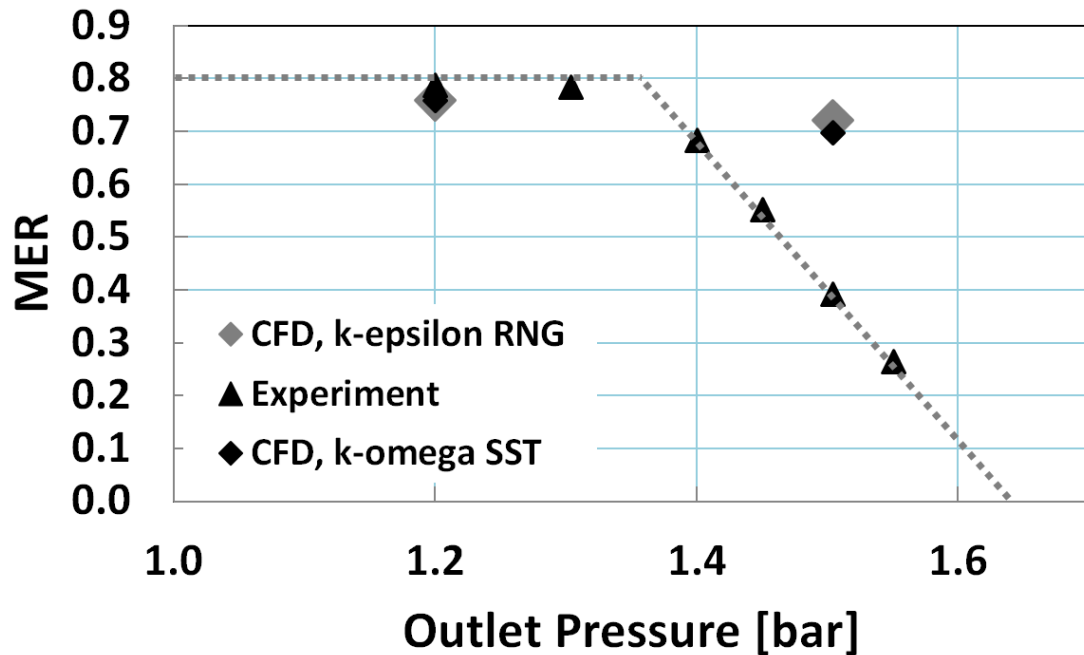


**Figure 3.3: Experimental characteristic curve of ejector operation for  $P_{\text{motive}} = 3.5$  bar and  $P_{\text{suction}} = 1$  bar shown by dotted line. Diamond-shaped data points indicate MER values for CFD simulations for the one on-design and one off-design condition considered for comparison in this study.**

boundary and its respective pressure measurement is less than 0.0013 bar. A sensitivity analysis showed that such changes in the pressure at the boundary conditions result in a change of  $\leq 1\%$  of the suction flow rate value. Therefore, these effects are also considered negligible.

Numerical simulations were conducted using the commercial CFD package ANSYS FLUENT v13 (2010), which is based on a finite volume approach. For each condition, two 2D CFD simulations were conducted using turbulence models  $k-\omega$  SST and  $k-\epsilon$  RNG. A rectangular mesh is adapted for areas of high Mach number and static pressure gradients, and refined at walls to attain  $y^+ < 1$  to ensure correct modeling of near-wall flow (wall-resolved RANS). The coupled set of equations (mass, momentum, energy) as well as the state equation is solved with a point implicit solver (block Gauss-Seidel) in conjunction

with an algebraic multigrid method. The solution is advanced using a time marching technique, and the time derivative terms are preconditioned to overcome numerical stiffness encountered at low Mach number or quasi-incompressible flow conditions. Inviscid fluxes are discretized by second order flux-difference splitting (based on Roe's approach), while the diffusion term is evaluated by a classical central difference. Convergence is defined by a change in all normalized residuals of less than 1E-6 for 1000 iterations, and a minimization of overall mass and energy imbalances over the computational domain. Grid dependence is checked for both turbulence models for the case of 3.5 bar motive pressure and 1.45 bar outlet pressure. With an ~18% increase in the number of cells, the corresponding change in inlet and outlet mass flow rates is less than 1%. Furthermore, Figs. 3.4 and 3.5 present a comparison of the centerline static pressure

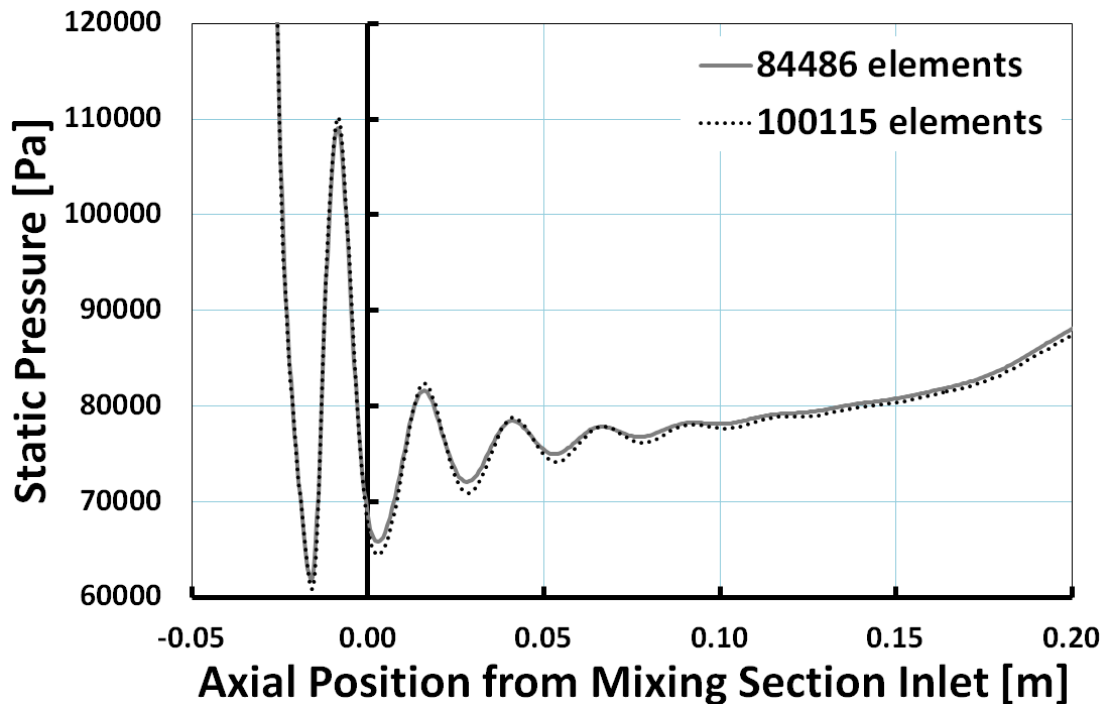


**Figure 3.4: Centerline static pressure vs. axial position for  $k-\epsilon$  turbulence model. An ~18% increase in the number of elements shows negligible change in the solutions.**

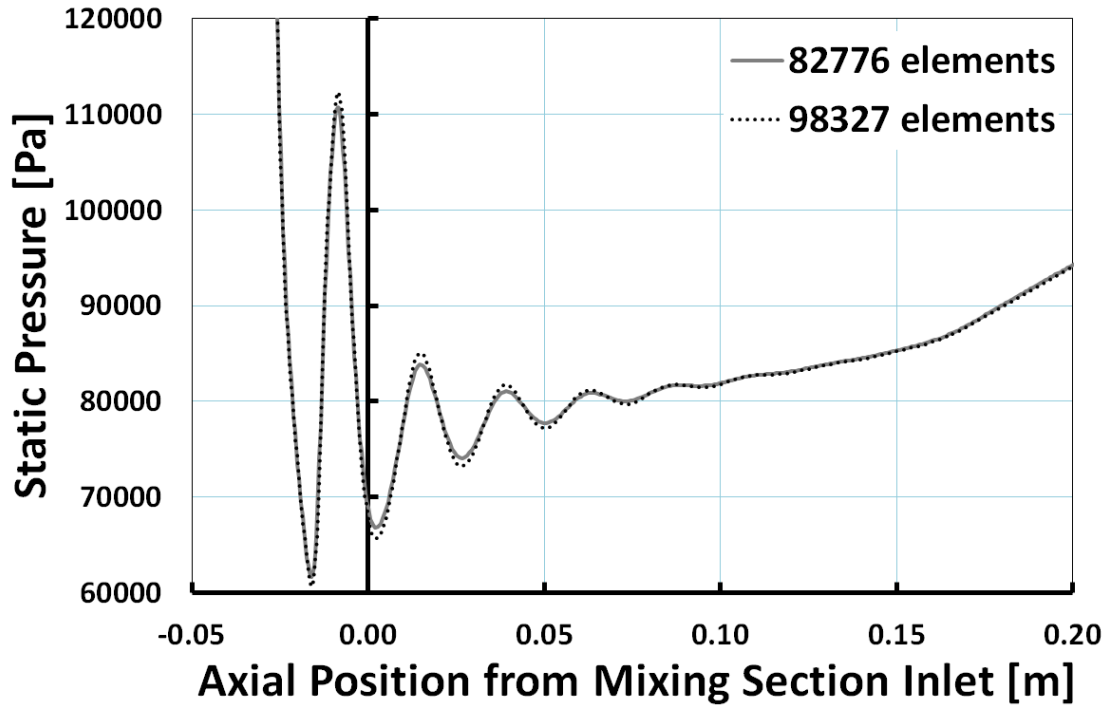


**Figure 3.5: Centerline static pressure vs. axial position for  $k-\omega$  turbulence model. An ~18% increase in the number of elements shows negligible change in the solutions.**

for the coarse and fine grid sizes, respectively, showing that there is little difference between the two in terms of magnitude and location of flow features, confirming that a grid size of > 85k cells is sufficient for this simulation. Therefore, the final grid sizes for the 1.2 and 1.5 bar back pressure  $k-\epsilon$  RNG models were chosen to be 110247 and 107565, respectively, and 145158 and 102639 for the  $k-\omega$  SST models, respectively.

### 3.4 Analytical modeling

An analytical first-principles model complementing the computational model detailed in Section 3.3 is also developed to both assess the departure of actual flow from ideal conditions, and to provide another method through which the ejector flow field can be resolved. The analytical modeling technique is demonstrated for the case of nominal motive, suction, and outlet pressures of 3.5, 1.0, and 1.5 bar, respectively. This off-design



case is chosen because non-ideal effects are more pronounced in the flow, and are more easily detected by the model.

This model divides the ejector flow field into discrete regions that are defined by the physical location and orientation of flow features. The change in flow properties across each flow feature can be calculated by modifying the fundamental relations derived for adiabatic ideal gas flow with constant specific heats ( $\gamma = 1.4$ ), to account for the non-ideal flow effects. As a result, the flow field can be entirely resolved knowing only the motive inlet  $T$  and  $P$ , motive nozzle geometry, and three angles taken from a visual image:  $\theta_3$ ,  $\theta_4$  and  $\mu_{6i}-\alpha_6$ .

The top part of Fig. 3.6 shows an image of the Laplacian of density generated by the off-design CFD simulation described in the previous section using the  $k-\varepsilon$  RNG turbulence model, with labels showing the position of each region that is used for the analysis. The bottom graph shows static pressure profiles for the flow at the centerline and at the jet boundary, scaled to match the axial distance in the CFD image. A schematic of the flow features seen is given in the middle of Fig. 3.6, indicating important geometric parameters. Region 3 starts at the exit plane of the motive nozzle and extends to the first shock coming from the motive nozzle tip at an angle of  $\theta_3$  with respect to the horizontal. After this shock, the flow compresses to Region 4. Region 4 compresses once again across the reflected shock at an angle of  $\theta_4$  to the horizontal to form Region 5. At this point, the shock reflects off the jet boundary to produce a Prandtl-Meyer expansion fan. The expansion completes to form Region 6, where the flow is at an angle  $\alpha_6$  with respect to the horizontal. The last Mach wave of the first expansion fan is at an angle  $\mu_{6i}-\alpha_6$  with respect

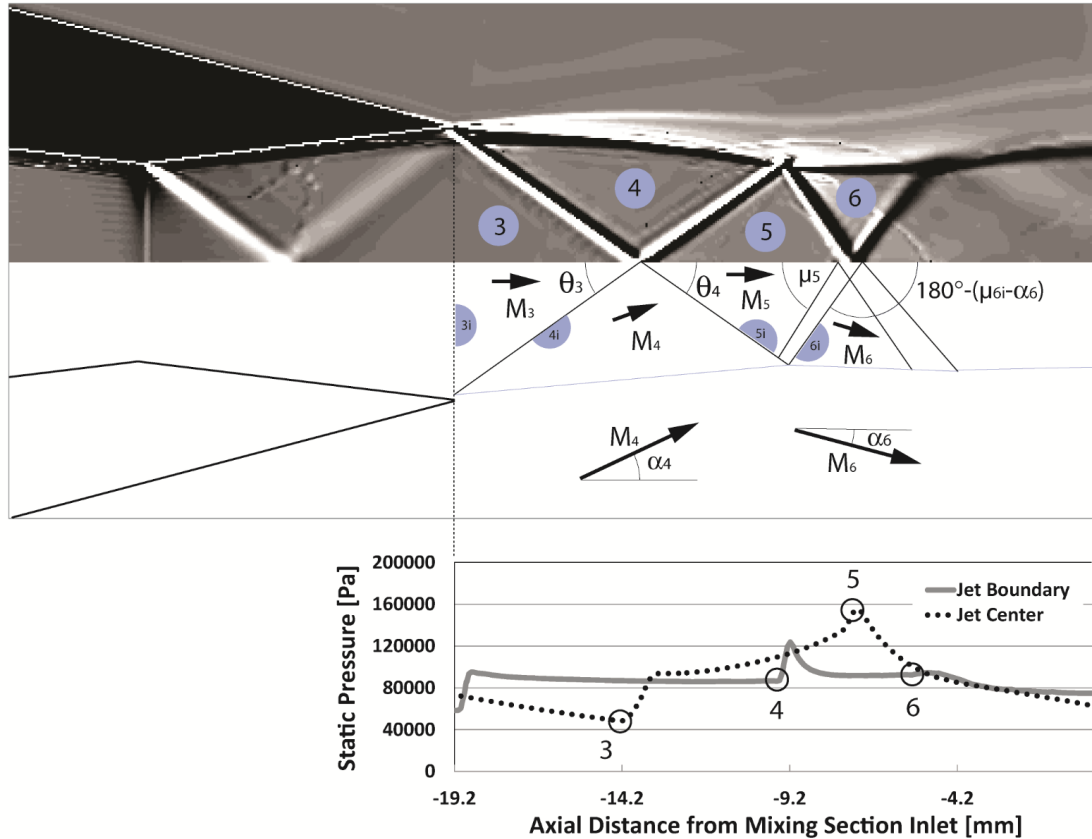


**Figure 3.6: (Top) Image from off-design CFD simulation ( $P_{\text{motive}} = 3.5$  bar,  $P_{\text{suction}} = 1$  bar, and  $P_{\text{outlet}} = 1.5$  bar) using  $k-\varepsilon$  RNG turbulence model indicating Region locations. (Middle) Schematic used for analytical model, identifying important geometric values. (Bottom) Graph shows contours of static pressure along the motive jet center and jet boundary, indicating specific points where data were taken for States 3 through 6 in Table 3.2.**

to the horizontal. States 3i through 6i shown in Fig. 3.6 are idealized states that exist immediately after a given flow feature, and are used in the following analysis.

The analytical model starts at the entrance to the motive nozzle where  $P_m = 3.5$  bar and  $T_m = 290.1$  K and the density is found using the ideal gas equation of state. Because the motive nozzle is a converging-diverging nozzle, it is known that  $M = 1$  at the motive nozzle throat according to isentropic theory, and based on the cross-sectional area of the throat,  $A_c^*$ , the mass flow rate of air through the nozzle is  $0.252 \text{ kg s}^{-1}$ . From mass

**Table 3.2: Flow conditions taken from CFD flow field and used to define correction coefficients. Locations at which properties are taken are indicated in the bottom graph of Fig. 3.6.**

Region	$T$ [K]	$P$ [Pa]	$M$ [-]
3	161.2	48410	1.95
4	206.8	86514	1.40
5	225.1	155030	1.14
6	218.5	91667	1.38

conservation, the velocity of flow at the entrance of the motive nozzle is found to be  $16.0 \text{ m s}^{-1}$ , and the total pressure and temperature are found accounting for the dynamic contributions to each. The static temperature and pressure at all points along the nozzle are found using basic relations for adiabatic 1D isentropic flow (John, 1984). For the sample case, the properties at the exit plane of the motive nozzle are found to be  $P_{3i} = 66930 \text{ Pa}$  and  $T_{3i} = 180.8 \text{ K}$ . Note that this is an idealized state that neglects several flow phenomena including boundary layer effects and heat transfer with the nozzle wall. A further complexity arises in what happens to the flow between the motive nozzle exit and the first shock. Based on the pressure profile given in the bottom of Fig. 3.6, the flow continues to expand until  $x = -14.2 \text{ mm}$  where the first shock reflects off the centerline.

The complexities of these phenomena make precise modeling difficult. Therefore, a set of correction coefficients are introduced to bring the ideal state 3i to the actual state 3.

$$\Psi_p = \frac{P_3}{P_{3i}} \quad (3.3)$$

$$\Psi_T = \frac{T_3}{T_{3i}} \quad (3.4)$$

$$\Psi_M = \frac{M_3}{M_{3i}} \quad (3.5)$$

where each correction factor quantifies the ratio of a “real” flow condition to an ideal flow condition.

In order to properly tune the ideal model with these correction coefficients, the “real” flow conditions at state 3 should be defined. Because the actual flow field is not known, the CFD flow field is used instead to best define these real conditions with the data available. Using the same motive inlet  $T$  and  $P$  values, as well as measured angles  $\theta_3$ ,  $\theta_4$  and  $\mu_{6i}-\alpha_6$  from the CFD image in Fig. 3.6, the correction coefficients can be tuned to have an exact match with the “real”  $T$ ,  $P$ , and  $M$  in Regions 3, 4, 5, and 6 of the flow.

In the real flow field, the values of  $T$ ,  $P$ , and  $M$  vary continuously within each region, making it difficult to pinpoint what the state points should be. For this analysis, the value of each property is taken at the end of the region, as indicated at the bottom of Fig. 3.6 where the state point values for  $P$  are circled for Regions 3 through 6. These locations are chosen such that full expansion or compression can occur after the given flow feature, and to incorporate any non-idealities that may arise from heat transfer, mass exchange, or viscous interactions with the suction flow along the length of the region. These same indicated values of  $P$  as well as the matching  $T$  and  $M$  values are tabulated in Table 3.2. These are the values that are matched by tuning the correction coefficients mentioned above.

The values of  $T$ ,  $P$  and  $M$  are known at State 3 from Table 3.2. The total temperature and pressure can be calculated using the flow velocity, the density is calculated using the ideal gas equation of state, and velocity using  $V = M\sqrt{\gamma RT}$ .

When the flow transitions from State 3 to State 4i, it passes through the first shock. To find the change in properties across this oblique shock, the flow at  $M_3$  is resolved into normal and tangential components with respect to the first shock. It is assumed that the flow direction in Region 3 is  $\alpha_3=0^\circ$  with respect to the horizontal.

$$M_{3n} = M_3 \sin(\theta_3) \quad (3.6)$$

$$M_{3t} = M_3 \cos(\theta_3) \quad (3.7)$$

The value of  $\theta_3$  is measured to be  $35.5^\circ$  from the CFD image shown in the top of Fig. 3.6 using image processing software. With the value of  $M_{3n}$ , the change in properties across the shock is found using basic equations of motion for a normal shock wave, derived from conservation of mass, momentum, and energy equations.

$$M_{4ni}^2 = \frac{M_{3n}^2 + \frac{2}{\gamma-1}}{\frac{2\gamma}{\gamma-1}M_{3n}^2 - 1} \quad (3.8)$$

$$\frac{T_{4i}}{T_3} = \frac{\left(1 + \frac{\gamma-1}{2}M_{3n}^2\right)\left(\frac{2\gamma}{\gamma-1}M_{3n}^2 - 1\right)}{M_{3n}^2\left(\frac{2\gamma}{\gamma-1} + \frac{\gamma-1}{2}\right)} \quad (3.9)$$

$$\frac{P_{4i}}{P_3} = \frac{2\gamma M_{3n}^2}{\gamma+1} - \frac{\gamma-1}{\gamma+1} \quad (3.10)$$

Using equations 3 through 5, the correction coefficients for  $T$ ,  $P$ , and  $M$  at State 4 can be calculated using the real flow conditions tabulated in Table 3.2. Then using  $M_{4ni}$ ,  $M_4^2 = M_{4t}^2 + M_{4n}^2$  where  $M_{4n} = \Psi_{M4} M_{4ni}$ ,  $M_{3t} = M_{4ti}$ , and  $M_{4t} = \Psi_{M4} M_{4ti}$ . The flow direction at State 4,  $\alpha_4$ , is found from

$$\frac{M_{4n}}{M_4} = \sin(\theta_3 - \alpha_4) \quad (3.11)$$

and the total  $T$  and  $P$ , density, and flow velocity are found as they were for State 3.

Moving to State 5, the flow passes through the second, reflected shock, which can be modeled in the same way as the first shock. Once again, the normal component of  $M_4$  must be found, but this time with respect to the second shock. The angle of the second shock,  $\theta_4$ , is measured from the CFD image to be  $35.0^\circ$ . Using the normal component of  $M_4$  with respect to the second shock, Equations 3.8 through 3.10 yield the ideal state 5i. Then correction coefficients are found using Equations 3.3 through 3.5 with data in Table 3.2 to get to State 5. The flow angle in Region 5,  $\alpha_5$ , is assumed to be  $0^\circ$  because there can be no net flow across the centerline.

The transition from State 5 to 6 must be handled differently because the flow passes through a Prandtl-Meyer expansion fan rather than a shock. Flow from State 5 to 6i is assumed to be isentropic and adiabatic, such that  $P_{tot,6i} = P_{tot,5}$  and  $T_{tot,6i} = T_{tot,5}$ . The first Mach wave forms at an angle  $\mu_5 = \sin^{-1}(1/M_5)$  with respect to the flow direction  $\alpha_5$ . Similarly,  $\mu_{6i} = \sin^{-1}(1/M_{6i})$ . (Note that  $M_{6i}$  is used here because the flow immediately after

the expansion fan has not yet had time to be influenced by any non-ideal effects, or in other words, the mixing and heat transfer lengths in the expansion fan itself are too small to have an effect.) Unfortunately,  $\mu_{6i}$  itself cannot be measured easily from the CFD image. Instead, the angle  $\mu_{6i}-\alpha_6$  is easier to discern, as notated in Fig. 3.6. To find  $\alpha_6$ , the total turning angle of the expansion fan (John, 1984) can be defined as  $\alpha_6-\alpha_5=v_{6i}-v_5$  where

$$v = \left( \sqrt{\frac{\gamma+1}{\gamma-1}} \tan^{-1} \sqrt{\frac{\gamma-1}{\gamma+1}} (M^2 - 1) - \tan^{-1} \sqrt{M^2 - 1} \right) \quad (3.12)$$

As such,  $\mu_{6i}-\alpha_6$  is measured to be  $59.5^\circ$ . Once  $M_{6i}$  is known,  $T_{6i}$  and  $P_{6i}$  can be found using basic 1D isentropic flow relations. Then to bring State 6i to 6, correction coefficients are fitted to State 6 data in Table 3.2.

After Region 6, the analysis is discontinued because it is no longer possible to discern the location of flow features from the CFD image with reasonable accuracy as viscous effects become more important and isentropic flow relations are no longer valid. In summary, the flow field through Region 6 is resolved using only three geometric inputs,  $\theta_3$ ,  $\theta_4$ , and  $\mu_{6i}-\alpha_6$ , and motive inlet conditions and geometry. Then, to tune the model to account for non-ideal effects,  $T$ ,  $P$ , and  $M$  for each region are needed to define  $\Psi_T$ ,  $\Psi_P$ , and  $\Psi_M$ , respectively. It should be mentioned that the success of this method depends heavily on the ability to accurately measure angles  $\theta_3$ ,  $\theta_4$ , and  $\mu_{6i}-\alpha_6$ . Accounting for a measured angle uncertainty of  $\pm 1^\circ$  on  $\theta_3$ ,  $\theta_4$ , and  $\mu_{6i}-\alpha_6$  (which is well within the measuring limit of the image processing software used), the most affected correction coefficient is  $\Psi_{P4}$  with an error of  $\pm 5.5\%$ . Of course, there is also an uncertainty associated with the difference between the CFD flow field and the real flow field, but this is extremely difficult to quantify

with the present test set up or others in the literature where high-fidelity  $T$  and  $P$  measurements are unavailable for local flow conditions. Furthermore, the correction coefficients found are specific to the off-design flow condition chosen, but it is expected that they will be similar for any ejector flow with an overexpanded motive jet, especially at off-design conditions.

It is important to emphasize that the utility of this method is not necessarily in the ability to predict the real flow field accurately, but rather to identify locations where there are significant non-ideal effects taking place (i.e., mixing, heat transfer, momentum transfer), and use this information to modify existing turbulence models and make suggestions for ejector geometric design. This identification can be done by considering the calculated correction coefficients themselves, as is demonstrated in Section 3.5.2.2.

### 3.5 Results and Discussion

#### 3.5.1 Comparison of Global Flow Features

The most practical and readily available, although perhaps not the most detailed, assessment of turbulence model performance is through global ejector parameters. Table 3.3 provides a comparison of CFD and experimental values for motive and suction mass flow rates at conditions shown in Table 3.1. The difference between CFD and experimental results for motive flow rate values for all cases is about 8%; this error appears to be

**Table 3.3: Comparison of CFD and experimental values for global parameters of motive and suction mass flow rates.**

Nominal $P_{\text{motive}}$ [bar]	Nominal $P_{\text{outlet}}$ [bar]	Mass flow rate [kg s <sup>-1</sup> ]					Difference [% of exp. value]	
		Experiment		CFD			Motive	Suction
		Motive	Suction	Turb. Model	Motive	Suction		
3.5	1.2	0.234	0.184	$k-\epsilon$ RNG	0.252	0.191	7.7	4.0
				$k-\omega$ SST	0.252	0.191	7.8	3.9
	1.5	0.234	0.092	$k-\epsilon$ RNG	0.252	0.181	7.7	97.6
				$k-\omega$ SST	0.252	0.176	7.9	91.5



systematic for all data points. The basic 1D model of isentropic flow through a converging-diverging nozzle with the same geometry as the motive nozzle indicated in Fig. 3.1 yields a motive flow rate of 0.252 kg/s, which is the same as the CFD value. This suggests that there is a small discrepancy, in part due to fabrication tolerances, between the dimensions in Fig. 3.1 and the actual experimental geometry. For example, a small change in motive nozzle throat height from 6.07 to 5.51 mm could cause the difference seen in the flow rate. It is also possible that this discrepancy arises from losses in the real system, such as flow separation induced by an angular converging-diverging motive nozzle profile. As for the suction flow rate, Table 3.3 shows that for *on-design* operation, both turbulence models provide very good predictions to within 4%, with the  $k-\omega$  SST model performing slightly better. For the *off-design* condition as well, the  $k-\omega$  SST model performs better; however, in this case, the error for both models is so large ( $> 91\%$ ) that such differentiation between the turbulence models is no longer meaningful.

For both on- and off-design flow rates, the values of the predicted flow rates are higher than the measured values. For the primary flow rate, this overprediction is due to the differences in geometry or the unaccounted losses mentioned above. For the suction flow rate, the overprediction can occur because the turbulence models tend to predict both better mixing (i.e., better momentum transfer from the motive to suction flow) between flows and weaker shocks (implying that more energy is transferred to the suction flow rather than lost to irreversibilities) than those that occur in the real system because of over-diffusive behavior. The fact that the two turbulence models predict similar deviation from the experimental data suggests that there is a reduced sensitivity to the exact turbulence model used, and instead the deviation may be caused by another factor, as discussed below.

The presence of 3D effects in the rectangular ejector geometry under investigation, especially at off-design operation, could also contribute to the deviation. In a rectangular ejector, the motive jet is influenced not only by momentum contact with the suction flow on two faces, but also by a no-slip boundary condition on the other two faces. This may result in significant loss of momentum to the ejector walls that would normally be transferred to the suction flow in an axisymmetric system, thus decreasing the measured suction flow rate, through a mechanism that is not modeled in a 2D CFD model. Other work by the author (Mazzelli *et al.*, 2015) show ~14% error in prediction of MER with respect to experimental results when using 3D CFD models. This is in comparison to ~42% error when using 2D CFD models.

Therefore, both turbulence models appear to be accurate for predicting on-design conditions, but there is significant discrepancy for off-design conditions that is due either to an inability of the turbulence models to accurately predict local flow features responsible for entrainment, or more likely the increased 3D wall effects at off-design conditions. To better assess the accuracy of the turbulence models, a closer inspection of local flow features is necessary.

### **3.5.2 Comparison of Local Flow Features**

#### ***3.5.2.1 Comparison of Turbulence Models***

To assess the turbulence models at the local scale, specific attention was paid to the position of flow features, and the number and strength of shock cells inside the motive jet. These can both be indications of the diffusive behavior predicted by each turbulence model, where more diffusive behavior is characterized by fewer shock cells and weaker shocks. The first comparison is presented in Fig. 3.7 for nominal conditions of  $P_{\text{motive}} = 3.5$  bar,

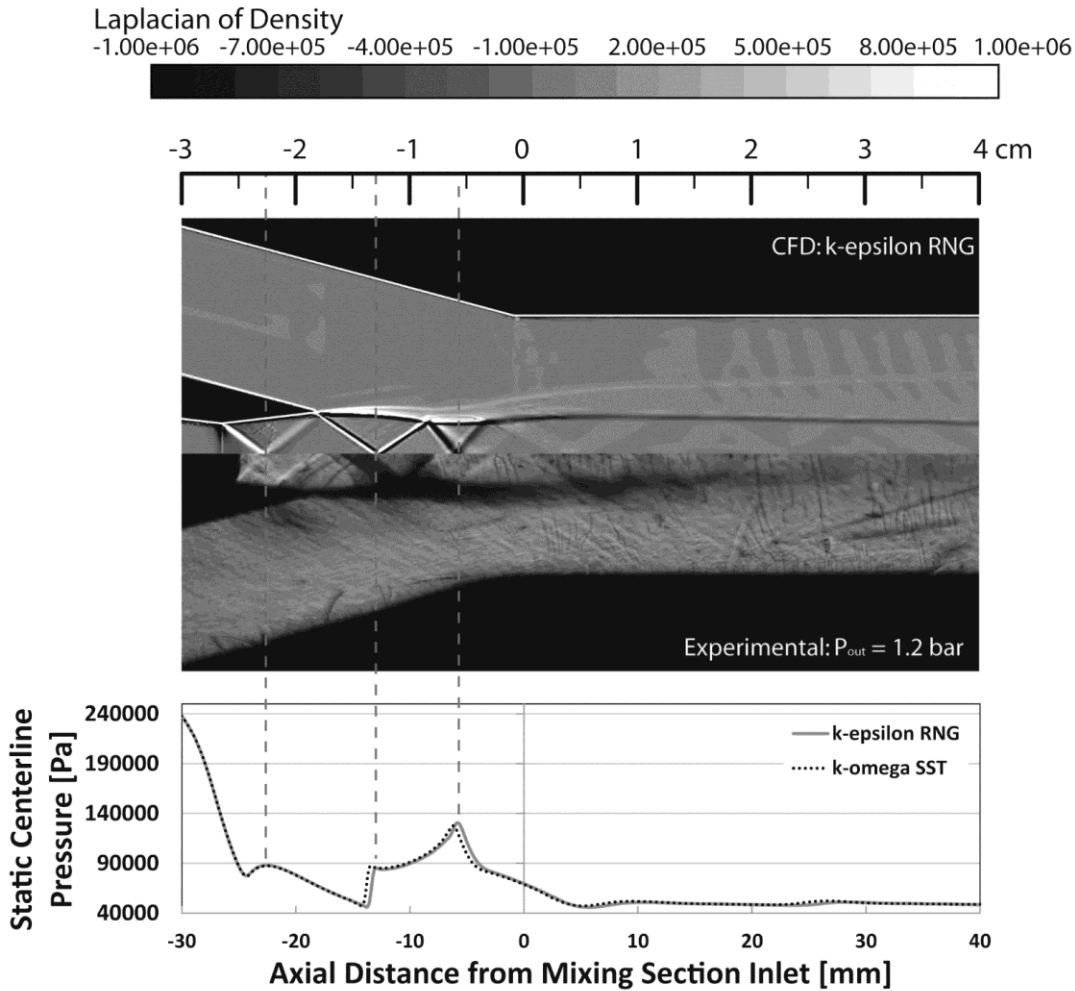


**Figure 3.7: Experimental image and CFD data for on-design condition with  $P_{\text{motive}} = 3.5$  bar,  $P_{\text{suction}} = 1$  bar, and  $P_{\text{outlet}} = 1.2$  bar. Visual comparison using contours produced by  $k-\epsilon$  RNG turbulence model. Bottom graph shows static pressure along ejector central axis, comparing values for  $k-\epsilon$  RNG to  $k-\omega$  SST data. Three major flow features are indicated at  $x = -22.6$  mm (expansion),  $x = -13.0$  mm (compression), and  $x = -5.8$  mm (expansion).**

$P_{\text{suction}} = 1$  bar, and  $P_{\text{outlet}} = 1.2$  bar in the on-design region, where both the motive and suction flows are choked (see data point in Fig. 3.3). The top half of the image shows contours of the Laplacian of density realized with the boundary conditions listed in Table 3.1 and using the  $k-\epsilon$  RNG turbulence model. The lower half shows the experimental shadowgraph image of the flow at the same conditions. The vertical dashed lines indicate

the position of major flow features in the CFD model, while the corresponding static pressure profile along the central axis is shown in the solid grey profile in the bottom graph. The dotted profile provides a comparison for the same conditions using the  $k-\omega$  SST turbulence model. The first major flow feature indicated is the point at which the first expansion, attached to the motive nozzle throat, reflects off the central axis of flow at position  $x = -22.6$  mm. From the pressure profile, it can be seen that across this expansion, there is a transition from high to low static pressure, and the expansion appears as a light-to-dark region, as expected for an expansion wave (Saad, 1993). The second major flow feature is at  $x = -13.0$  mm. This feature is important because it indicates whether the motive jet is over or underexpanded. From the pressure profile, there is a sudden rise in pressure, and the density Laplacian shows a very small dark region followed by a more obvious light region, indicating a shock. Furthermore, centerline pressure should change from low to high across a reflected shock (Saad, 1993). Therefore, the second flow feature at  $x = -13.0$  mm is a shock, implying that the motive jet is slightly overexpanded. Reflection of this shock at the constant-pressure jet boundary produces an expansion fan that appears at  $x = -5.8$  mm on the centerline. By the time the motive jet has entered the mixing section at  $x = 0$  mm, the oscillations in centerline pressure have mostly subsided, and the pressure is almost constant with no visible flow features.

When comparing the static pressure profiles of the two turbulence models, it can be seen that the flow features are generally translated slightly to the left, or further upstream, with the  $k-\omega$  SST simulation (except for the first flow feature where turbulence plays a minor role in the jet core). In the motive nozzle, there are fewer viscous effects because there is no secondary flow present, and the position of the first expansion after the

motive nozzle throat is affected to a lesser extent by the turbulence model used. But for the other two flow features, these viscous effects are more important, and different treatment of viscous effects results in a change in position. The viscous effects of each turbulence model can also be evaluated with strength of each shock or expansion, indicated by the  $\Delta P$  across it and the angle of the flow feature. The CFD data show that  $\Delta P$  across this first shock is 39219 and 39887 Pa for  $k$ - $\epsilon$  RNG and  $k$ - $\omega$  SST models, respectively. But these differences in  $\Delta P$  are so slight that no conclusion can be made as to which is more or less diffusive, especially in a region so close to the motive nozzle exit. More accurate local internal data in the far field region from the motive nozzle outlet are necessary to evaluate this characteristic.

For off-design conditions, the far field region is more accessible for observation because the flow features are more obvious. This is because momentum transfer between the motive and suction flows is felt along the entire length of the ejector because the limit (choking) of suction flow has not yet been reached, resulting in more intense shock/expansion interaction with the mixing layer.

Figure 3.8 shows the comparison for nominal conditions of  $P_{\text{motive}} = 3.5$  bar,  $P_{\text{suction}} = 1$  bar, and  $P_{\text{outlet}} = 1.5$  bar in the off-design region where only the motive flow is choked (see data point in Fig. 3.3). (The top CFD image is the exact same one shown in Fig. 3.6 for use with the analytical model.) Again, the major flow features indicated by the CFD data are an expansion at  $x = -22.6$  mm, a compression at  $x = -13.2$  mm, and another expansion at  $x = -7.1$  mm. In comparison to Fig. 3.7, it is seen that the flow features have moved slightly upstream because of the increase in outlet pressure from 1.2 to 1.5 bar. This shift upstream is reflected in the shadowgraph image, but the same mismatch between CFD

and experimental results is still evident. For this 1.5 bar back pressure case, flow features further downstream are easier to identify in both the CFD data and the shadowgraph, and the graph of centerline static pressure shows that this is because the pressure oscillations in the motive jet are stronger than those for a back pressure of 1.2 bar.

Comparing the two turbulence models in the lower graph of Fig. 3.8, trends similar to the data in Fig. 3.7 can be seen. With distance downstream of the motive nozzle exit, the discrepancy between the  $k$ - $\epsilon$  RNG and  $k$ - $\omega$  SST turbulence models becomes more obvious as the distance available for momentum transfer increases. For example, at position  $x = 13.2$  mm, the discrepancy in flow feature location is only 0.7 mm, whereas downstream at  $x = 36.5$  mm, the discrepancy is larger at 3.5 mm. Even though the largest velocity mismatch between the motive and suction flows occurs at the exit of the motive nozzle, the motive flow velocity in the first one or two shock cells is still so high that there has not been enough time for momentum transfer to occur. This means that differences between the two turbulence models can only be realized further downstream, and it is only for this off-design condition that these discrepancies are large enough to allow for an assessment of turbulence models. More generally, a visual comparison with the shadowgraph shows that there are more compressions and expansions visible in the experiments than in the results from the CFD model. This could be due to the prediction of a pressure equilibrium over a shorter distance, or more efficient mixing with the CFD model that results in weaker shocks/expansion cells and a shorter area containing such shock/expansion reflections. However, beyond the first shock/expansion cells, it seems that the outer jet boundary tends to collapse more rapidly towards the centerline in the experiment. This would involve, on

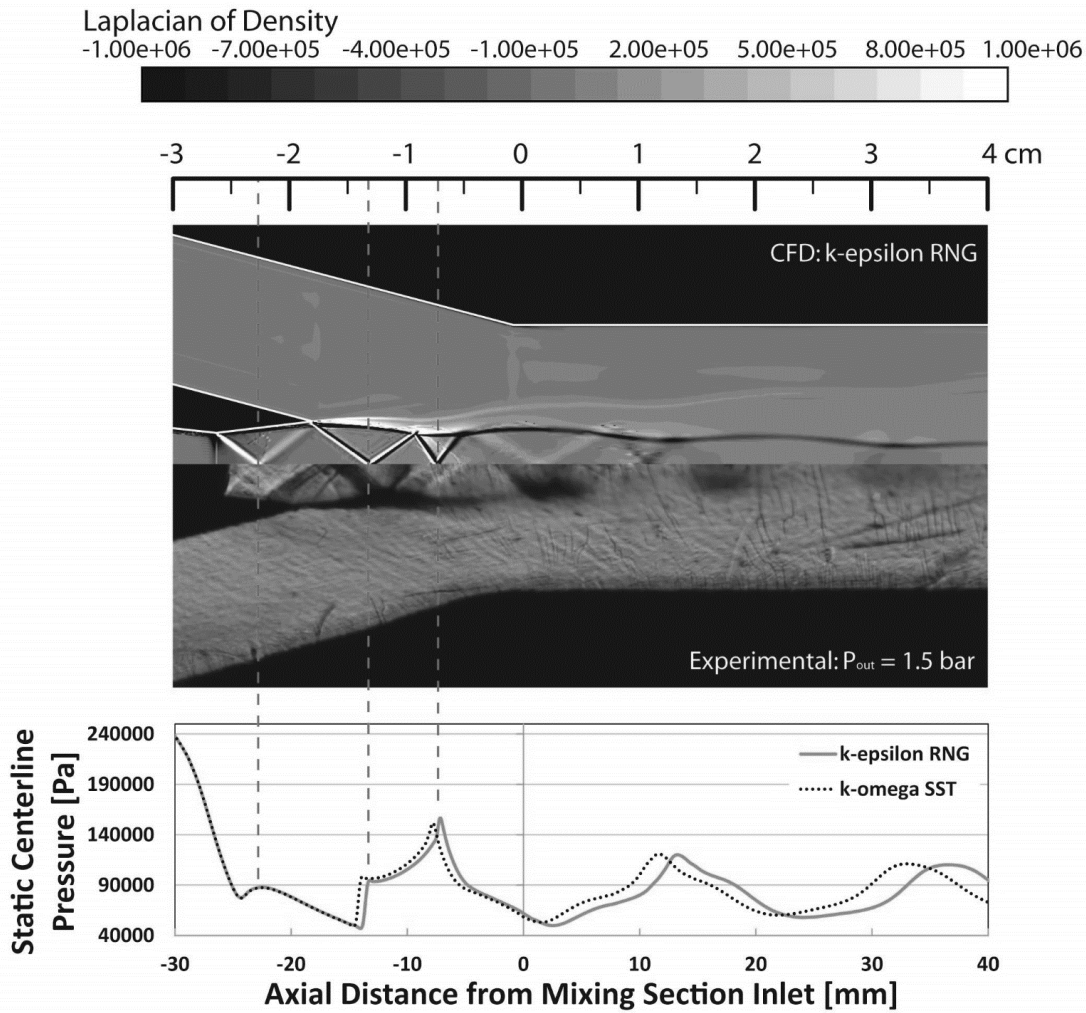


**Figure 3.8: Experimental image and CFD data for off-design condition with  $P_{motive} = 3.5$  bar,  $P_{suction} = 1$  bar, and  $P_{outlet} = 1.5$  bar. Visual comparison using contours produced by  $k-\epsilon$  RNG turbulence model. Bottom graph shows static pressure along ejector central axis, comparing values for  $k-\epsilon$  RNG to  $k-\omega$  SST data. Three major flow features are indicated at  $x = -22.6$  mm (expansion),  $x \approx -13.2$  mm (compression), and  $x \approx -7.1$  mm (expansion).**

the contrary, an underprediction of the mixing by the CFD model far from the motive nozzle exit.

### 3.5.2.2 Analytical Model vs. Visual Observations

Using the model developed in Section 3.4, the real flow field at off-design conditions can be resolved using the CFD image in Fig. 3.6. The final correction factors for the analytical model are given in Table 3.4. As mentioned previously, these correction factors are the adjustments required in each region to bring the idealized flow to the “real” flow conditions from the CFD simulation values presented in Table 3.2. The values given in parentheses indicate the sensitivity of each coefficient to a +5% or -5% change in  $T$ ,  $P$ , or  $M$ . For example, if the real pressure in Region 4 is 86514+5% Pa, correction coefficient  $\Psi_P$  will increase to 1.344-10%. If the real pressure is 86514-5% Pa,  $\Psi_P$  will be 1.344+12%. This gives an indication of a range for the values of these coefficients to match real flow conditions instead of a CFD approximation of real flow conditions. As expected, the correction coefficients are the most sensitive to a change in pressure, and all correction coefficients are expected to be in within  $\leq \pm 12\%$  of the value listed in Table 3.4.

The main purpose of these correction coefficients is to provide important insight into the non-idealities of the flow, including the effects of viscous dissipation, mixing, heat transfer, and other effects that result from interaction of the motive jet with the suction flow. While an individual correction factor is not able to quantify the non-ideality directly, it can provide guidance on the sources of any non-ideal effects.

**Table 3.4: Correction coefficients used to match idealized first-principles analysis to flow conditions identified in Table 3.2. Values in parentheses represent the change in coefficient caused by a  $\pm 5\%$  change in the flow property to which the coefficient corresponds.**

Region	$\Psi_T$	$\Psi_P$	$\Psi_M$
3	0.891 (+5%, -5%)	0.723 (+5%, -5%)	1.121 (+5%, -5%)
4	1.182 (-3%, +3%)	1.344 (-10%, +12%)	0.770 (+2%, -3%)
5	1.088 (-1%, +1%)	1.792 (-3%, +1%)	0.708 (-2%, +5%)
6	1.064 (+1%, -1%)	0.958 (+5%, -5%)	1.193 (+4%, -4%)



Starting in Region 3, the real flow conditions are nearly the same as the ideal flow conditions at 3i, but the physical location of 3 is further downstream. Due to 3D flow effects, expansion of the flow continues after the motive nozzle exit such that the velocity is higher, and the temperature and pressure are lower than in the ideal case ( $\Psi_M > 1$ ,  $\Psi_P < 1$ , and  $\Psi_T < 1$ ). Because it is not expected that there would be any mixing or heat transfer with the suction flow in this region, it seems that this 3D flow effect is the only deviation from ideal conditions.

Region 4 is the first region that comes into contact with the suction flow. At this location, the jet boundary converges and the supersonic motive flow consequently decelerates, most probably due to a transfer of kinetic energy to the suction flow. This behavior agrees with  $\Psi_M < 1$  and  $\Psi_P > 1$  because, as the flow decelerates, the pressure rises. Furthermore,  $\Psi_T > 1$  suggests that some heat is being added to the motive flow. This could be due either to viscous dissipation or more likely, due to dissipation of heat from the warmer suction flow to the cooler motive flow, which could cause further deceleration.

Region 5 is again isolated from the suction flow, and therefore any loss of momentum or heat gain from the suction flow is not expected.  $\Psi_M < 1$  and  $\Psi_P > 1$  indicate that after the second shock, the flow continues to gradually compress. This can be attributed again to the converging shape of the motive jet boundary. It would be expected that such deceleration, as well as viscous effects, would cause a rise in temperature, and this is demonstrated with  $\Psi_T > 1$ .

Finally, Region 6 is again in contact with the suction flow. Because of its position, mixing is likely to be important, and it becomes increasingly difficult to characterize the

flow with the idealized model. The combination of  $\Psi_M > 1$  and  $\Psi_P < 1$  suggests that the flow gradually accelerates, again due to the shape of the jet boundary that is now divergent. This re-acceleration of the flow seems to overcome any deceleration that would occur from momentum transfer to the suction flow. This could be because the jet surface area available for interaction with the suction flow is much smaller in comparison to that of Region 4. Finally,  $\Psi_T > 1$  indicates that heat is being gained either from viscous dissipation, or more likely from heat transfer with the warmer suction flow.

In general, it can be said that a combination of  $\Psi_M < 1$  and  $\Psi_P > 1$  is an indication of momentum loss to the suction flow, or of gradual compression forced by a converging motive jet shape. The opposite is true for the case of gradual expansion. Then  $\Psi_T > 1$  is an indication of heat being transferred from the warmer suction flow to the cooler motive flow, with potential secondary heat generation from viscous dissipation. At the supersonic velocities considered, any heat gain can result in flow deceleration, while heat loss can result in acceleration.

Looking at the experimental shadowgraph image in the middle of Fig. 3.8, angles  $\theta_3$ ,  $\theta_4$ , and  $\mu_{6i}-\alpha_6$  are measured to be  $35.5^\circ$ ,  $41.0^\circ$ , and  $39.0^\circ$ , respectively. Because the primary purpose of this analysis is to comment on the applicability of available turbulence models for the simulation of ejector flow, the correct model will accurately capture shock-boundary layer interactions that reproduce correct angles seen in the real flow field because they dictate the change in properties from one region to the next. After appropriate selection of the turbulence model, the same first-principles analysis detailed in Section 3.4 can be performed to find improved correction coefficients (although it is expected that the correction coefficients will remain relatively the same). In this way, locations of notable

heat and momentum transfer can be identified as shown above, emphasizing the need for local validation of the turbulence model at the specific on- or off-design condition.

In regions where momentum transfer to the suction flow seems higher, like in Region 4, flow conditions can be changed to ensure maximum contact. For example, increasing the velocity of flow at the exit of the motive nozzle would promote a smaller  $\theta_3$  and an elongated Region 4. This could be done by reducing momentum losses in the motive nozzle with the use of smoother wall profiles, or allowing for a larger motive nozzle exit area to increase nozzle expansion. This analysis also suggests that there may be some advantage to operating with underexpanded jets. The sample case above shows that from Region 3 to 4, the flow compresses with the corresponding drop in flow velocity. If instead the transition from 3 to 4 was across an expansion (as is the case for an underexpanded jet), the velocity in Region 4 would be higher, thus enhancing momentum transfer to the suction flow along the length of Region 4.

These are only two of many insights that can be taken from the correction coefficients to tailor ejector geometry for maximum ejector performance. However, it must be noted that while the analysis above is for a specific sample case, additional work is needed to verify if the above suggestions and observations are applicable to other ejector conditions, whether there is a difference in operational regime, inlet conditions, geometry, or jet type.

### **3.6 Conclusions**

This work presents an integrated computational, experimental, and analytical study of ejector flow characteristics from global properties of mass entrainment to local properties of flow feature location, strength, and non-ideal behavior. Comparison of experimental and

CFD results showed that while predictions of inlet and outlet conditions were good for on-design operation (within 8% error), predictions of off-design conditions displayed considerably larger errors. This difficulty in predicting off-design conditions was attributed at least partially to the errors in turbulence modeling from an inability to correctly predict shock/expansion wave interactions with the jet boundary layer. Two turbulence models were considered,  $k$ - $\epsilon$  RNG and  $k$ - $\omega$  SST, with ideal gas air flow in a 2D ejector with rectangular cross-section. While differentiation between these two turbulence models at the global scale was difficult, differences could be seen more clearly at the local scale. But these differences did not reflect the magnitude of difference in predicted secondary flow rate, which was much higher, 6%, for the off-design case than for the on-design case, only 0.1%. Therefore local features were not reflected in the different predictions of global features. In previous work by one of the authors (Hemidi *et al.*, 2009b), it was also found that there was no obvious relationship between the ability to predict local flow features and to predict global parameters.

The  $k$ - $\epsilon$  RNG turbulence model was shown to predict both global flow rates and the position of flow features less accurately. The  $k$ - $\epsilon$  RNG turbulence model is generally known to be a computationally inexpensive model that is good for first approximations of flows, but is not able to capture details of complex flows that are associated with severe pressure gradients or flow separation. Ejector flow is characterized by such complex phenomena, and pressure gradients are especially large. On the other hand, the  $k$ - $\omega$  SST turbulence model had better performance across the board with slightly lower error in predicting global parameters, and better prediction of flow feature position than the  $k$ - $\epsilon$  RNG model. This is probably due to the strengths of the  $k$ - $\omega$  SST model in predicting

compressible flows. Unfortunately, the  $k-\omega$  SST turbulence model requires proper refinement of the near-wall mesh to be accurate, often requiring longer computational times to solve.

The number of shock cells and angle of flow features were identified as better indicators of flow prediction accuracy, where in general for both turbulence models at the off-design condition, the number of shock cells was greater, indicating a more important mismatch of flow conditions, i.e., pressure, between the motive and suction streams. Therefore it can be concluded that the discrepancy in global inlet flow rates can be attributed to the inability of both turbulence models to predict local shock/expansion strength and interaction with the jet boundary. It is found that turbulence models can be adjusted to match the angle of flow features seen in shadowgraph visualizations of the flow in order to demonstrate the same flow feature strength.

A comparison of the CFD flow field and the 1D first-principles analytical model was able to identify regions of notable non-ideal effects with correction coefficients, hence identifying the relative strengths of momentum and heat transfer effects. It was found that in regions adjacent to the suction flow and further downstream, these effects became stronger as interaction with the suction flow increased, often due to heat dissipation from adjacent regions. Furthermore, the importance of matching flow feature angle was demonstrated during a comparison with a real flow image at the same flow conditions. The influence of heat transfer on ejector flow was also found to be quite important. With this information, suggestions were made as to how ejector flow geometry can be tuned to maximize the contact area between the motive and suction flows where momentum transfer seems to be highest. To the authors' knowledge, this is the first available analytical model

capable of probing the ejector flow field without the use of intrusive measurement techniques.

These findings imply the necessity for more accurate turbulence modeling, and provide specific avenues for improvement. Ejectors operate with phenomena that are typically very difficult to model, such as momentum transfer via shear layers, large pressure gradients, and shock/expansion interaction with boundary layers. These complex phenomena were shown to be especially prominent for off-design operation, indicating that if future turbulence models are to be validated rigorously for the application of modeling ejector flow, this validation must be done at off-design conditions with special attention to the prediction of suction flow rate. Furthermore, such validation must combine information from multiple measurements including global inlet and outlet conditions, shock visualization, and comparison with the idealized 2D modeling technique developed here. Such integrated analyses ensure due cognizance of the fundamental physics of the flow, therefore enabling more specific tailoring of geometry to individual flow features to improve ejector efficiency for a wide range of systems and conditions.

## CHAPTER 4

### SHADOWGRAPH VISUALIZATION OF CONDENSING R134A FLOWS THROUGH EJECTORS

In this chapter, the CFD and analytical modeling techniques, as well as the shadowgraph visualization technique developed in Chapter 3 are applied to a small-scale ejector refrigerant flow at ejector-based chiller operating conditions. Accurate simulation of such ejector flows has been challenging due to the difficulties in modeling two-phase supersonic flows of fluids other than air or steam at high temperature and pressure conditions. Such modeling is necessary for ejector design and operational optimization, but the models currently available have yet to be validated at flow conditions representative of an ejector-based chiller. A transparent ejector test section is designed, fabricated, and operated in an ejector-based chiller loop using R134a as the working fluid. Undistorted visual access allows for detailed shadowgraph visualization of the motive jet in the mixing section at various degrees of condensation. High-speed imaging is used with measured temperatures and pressures at the ejector inlets to validate the available analytical and CFD models of ejector flow. It is found that the best modeling techniques assume that the motive flow exits the motive nozzle at full thermodynamic equilibrium, and that the  $k$ - $\epsilon$  RNG turbulence model in ANSYS FLUENT captures these equilibrium conditions sufficiently at the local scale, along with flow features in the vicinity of the motive nozzle exit.

#### **4.1 Introduction**

It has been hypothesized in previous studies (Al-Ansary and Jeter, 2004; Hemidi *et al.*, 2009a) that the entrainment effect within the ejector (MER) can be augmented by forcing the presence of condensate droplets in the motive jet. Condensation would have the effect

of slowing the motive flow velocity while maintaining the mass flux available for momentum transfer to the suction flow. This would decrease the velocity mismatch between the motive and suction flows, consequently decreasing the corresponding exergetic losses and increasing ejector efficiency. A simple way to promote the formation of liquid droplets is to adjust the degree of superheat at the motive nozzle inlet. At high enough degrees of superheat, the motive nozzle outlet condition (state 2 in Fig. 1.5 (b)) would lie outside the saturation dome, producing a “dry” motive jet with no liquid droplets as in the top of Fig. 1.5 (b). Conversely, a lesser degree of superheat would result in expansion into the saturation dome, as shown in the bottom of Fig. 1.5 (b). Depending on the time scale of this expansion and the kinetics of droplet formation, droplets may form to produce a “wet” motive jet.

Being able to predict the exact outlet condition of such rapidly expanding (and potentially two-phase) flow has been a challenge, requiring detailed knowledge of metastable states and subcooled droplet nucleation and growth. While models of these flows do exist, the high temperatures and pressures of ejector flows in combination with the use of fluids other than air and steam have limited the ability to measure or visualize the flow. The present study uses direct observation of such condensing flows to determine the actual outlet condition of the motive nozzle, and compares shadowgraph images to the predictions of available models of nozzle flow. Knowing the exact outlet condition of the motive nozzle, the properties of the motive jet, the geometry of which is shown schematically in Fig. 4.1 (with various flow angles and vectors referred to in subsequent sections), can be assessed with greater accuracy to determine the nuanced effects of flow condensation on momentum and heat transfer characteristics in the mixing section. This



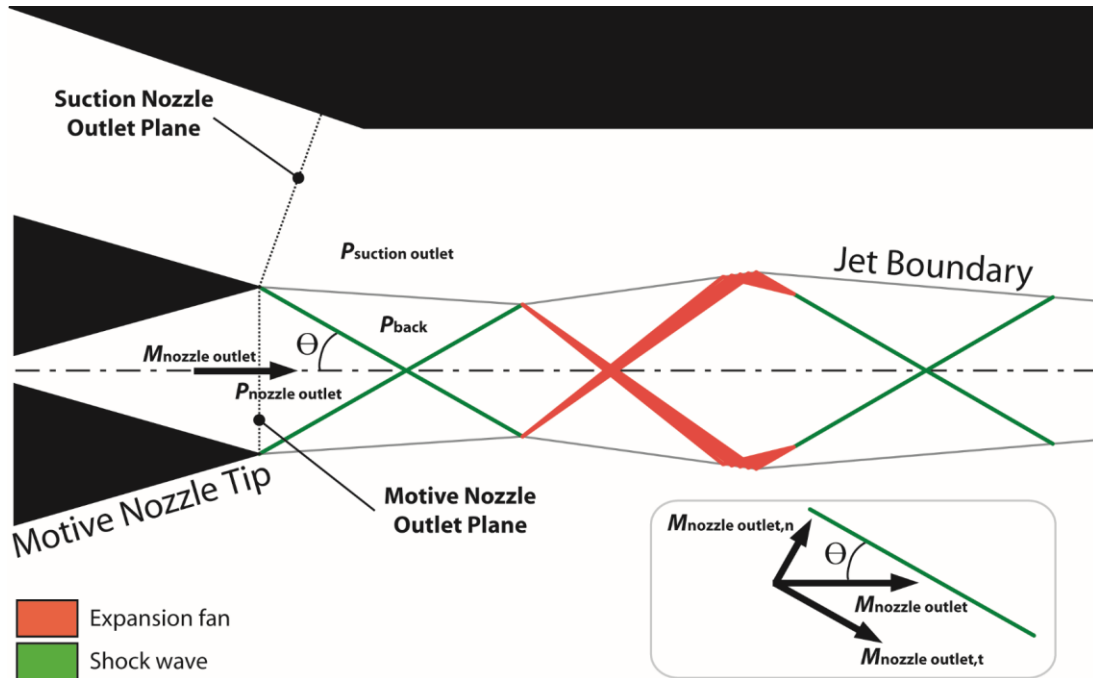


**Figure 4.1: Schematic of motive jet geometry. Green lines indicate a compression shock and red lines indicate expansion waves. Pressure across the jet boundary is constant such that  $P_{back} = P_{suction\ outlet}$ . Inset shows the decomposition of the motive flow velocity vector with respect to the first shock at angle  $\theta$ .**

information is critical to understanding the mechanisms of suction flow entrainment and overall ejector performance.

Considering the many assumptions necessary for analytical models, and the relative infancy of two-phase numerical modeling, visualization studies of condensing flows are critical for model validation. Visualization has the added benefit of capturing effects that may not be realizable even with the most advanced CFD models, including droplet coalescence, development of wall films, unsteady effects, or the nature of droplet drag effects. Many of the visualization studies in the literature have been conducted for the purpose of understanding internal flow in constant cross-sectional area ducts (Matsuo *et al.*, 1999) and/or flows with air. Visualization studies pertaining specifically to ejector flow

are much less common, and no known studies visualize ejector flow with fluids other than air or steam. In this chapter, a simplification of the Schlieren technique - shadowgraph visualization - is used to image the flow of refrigerant R134a through an ejector operating under conditions seen in an ejector-based chiller, and is based on previous work by the author (Little *et al.*, 2012). To the authors' knowledge, this is the first study to visualize refrigerant flow through an ejector operating at real cycle conditions. As such, unique pure fluid flow dynamics inside an ejector can be observed directly.

## **4.2 Experimental Approach**

### **4.2.1 Ejector-Based Chiller**

A full ejector-based chiller system was built and operated with R134a as the working fluid to provide the desired inlet and outlet conditions at the ejector test section. A schematic of the system is provided in Fig. 4.2 with the locations of temperature, pressure, and mass flow rate measurements indicated. Temperatures are measured with T-type thermocouples (accuracy  $\pm 0.25^\circ\text{C}$  after calibration), pressures are measured with Rosemount 2088 and 3051S pressure transducers (accuracies  $\pm 0.8$  kPa for  $P_{\text{condenser}}$ ,  $\pm 0.2$  kPa for  $P_{\text{evaporator}}$ ,  $\pm 6$  kPa for  $P_{\text{boiler}}$ ), and mass flow rates are measured with Rheonik RHM04 Coriolis flow meters (accuracies  $< 1.6\%$  reading for  $\dot{m}_{\text{suction}}$ ,  $< 0.12\%$  reading for  $\dot{m}_{\text{motive}}$ ). Heat inputs to the boiler and evaporator are provided by Watlow cartridge heaters, and the power provided to these heaters is measured using Ohio Semitronics AC watt transducers (accuracies  $\pm 20$  W and  $\pm 15$  W for boiler and evaporator heaters, respectively, and  $\pm 5$  W for superheater). Power is regulated using solid state controllers from Payne Engineering. Heat is removed from the condenser with a NESLAB Merlin M150 recirculating chiller, and an Exergy shell-and-tube heat exchanger serves as the condenser. Fluid is circulated

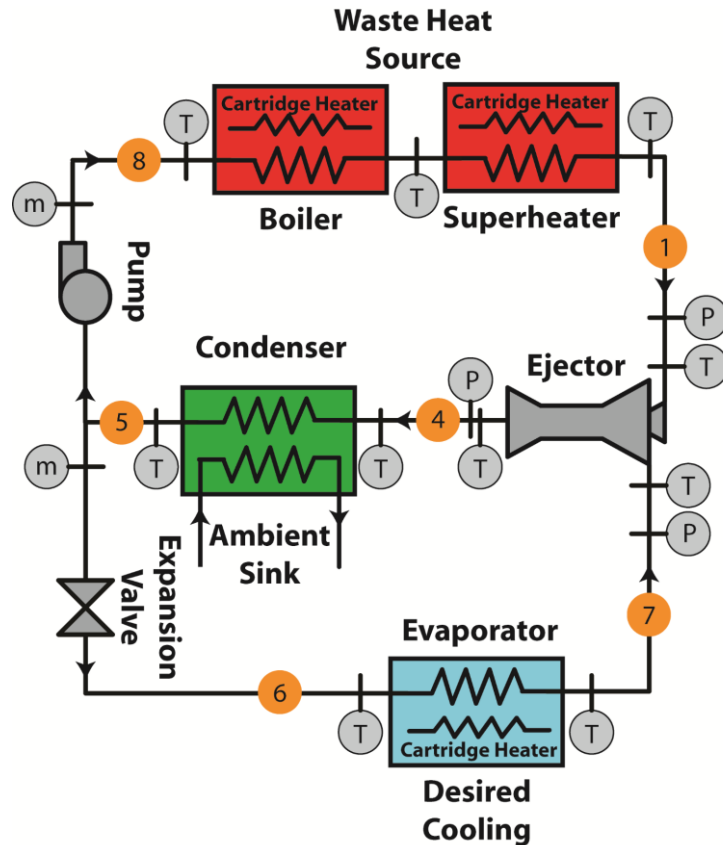


**Figure 4.2: Schematic of ejector-based chiller test facility used to provide desired inlet and outlet conditions to transparent ejector test section. Motive flow enters the ejector at state 1, and suction flow enters at state 7. Locations of temperature,  $T$ , pressure,  $P$ , and mass flow rate.**

through the upper loop using a P100 diaphragm metering pump from Hydra Cell with a variable frequency controller. No apparent cavitation was encountered during pump operation. An NI SCXI-1000 DAQ system was used to log the acquired data.

#### **4.2.2 Transparent Ejector Test Section**

The ejector test section was designed to have a rectangular cross-section such that a flat borosilicate glass window with a low index of refraction could be used to provide undistorted and clear optical access to the area at the motive nozzle outlet. The dimensions of the ejector geometry shown in Fig. 4.3 were determined using basic gas dynamics principles and best practices set forth by the ASHRAE equipment handbook (ASHRAE,

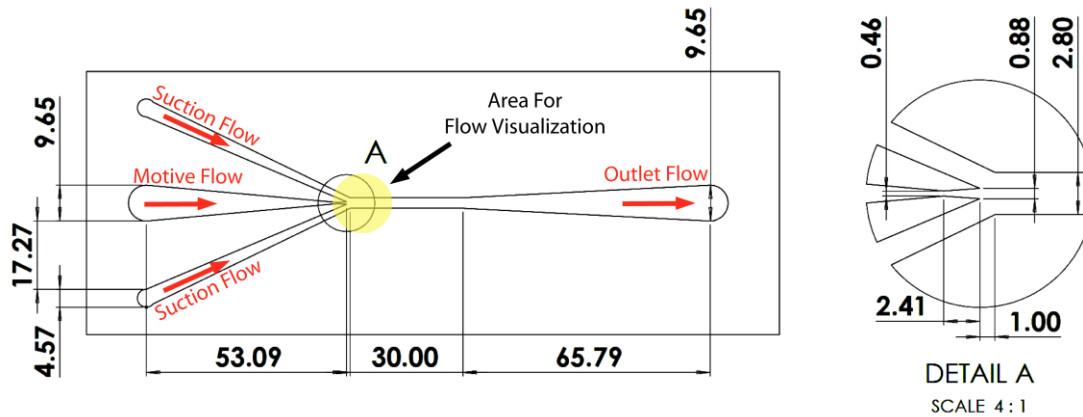


**Figure 4.3: Schematic of ejector plate showing ejector geometry and the area of interest for visualization highlighted. All dimensions are in mm.**

1983) for steam-jet refrigeration equipment. The area of interest for visualization is highlighted. The entire ejector was fabricated from 303 stainless steel, using a wire EDM to cut the geometry in the ejector plate. An exploded view of the test section is provided in Fig. 4.4, with a photograph of the actual test section in Fig. 4.5. The back plate contains the fluid inlet ports for the motive and suction flows, as well as the single outlet port for the outlet flow. The suction inlet port is split in two to ensure a symmetric flow pattern for the rectangular ejector geometry used here. The back plate also contains a pocket in which a flat mirror (optics quality, 50 mm x 50 mm, enhanced aluminum coating, BOROFLOAT substrate, 10 mm thickness, and surface accuracy of  $\frac{1}{4} \lambda$ ) is placed for visualization, as discussed in Section 4.2.3. The front plate contains the borosilicate sight glass. Both plates were polished to ensure a good seal between them and the ejector plate when assembled and pressurized. The seal around the sight glass was made using refrigerant-compatible high temperature silicone RTV sealant. The seal between the ejector plate and the front and back plates was established using a gasket made from thin ( $t = 0.397$  mm) sheets of corrosion-resistant fluorosilicone rubber with a hardness of 60A, laser cut to accommodate the geometry on the ejector plate. After assembly and compression of the gasket, the depth

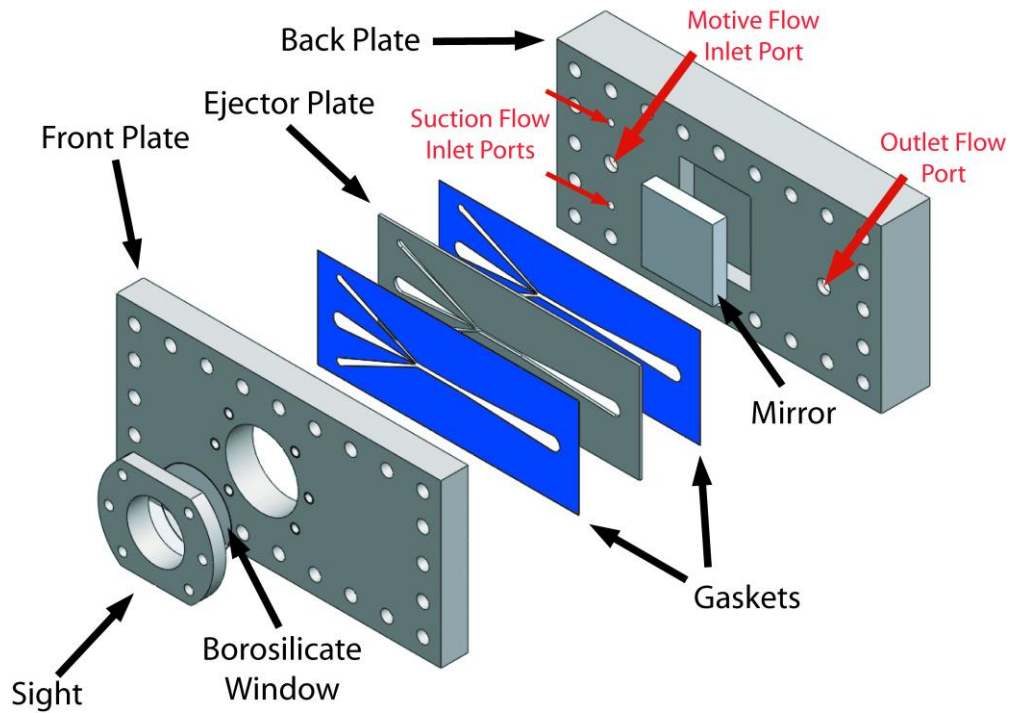


**Figure 4.4: Exploded view of transparent ejector test section showing major components (front plate, back plate, ejector plate) and minor components (mirror, sight/window, gaskets). Motive and suction inlet ports are indicated in the back plate where suction inlet is split in two to maintain flow symmetry. Outlet flow port is also shown in back plate.**

of the flow path through the ejector geometry (i.e., the distance between the front and back plates) was determined to be 2.2 mm. This test section depth was chosen such that, with this rectangular cross-sectional geometry, the total surface area of the motive jet available for direct contact with the suction flow would be equivalent to that of a conventional circular cross-sectional ejector operating at the same capacity.

The motive nozzle was sized for a nominal motive mass flow rate of  $\sim 0.75 \text{ kg min}^{-1}$  while maintaining a constant suction inlet saturation temperature and pressure of  $33.3^\circ\text{C}$  and  $848 \text{ kPa}$ , respectively, and  $11 \text{ K}$  superheat to ensure single-phase conditions at the suction nozzle inlet. The ejector outlet saturation temperature and pressure was maintained

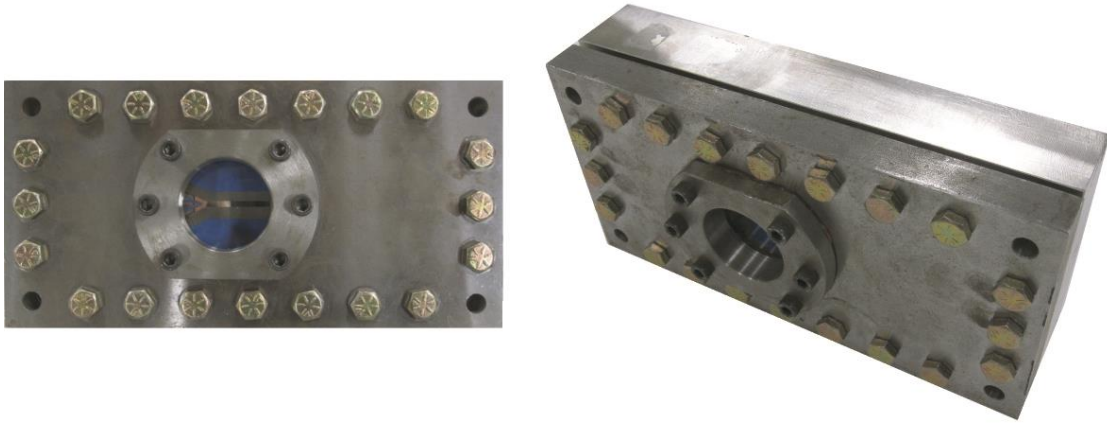


**Figure 4.5: Photographs of assembled transparent ejector test section, designed specifically for undistorted flow visualization of high temperature and high pressure refrigerant flows.**

at 38°C and 965 kPa, respectively, ensuring choked suction flow and on-design operation of the ejector.

Starting at an 11.5 K superheat condition at the inlet to the motive nozzle, the heat input from the boiler was decreased incrementally to change the motive nozzle inlet enthalpy until a significant drop in MER was observed. For the range of motive inlet conditions considered, the motive nozzle inlet pressure changed from 3003 to 2723 kPa with the corresponding  $T_{\text{sat}}$  ranging from 86 to 82°C. This change produced motive inlet conditions ranging from well outside the vapor-liquid dome to one well inside the dome, and a transition from dry to wet jet conditions at the motive nozzle outlet. The test point conditions are given in Table 4.1.

#### **4.2.3 Shadowgraph Flow Visualization**

These changes in flow conditions were imaged using the shadowgraph visualization technique. Shadowgraph images can detect sharp density gradients produced by shocks and expansions. Differences in density cause changes in the refraction index of the flow, and the refracted light beams cast shadows or bright spots as different light rays diverge or

**Table 4.1: Experimental motive inlet conditions and resulting MER values. Motive inlet enthalpy is calculated using measured  $T$  and  $P$  for superheated conditions, and an energy balance about the boiler for saturated conditions.**

$P_{m,inlet}$ [kPa] ( $\pm 6$ kPa)	$T_{m,inlet}$ [C] ( $\pm 0.25^\circ\text{C}$ )	$h_{m,inlet}$ [kJ kg <sup>-1</sup> ] ( $\pm 0.5\%$ )	Superheat [K]	MER [-] ( $\pm 2\%$ )
3003	97.8	301.3	11.5	0.675
2986	95.2	297.6	9.3	0.654
2992	93.0	293.5	7.0	0.659
2961	89.8	288.5	4.2	0.636
2942	87.3	284.1	2.1	0.623
2911	85.3	277.8	sat ( $x=0.98$ )	0.621
2878	84.7	273.8	sat ( $x=0.94$ )	0.612
2833	83.9	267.2	sat ( $x=0.87$ )	0.604
2793	83.2	262.2	sat ( $x=0.82$ )	0.597
2756	82.6	256.8	sat ( $x=0.77$ )	0.570
2723	82.0	251.4	sat ( $x=0.72$ )	0.539

converge, respectively. Unlike a Schlieren image that shows the gradient of refractive index, a shadowgraph shows the change in this refractive index gradient, or in other words, the Laplacian of the refractive index (Settles, 2001).

The shadowgraph setup used here is shown schematically in Fig. 4.6, with the five main components of the setup indicated. The first is the light source, produced by a Fiber-Lite MI-152 high-intensity illuminator from Dolan-Jenner, and condensed using a 40X microscope objective. The second is a plano-convex lens (40 mm diameter, 300 mm FL, MgF<sub>2</sub> coating) responsible for collimating the incoming light before it passes through the test section, as well as focusing the outgoing light going to the camera. The third is the flat mirror inlaid in the back plate of the test section, as mentioned above, responsible for reflecting light back through the test section to the camera. The fourth item is a FASTCAM SA4 high-speed Photron video camera (model 500K-M1) fitted with a high magnification 12X Navitar lens. The fifth item is a cube beam splitter (30 mm sides,  $\frac{1}{4} \lambda$  MgF<sub>2</sub> coating) reflecting 50% and transmitting 50% of the incident light. As a result, only 25% of total

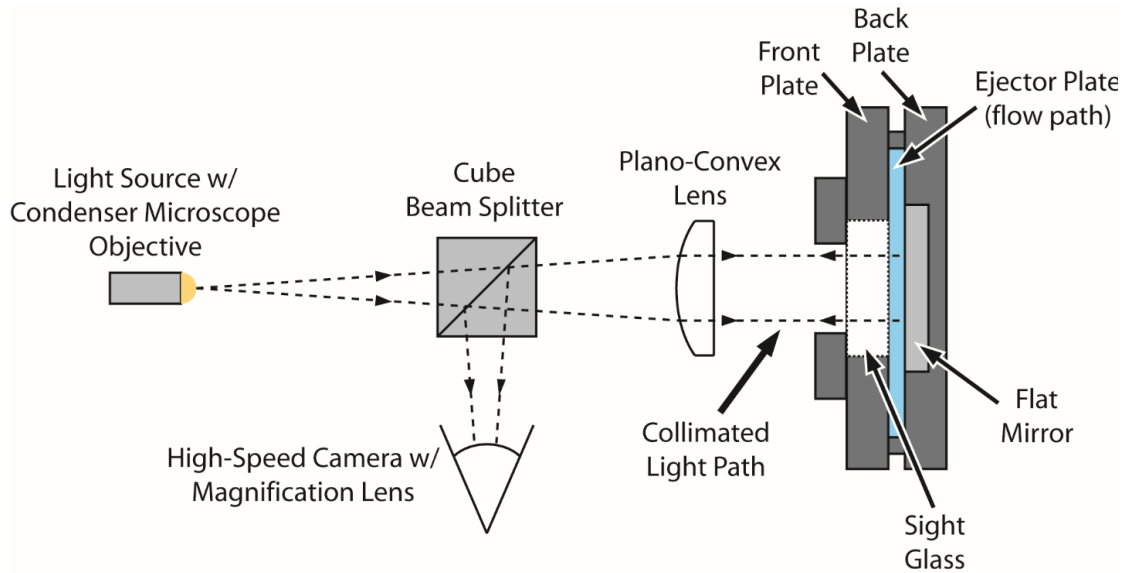


**Figure 4.6: Schematic of shadowgraph visualization setup. Major visualization components include a condensed light source, plano-convex lens, flat mirror within the ejector test section, cube beam splitter, and high-speed camera with magnification lens.**

light supplied by the light source reaches the camera after passing through the beam splitter twice. The beam splitter eliminates distortion effects related to asymmetric light beam paths. The images presented in this work show the small region near the outlet of the motive nozzle, as indicated in Fig. 4.3, where flow features were strong enough to be visible with the shadowgraph technique. A grid target reticule was used to check for correct alignment of visualization components, trueness of the captured images, and spatial measurement of nozzle tip geometry and flow features during operation.

As shown in Fig. 4.3, the motive nozzle geometry is quite small; on the order of 1 mm. A magnifying lens was required on the camera to capture the flow features in the motive jet. Therefore, any imperfections in the test section introduced by mirror imperfections, dust, particulate, or lubricants from the upstream pump, valves, and/or sealants were notable in the images. A comparison of flow images to an image with zero



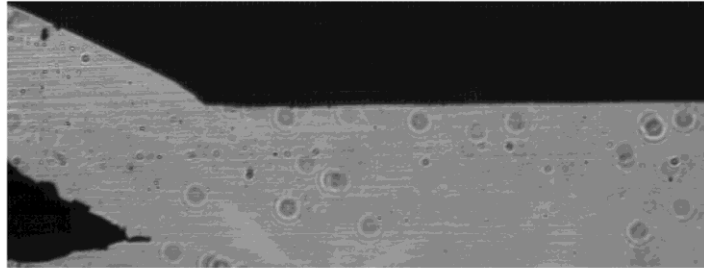
flow (calibration image) allowed for identification and removal of these imperfections. A sample set of images is shown in Fig. 4.7, where a half-image of the area at the motive nozzle tip is shown. In Fig. 4.7 (a), the raw image of zero flow shows striations and dust on the mirrored surface as well as imperfections and dust on the borosilicate window glass. Figure 4.7 (b) shows a raw image of flow where the same imperfections exist along with minor rivulets of liquid refrigerant flow coming from the suction line. Also, the slight swelling of the gasket that can be seen with a change in shape of the motive nozzle tip (the effect of which is discussed later). Figure 4.7 (c) shows a corrected image of the flow with imperfections removed using image analysis software to eliminate image features that were obviously due to test section contamination.

### **4.3 Modeling and Data Reduction**

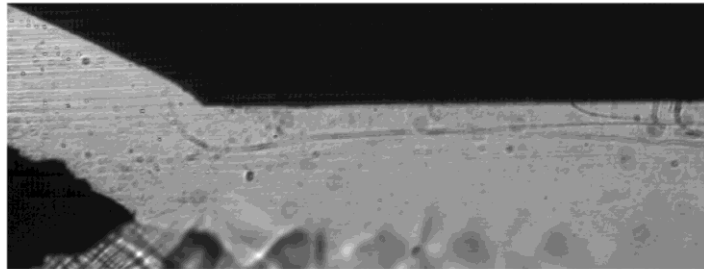
The images collected using the above approach provide useful information for a variety of analyses. The specific analysis in this study compares measured values of motive nozzle back pressure from images to those predicted by simplified analytical and CFD models. Such a comparison helps in the selection of the best modeling technique, and pinpoints the exact conditions at the motive nozzle exit needed to predict suction flow entrainment and related ejector performance in Chapter 5.

#### **4.3.1 Analytical Model**

The flow phenomena inside the motive nozzle are governed by the combined effects of short time scales for the expansion process, detailed kinetics of droplet formation, supersonic speeds, and/or droplet coalescence and impingement. A detailed discussion of related metastable flow phenomena can be found in Carey (2008) and Bakhtar *et al.* (2005). There are two ways to approximate the exit condition of the motive nozzle



(a)



(b)



(c)

**Figure 4.7: Sample set of ejector test section images showing (a) raw image with zero flow, (b) raw image with flow, and (c) corrected image with flow.**

analytically to account for the relevant metastable effects. One method is to assume that the flow entering the motive nozzle behaves as an ideal gas as it quickly expands through the nozzle. This is described as “frozen flow” behavior, and assumes that zero flow condensation occurs. It sets a lower limit for flow temperature, pressure, and density at the motive nozzle exit. The other method is to assume the flow is at full thermodynamic equilibrium at every point along the motive nozzle flow path, ignoring any kinetics of droplet formation that may occur from the presence of metastable effects. This is

considered “equilibrium flow” behavior and sets an upper limit for nozzle outlet temperature, pressure, and density, and also provides a prediction of quality - the maximum possible amount of condensation that can occur at the nozzle exit. The real exit condition of the motive nozzle lies between the predictions of the frozen and equilibrium models, depending on the time available droplet formation and growth as dictated by the degree of flow subcooling. Chapter 5 (Little *et al.*, 2016) provides a full explanation of these models and associated analysis, finding that the motive nozzle outlet condition likely follows the equilibrium model flow condition.

Starting from the motive nozzle inlet condition measured from experiments, as indicated in Table 4.1, the outlet of the motive nozzle can be calculated assuming isentropic flow, conservation of mass, and conservation of energy at the nozzle outlet. For the frozen flow model, the ideal gas equation of state is used to close the set of equations, whereas for the equilibrium model, the Tillner-Roth and Baehr equation of state for R134a (1994), a fundamental equation of state for the dimensionless Helmholtz free energy, is needed to determine density and provide closure. Thus, the upper and lower bounds of  $T$ ,  $P$ , and  $\rho$  at the motive nozzle outlet, as well as maximum possible condensation from the equilibrium value of quality, can be determined.

The first observed flow feature after the outlet of the motive nozzle is a shock in all experimental cases, and its angle provides a ratio of pressure (and temperature and density) across the shock from the motive nozzle outlet pressure to the motive nozzle back pressure. As mentioned above, the motive nozzle back pressure is taken to be equivalent to the suction nozzle outlet pressure because both states are found on opposite sides of the constant pressure jet boundary. Figure 4.1 shows a schematic of this shock with definitions

of flow angles and vectors needed for this analysis. It is assumed that the flow exiting the motive nozzle has a flow angle of  $0^\circ$  with respect to the flow direction, and  $\gamma$  is equal to that at the motive nozzle inlet in the 11.5 K superheat case. Using ideal gas relations for adiabatic flow with constant specific heats, the ratio of pressure across the shock can be found as

$$\frac{P_{back}}{P_{nozzle\ outlet}} = \frac{1 + \gamma M_{nozzle\ outlet,n}^2}{1 + \gamma M_{back,n}^2} \quad (4.1)$$

$$M_{back,n} = \sqrt{\frac{M_{nozzle\ outlet,n}^2 + \frac{2}{\gamma - 1}}{\frac{2\gamma}{\gamma - 1} M_{nozzle\ outlet,n}^2 - 1}} \quad (4.2)$$

where  $P_{nozzle\ outlet}$  is the pressure at the outlet plane of the motive nozzle,  $P_{back}$  is the back pressure found after the first shock (and equal to the suction nozzle outlet pressure),  $M_{nozzle\ outlet,n}$  is the normal component of the nozzle exit flow Mach number with respect to the first shock. The speed of sound is determined from the Tillner-Roth and Baehr equation of state for superheated conditions. For two-phase conditions, the speed of sound is calculated using the formulation of Liu and Groll (2008). The value of  $P_{back}$  can be compared to the value of pressure at the suction nozzle outlet to determine the location of the real nozzle outlet condition within the range of predicted conditions. The value of pressure at the suction nozzle outlet is found from measured suction nozzle inlet conditions. Flow through the suction nozzle has a relatively low speed and experiences minor expansion, making it possible to assume that the suction flow is always at equilibrium. As such, the equilibrium flow relations are used to determine the pressure at the outlet of the suction nozzle.

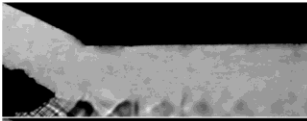
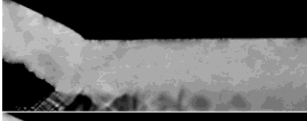
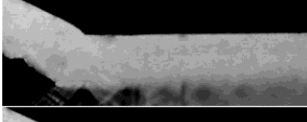
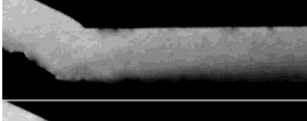
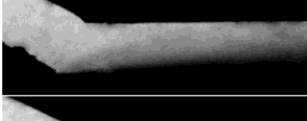
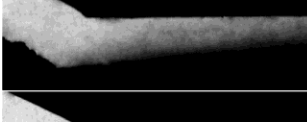
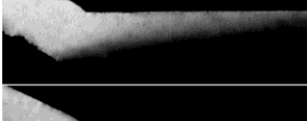
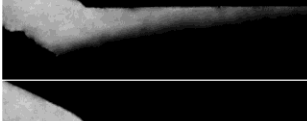
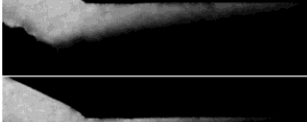


### **4.3.2 CFD Model**

To validate the performance of readily available CFD models, contours of predicted Mach number are compared to the shadowgraph images. This comparison allows for local validation of the motive nozzle back pressure, angle of shock flow features, and number of shock cells. A 2D steady-state simulation is performed using the computational package ANSYS FLUENT v13 (2010). All calculations are set to be performed in the vapor phase with R134a using the REFPROP NIST database that references the Tillner-Roth and Baehr equation of state (1994). The  $k$ - $\epsilon$  RNG turbulence model is used with enhanced wall functions and a second order upwind discretization, chosen for being less computationally expensive. All simulations use meshes  $> 113$  k elements. The CFD models in Chapter 3 (Little *et al.*, 2015) for similar geometries found that a mesh  $> 85$  k elements is sufficient to attain mesh independent results.

## **4.4 Results and Discussion**

### **4.4.1 Effect of condensation on MER**

The images shown in Fig. 4.8 were taken at the conditions listed in Table 4.1, ensuring a constant motive mass flow rate, suction inlet temperature and pressure, and ejector outlet pressure at each data point. The shadowgraph imaging technique detected shock and expansion features starting at the motive nozzle throat and finishing as they dissipate in the mixing section. It is evident that as the motive nozzle inlet enthalpy drops and the flow becomes more condensed at the nozzle outlet, the jet becomes considerably darker from the higher degrees of flow condensation. Furthermore, the rising quantity of condensate increasingly expands to span the entire width of the mixing section. The values of MER given in Table 4.1 and Fig. 4.8 show a general gradual decrease, indicating that the performance of the ejector deteriorates steadily with decreasing motive inlet superheat.

	Nozzle Inlet Superheat	MER	Nozzle Outlet Quality (equilibrium model)
	11.5 K	0.675	1.00
	9.3 K	0.654	1.00
	7.0 K	0.659	0.99
	4.2 K	0.636	0.97
	2.1 K	0.623	0.95
	saturated ( $x = 0.98$ )	0.621	0.93
	saturated ( $x = 0.94$ )	0.612	0.91
	saturated ( $x = 0.87$ )	0.604	0.88
	saturated ( $x = 0.82$ )	0.597	0.86
	saturated ( $x = 0.77$ )	0.570	0.84
	saturated ( $x = 0.72$ )	0.539	0.82

**Figure 4.8: Images of ejector flow at decreasing motive inlet superheat with experimental values of MER. Motive nozzle outlet quality values according to the equilibrium analytical model are also given. Exact flow conditions can be found in Table 4.1.**

This is most likely due to lower motive inlet pressures. As the difference in pressure between the motive inlet and suction inlet decreases, there is less expansion in the motive

nozzle available to produce work for the ejector pumping effect. Another factor that likely contributes to the drop in MER is the increasing presence of condensation. Although it has been argued by some (Al-Ansary and Jeter, 2004; Hemidi *et al.*, 2009a) that condensation may help enhance ejector flow by reducing flow irreversibilities related to velocity and temperature mismatches between the motive and suction flows, this is only likely the case when qualities are high and condensate droplets are very small such that droplet drag effects are negligible. It is possible that this is the cause of the slight rise in MER seen from the 9.3 K to 7.0 K superheat cases, because the degree of condensation seen is very small. But after the 7.0 K superheat case, condensation becomes quite dramatic and is more likely to cause significant drag and turbulence effects in the mixing section.

#### **4.4.2 Analytical model performance**

Using these images, the angle of the first shock,  $\theta$ , can be measured for use with the analytical models discussed in Section 4.3.1. This angle could only be discerned in the first three flow images in Fig. 4.8, which are also shown in Fig. 4.9 (focusing on the motive jet structure right after exiting the motive nozzle) in comparison to Mach number contours from the CFD simulations. The angle of the first flow feature for each frame, indicated in Fig. 4.9, was measured using image analysis software and found to be  $41.5^\circ$ ,  $41.0^\circ$ , and  $40.5^\circ$  for the 11.5 K, 9.3 K, and 7.0 K superheat cases, respectively. The uncertainty on the measured value of angle was conservatively assumed to be quite large at  $\pm 3^\circ$  to include the full range of possible angles, as it was difficult to identify the flow feature accurately because of imperfections in the test section. The predicted motive flow back pressures for both the frozen and equilibrium models are provided in Table 4.2 along with the predicted values from the CFD simulations. As noted above, the equilibrium model predicts an upper

**Table 4.2: Comparison of experimentally measured back pressure values to those predicted by analytical and CFD models.**

Superheat [K]	$\theta$ [deg]	Model		$P_{back}$ [kPa] (predicted)	$P_{back}$ [kPa] (measured) ( $\pm 0.1\%$ )
11.5	$41.5 \pm 3^\circ$	Analytical	Equilibrium	$775 \pm 97$	818
			Frozen	$719 \pm 89$	
	38.0	CFD		739	
9.3	$41.0 \pm 3^\circ$	Analytical	Equilibrium	$752 \pm 96$	820
			Frozen	$700 \pm 89$	
	38.0	CFD		740	
7.0	$40.5 \pm 3^\circ$	Analytical	Equilibrium	$733 \pm 95$	820
			Frozen	$687 \pm 88$	
	38.0	CFD		741	

limit value of back pressure, whereas the frozen mode predicts a lower limit value. However, a comparison of analytical values to measured values shows that the real back pressure is higher than the upper limit predicted by the equilibrium model (albeit within the uncertainty range). This is likely due to imperfections in the transparent test section associated with assembly and operation that may have caused deviations from the flow geometry defined in Fig. 4.3. First, it is likely that critical dimensions of the ejector, specifically the motive nozzle throat and outlet cross-sectional areas, as well as the cross-sectional area of the mixing section, were different or changed because of the potential indeterminate flexure of the gasket layer on either side of the ejector plate. During assembly of the test section, the gasket was known to squeeze into the test section slightly at some locations, and to not fill in close enough to the ejector geometry in others. As such, the functional geometry of the ejector could be estimated, but not known precisely. Furthermore, at the high operating pressures under consideration, it was difficult to provide a satisfactory seal at the very tip of the motive nozzle. From the flow images in Figs. 4.8 and 4.9, it does not seem that there is any flow leakage out of the motive nozzle to the suction flow, but the motive nozzle tip was not perfectly sharp to match the Fig. 4.3 geometry used in the models. Because the outlet cross-sectional area of the motive nozzle



was so critical for determining back pressure, this is the most likely source of any *systematic* error in the results in Table 4.2.

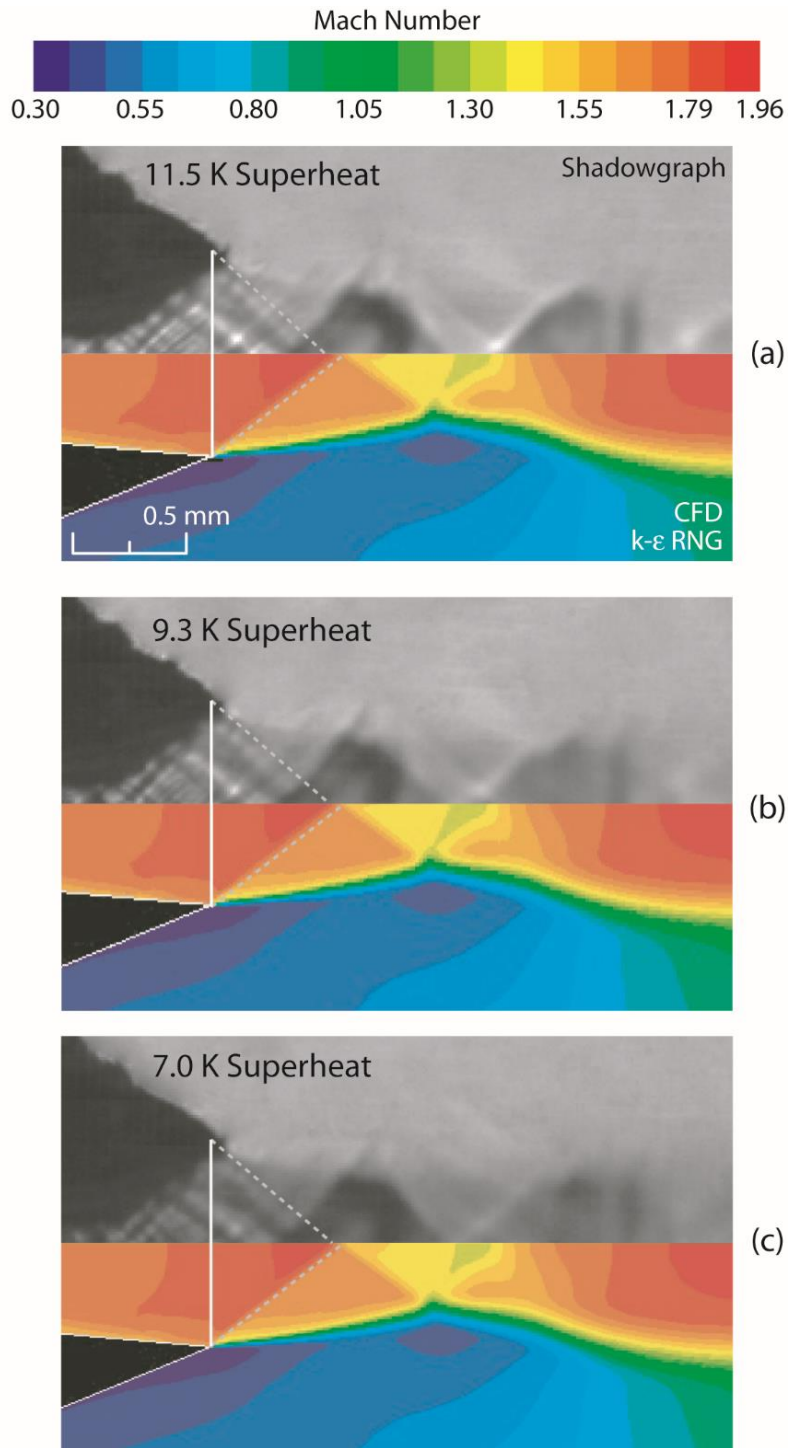


**Figure 4.9:** Comparison of first three superheat conditions with clear motive jet flow features. Dotted lines indicate angles measured for analytical and CFD analyses, given in Table 4.2.

Apart from this systematic error, there seems to be an additional error that increases with decreasing superheat. Both the equilibrium and frozen flow models assume isentropic flow through the nozzle, but the actual flow contains irreversibilities related to 3D flow effects (i.e., wall friction), condensation shocks, and droplet drag, all of which become more dominant at lower superheat conditions. The presence of these irreversibilities would have the effect of reducing the expansion in the nozzle such that the real back pressure would be higher than that predicted by the model. Therefore, the higher errors in the analytical model predictions at lower superheats could be an indication of the entropy generation from two-phase flow effects. However, this finding is not conclusive, considering the fact that the measured value of  $\theta$  (with high uncertainty) is the major parameter determining the value of predicted back pressure.

With these uncertainties in mind, the equilibrium model generally tends to predict the value of back pressure the best. This implies that the real flow exiting the motive nozzle has come to full equilibrium, and the quantity of condensation as well as flow properties at the exit of the motive nozzle can be found using the equilibrium model. This finding is applicable to the motive nozzle geometry shown in Fig. 4.3. Changes to this geometry, namely a larger angle for the divergent portion of the motive nozzle, would result in a faster expansion of the motive flow. In such a case, the likelihood of the motive flow coming to full equilibrium by the exit of the motive nozzle is lower. The nozzle shown in Fig. 4.3 was designed based on best practices from the ASHRAE handbook (ASHRAE, 1983) for steam-jet refrigeration equipment, which states that this divergent angle (total included angle) should be between 8 and 15°. The present geometry has a divergent angle of 10°.

Therefore, this angle should be sufficient for equilibrium conditions to be met under conditions typical of ejector operation in a chiller.

#### **4.4.3 Numerical model performance**

As mentioned in Section 4.3.2, the CFD simulations are performed in ANSYS FLUENT using the Tillner-Roth and Baehr (1994) equation of state for R134a. Because this same equation of state was used for the analytical equilibrium model, it is expected that the results from the CFD simulations match or come close to those of the equilibrium model. It can be seen from Table 4.2 that this is generally the case. Any discrepancies are likely due to an error in the measurement of  $\theta$ . Out of all models of the ejector flow, the CFD simulation can be considered the most accurate because it reflects equilibrium flow behavior, shown above to have the best match with experimentally measured values, and it includes important 2D flow effects. The major portion of the error between the CFD simulations and experiments seen in Table 4.2 is probably due to the systematic error introduced by the geometry differences mentioned above.

The detail of the CFD model allows for a more comprehensive comparison of motive jet flow geometry. The numerical value of  $\theta$  for all cases was found to be constant at  $38^\circ$ , whereas the shadowgraph images show this angle becoming smaller with decreasing superheat. The effect of two-phase flow would be to decrease the strength of the shocks (Bartosiewicz *et al.*, 2005), making  $\theta$  smaller. This seems to be evident in the shadowgraph images, but is not reflected in the CFD. It was found in Chapter 3 that matching this angle as well as the number of shock cells is critical to determining the accuracy of a given turbulence model (Little *et al.*, 2015). Diffusive behavior is characterized by fewer shock cells and weaker shocks. In Fig. 4.9, it seems that the CFD model is showing a slight excess

of diffusive behavior, but the predictions from the  $k$ - $\epsilon$  RNG turbulence model is generally good at this local scale. The most notable discrepancy between the visualized flow and the modeled flow field is the axial position of flow features. Each feature in the shadowgraph image seems to be translated upstream by  $\sim 0.25$  mm with respect to the CFD simulation. This is likely due to an imperfect seal at the motive nozzle tip, and/or a nozzle tip that was not perfectly sharp in the test section. Both of these factors would force the start of the first shock flow feature further upstream as they appear in the images, and can be attributed to experimental error rather than a deficiency in the CFD model.

Considering these factors, it seems that the diffusive behavior of the flow is predicted satisfactorily for the on-design conditions considered in Fig. 4.9 based on both the number of shock cells present, and the angle of observed flow features. Unfortunately, no conclusion can be made as to the accuracy of the CFD modeling technique at conditions where significant condensation occurs, because flow features cannot be discerned through the darkness caused by the condensed flow. Nonetheless, from both Fig. 4.9 and the modeling results in Table 4.2, it seems that assuming that equilibrium is reached by the end of the motive nozzle is valid, and that metastable effects can be ignored without significant error when predicting conditions inside the mixing section of the ejector where flow entrainment occurs.

#### **4.5 Conclusions**

The influence of two-phase flow on the performance of ejectors has been a subject of discussion in the literature, mostly because of the difficulty of modeling two-phase supersonic flows accurately, and the difficulty of having undistorted optical access to high pressure and temperature refrigerant flows at the mini scale. This study provides guidance

on these issues with a full ejector-based chiller setup fabricated with a special transparent ejector test section designed for undistorted optical access. Shadowgraph visualization is used to image the flow at conditions of varying flow condensation and associated ejector performance. It is found that the performance of the ejector component decreases at higher degrees of condensation. The flow images captured are used to validate pre-existing analytical and CFD models of the ejector flow. Comparison of these models with measured values of motive nozzle back pressure show that the flow at the exit of the motive nozzle is likely at full equilibrium, and the quantity of condensation in the motive jet can be determined by evaluating quality at equilibrium, ignoring any metastable flow effects.

This is the first known study to image an ejector flow with a fluid other than air or steam at inlet/outlet conditions relevant to ejector use in an ejector-based chiller. As such, the unique dynamics of fluid flow where both condensate droplets and the bulk flow are of the same fluid (unlike air-water mixtures) can be captured for the first time and used as a basis to validate many models of ejector flow that had previously been unverifiable. With these new insights, two-phase ejector modeling can be refined for tailoring ejector design and operation, leading to optimized ejector-based chiller performance

**CHAPTER 5**

**COMBINED EFFECTS OF FLUID SELECTION AND FLOW  
CONDENSATION ON EJECTOR OPERATION IN AN EJECTOR-  
BASED CHILLER**

This chapter investigates the possibility of using two-phase flow effects to optimize the COP of an ejector-based chiller. Experiments are performed with wet R134a and dry R245fa fluids, changing the conditions at the motive nozzle inlet to realize different two-phase flow conditions at the motive nozzle exit where subsequent suction flow entrainment occurs. Using findings from Chapter 4, models are developed for the motive nozzle and mixing sections to differentiate between the roles of momentum transfer, heat transfer, and two-phase flow on suction flow entrainment. These models provide the necessary information to draw conclusions about the role of phase change on suction flow entrainment and overall cycle COP.

**5.1 Introduction**

Conventional operation of power cycles dictates that the inlet condition to an expansion device must be superheated by  $>10$  K (typically between 25 and 30 K for gas turbines (ASME, 1992; Boyce, 2006)). This is because in radial and axial expanders, two-phase flow is avoided to prevent damage to rotating machinery through detrimental droplet impingement effects on sensitive, high-speed components. But because of the mechanical simplicity of the ejector, these effects do not pose appreciable concerns, and a wider range of conditions is allowable at the motive nozzle inlet (state 1 in Fig. 1.5) for safe operation. The present work considers the relaxation of this constraint to investigate the effects of

condensation in the motive flow on ejector operation and overall cycle performance defined by the coefficient of performance:

$$COP = \frac{\dot{Q}_{evaporator}}{\dot{Q}_{boiler} + \dot{Q}_{superheater}} \quad (5.1)$$

Previous ejector studies have either focused on the development of the ejector-based chiller cycle or on the ejector component, whereas the work in this chapter combines the two. Furthermore, previous studies have focused on air ejectors with water droplets. In an ejector-based chiller, the operating fluids have properties and operating conditions significantly different from those of air, and both the vapor and liquid phases are of the same fluid. This could result in significantly different gas dynamics than those seen in the air-water mixtures of previous studies.

It has been hypothesized in previous studies (Al-Ansary and Jeter, 2004; Hemidi *et al.*, 2009a) that the entrainment effect within the ejector can be enhanced by forcing the presence of liquid droplets in the motive jet. From a mass conservation standpoint, condensation would reduce the motive flow velocity while maintaining the mass flux in the motive jet that is available for momentum transfer to the suction flow. This would decrease the velocity mismatch between the motive and suction flows, potentially decreasing corresponding exergetic losses. The expected net effect would be to increase system COP due to the improved ejector efficiency, assuming viscous drag of the condensate droplets has a minor effect on performance. However, others (Grazzini *et al.*, 2015) have stated that the presence of these liquid droplets would reduce the effectiveness

of momentum transfer from the motive to the suction stream, making the net effect of flow condensation unclear.

One simple approach to promote the formation of these liquid droplets is to adjust the degree of superheat at the motive nozzle inlet (see discussion in Section 4.1), as is done in this chapter. A full ejector-based chiller was fabricated and operated for this specific purpose, and results from experiments are presented here while operating with wet R134a and dry R245fa fluids. Analytical and CFD models are formulated to determine the nature of condensed flow inside the motive nozzle and mixing sections to provide an explanation for the observed changes in COP with changes in motive nozzle inlet superheat.

## **5.2 Experimental Approach**

The ejector-based chiller system used is shown schematically in Fig. 4.2 with the locations of temperature, pressure, and mass flow rate measurements indicated. A photograph of the test facility is provided in Fig. 5.1. Details on the test facility can be found in Section 4.2.1.

Two new ejectors, one for R134a and one for R245fa, were designed with conventional circular cross-sections using basic gas dynamics principles and best practices set forth by the ASHRAE equipment handbook for steam-jet refrigeration equipment (ASHRAE, 1983). The motive nozzle was sized for a nominal motive mass flow rate of  $\sim 0.85$  and  $\sim 0.48$  kg min<sup>-1</sup> for R134a and R245fa, respectively, corresponding to a heat input at the boiler of  $\sim 2000$ - $3000$  W and  $\sim 1800$ - $2000$  W, respectively. The mixing section was sized to allow enough suction flow entrainment to realize  $\sim 300$ - $400$  W of cooling at the evaporator, resulting in a COP between 0.1 and 0.2. Schematics of the ejector geometries are provided in Fig. 5.2, showing the dimensions of the motive and suction nozzles, mixing sections, and diffuser sections for both. The ejectors were fabricated in four separate parts



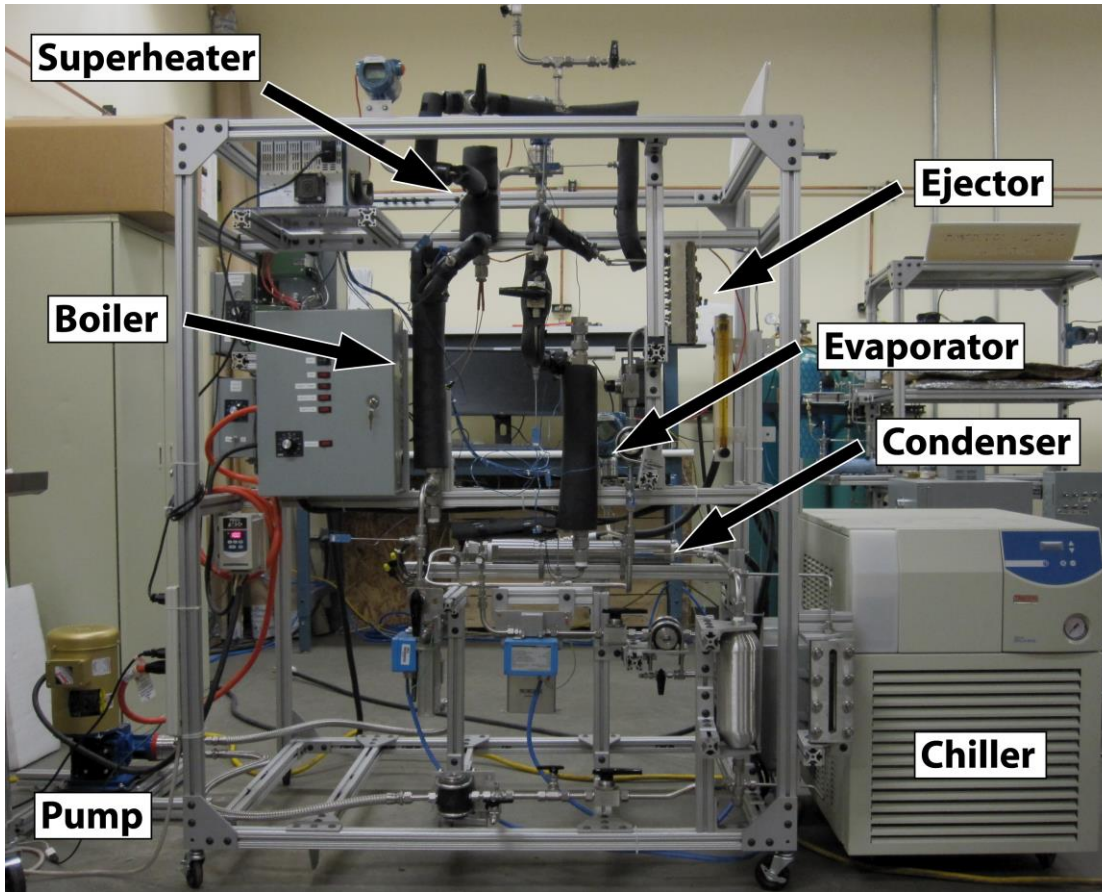


**Figure 5.1: Photograph of ejector-based chiller test facility with major components labeled.**

from aluminum, using a wire EDM to cut converging and diverging angles in the motive and diffuser sections.

To observe operation under wet and dry conditions, the heat input to the boiler was changed to vary the superheat at the motive nozzle inlet while maintaining all other parameters constant. For R134a, the critical mass flow rate of  $0.85 \text{ kg min}^{-1}$  was kept constant to ensure choked flow in the motive nozzle. The evaporator pressure was maintained at 469 kPa with  $T_{\text{sat}} = 14^\circ\text{C}$  and 10 K superheat at the evaporator outlet to ensure superheated conditions at the suction nozzle inlet. The condenser pressure was maintained at 765 kPa with  $T_{\text{sat}} = 30^\circ\text{C}$  and 4 K subcooling at the condenser outlet, ensuring choked suction flow for on-design operation. The temperature lift for all conditions was 16

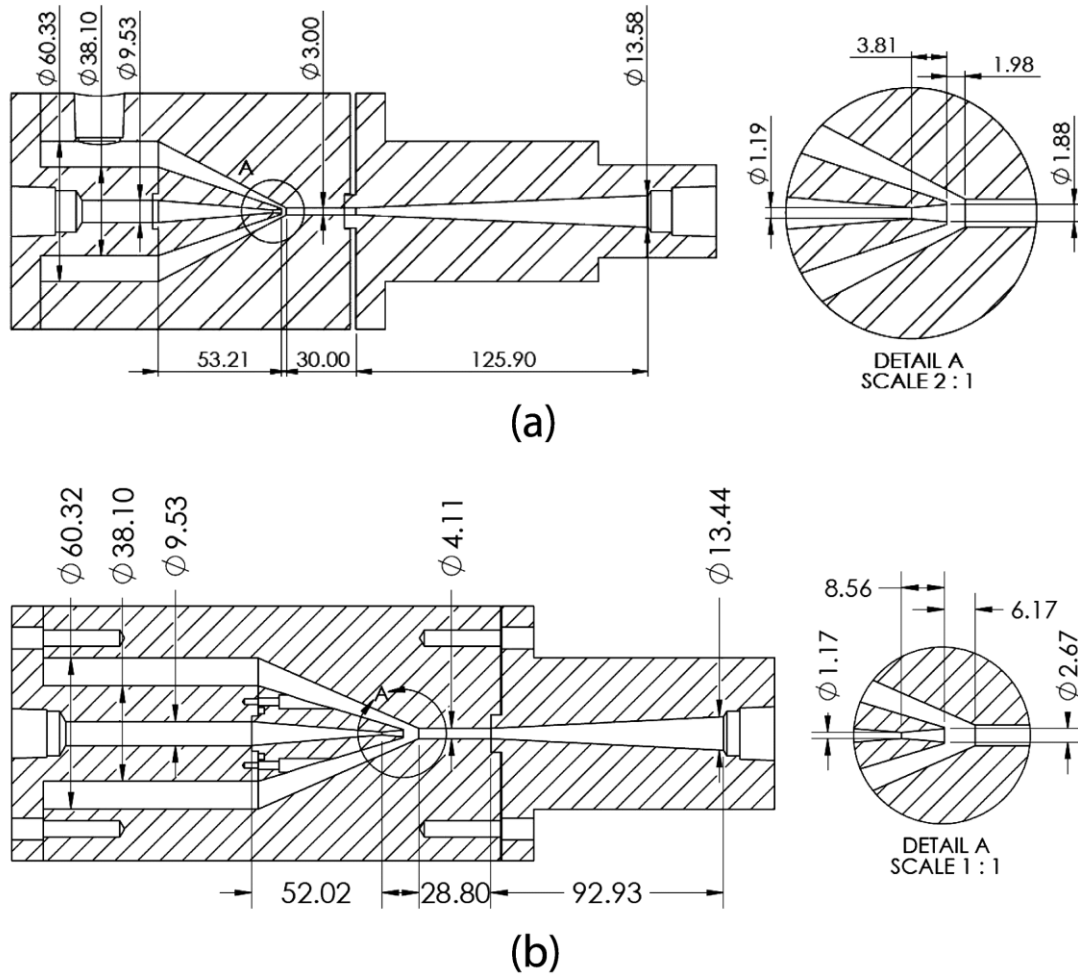


**Figure 5.2: Schematic of ejector geometry used for experiments with (a) R134a and (b) R245fa. All dimensions are in mm.**

K, and system COP varied depending on the change in waste heat input at the boiler and performance of the ejector. For R245fa at the critical mass flow rate of  $0.48 \text{ kg min}^{-1}$ , the evaporator pressure was 90 kPa with  $T_{\text{sat}} = 12^\circ\text{C}$  and 11 K superheat at the evaporator outlet, the condenser pressure was maintained at 214 kPa with  $T_{\text{sat}} = 35^\circ\text{C}$  and 2 K subcooling at the condenser outlet, and the temperature lift for all conditions was 23 K. These operating conditions were also chosen to ensure on-design operation with choked suction flow.

The heat input from the boiler was decreased incrementally until a significant drop in COP was observed. During these experiments, the boiler pressure dropped from 3103 to 2682 kPa with corresponding  $T_{\text{sat}}$  from ranging from 88 to 81°C for R134a, and from 1613 to 1372 kPa with corresponding  $T_{\text{sat}}$  from ranging from 111 to 104°C for R245fa. The measured state points at the motive inlet, suction inlet, and ejector outlet are all plotted on  $T$ - $h$  diagrams in Fig. 5.3 and also shown in Tables 5.1 and 5.2, along with the motive nozzle outlet condition (as approximated by the equilibrium flow model detailed in Section 5.3.1.2). For R134a, motive inlet conditions well outside the vapor-liquid dome to well inside the dome were achieved with a transition from dry to wet jet conditions at the motive nozzle outlet. For R245fa, these conditions also produced a motive inlet condition well outside the vapor-liquid dome to well inside the dome, but wet jet conditions at the motive nozzle outlet were only realized at the lowest motive inlet condition.

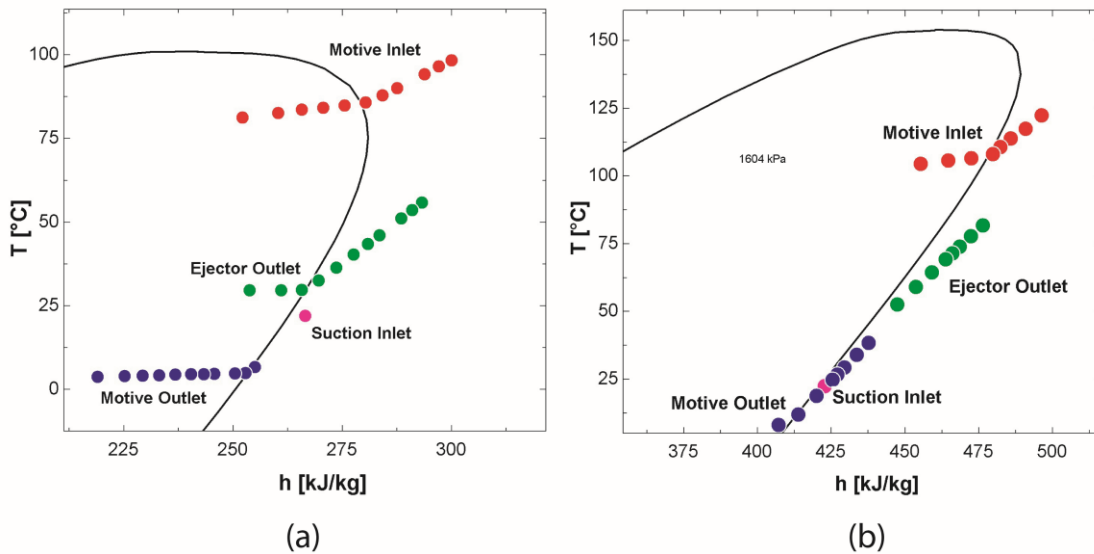


**Figure 5.3:** Experimental state points for (a) R134a and (b) R245fa plotted on a  $T$ - $h$  diagram. Red, blue, green, and pink points indicate the locus of states for the motive nozzle inlet, motive nozzle outlet, ejector outlet, and suction inlet states, respectively. The test matrix starts with right-most points at the highest motive inlet enthalpy and superheat. All ejector outlet conditions are maintained at the same pressure.

**Table 5.1: Tabulated experimental results for ejector-based chiller operation with R134a for different degrees of superheat at the motive nozzle inlet. Change in COP and realized cooling load can be seen to change with the degree of superheat, with the peak value of COP being 0.153. COP values are presented graphically at the top of Fig. 5.5.**

Superheat [K]	$P_{\text{boiler}}$ [kPa] ( $\pm 6$ kPa)	$T_{\text{sat, boiler}}$ [C] ( $\pm 0.25^\circ\text{C}$ )	$T_{\text{m, inlet}}$ [C] ( $\pm 0.25^\circ\text{C}$ ) (State 1 in Fig. 1.5 (a))	$h_{\text{m, inlet}}$ [kJ kg <sup>-1</sup> ]	COP	$Q_{\text{evaporator}}$ [W] ( $\pm 15$ W) ( $T_{\text{cooling}} = 14^\circ\text{C}$ )
10.6	3104	87.8	98.4	300.0	0.137 $\pm$ 0.005	398.2
8.9	3097	87.7	96.6	297.1	0.139 $\pm$ 0.005	398.5
7.1	3062	87.2	94.2	293.8	0.127 $\pm$ 0.005	357.9
3.8	3014	86.4	90.1	287.5	0.128 $\pm$ 0.006	349.5
2.2	2979	85.8	88.0	284.2	0.127 $\pm$ 0.006	339.7
sat. vapor	2936	85.1	85.8	280.3	0.129 $\pm$ 0.006	337.6
sat. ( $x=0.96$ )	2893	84.4	85.0	275.5	0.150 $\pm$ 0.006	381.1
sat. ( $x=0.91$ )	2852	83.7	84.3	270.6	0.153 $\pm$ 0.006	381.1
sat. ( $x=0.86$ )	2814	83.1	83.7	265.7	0.151 $\pm$ 0.006	365.0
sat. ( $x=0.80$ )	2757	82.1	82.7	260.3	0.142 $\pm$ 0.006	332.8
sat. ( $x=0.73$ )	2681	80.8	81.3	252.1	0.113 $\pm$ 0.007	252.2

### 5.3 Analytical Modeling

To explain the COP trends seen in the data, models are formulated to probe the behavior of the ejector flow under varying motive inlet conditions. The behavior of flow in the motive nozzle under different two-phase conditions must first be understood. Section 5.3.1 details the analytical models used to determine the outlet conditions of the motive nozzle. These conditions are then used in the control volume analysis in Section 5.3.2 to calculate values of exergy destruction, motive jet work and heat transfer, MER, and quality that are important to determining the effects of fluid choice and two-phase flow on ejector-based chiller operation.

#### 5.3.1 Motive Nozzle Analysis

The flow phenomena inside the motive nozzle are governed by the combined effects of short time scales for the expansion process, kinetics of droplet formation or evaporation, supersonic speeds, and/or droplet coalescence and impingement. Previous efforts to

**Table 5.2: Tabulated experimental results for ejector-based chiller operation with R245fa for different degrees of superheat at the motive nozzle inlet. Change in COP and realized cooling load can be seen to change with the degree of superheat, with the peak value of COP being 0.160. COP values are presented graphically at the bottom of Fig. 5.5.**

Superheat [K]	$P_{\text{boiler}}$ [kPa] ( $\pm 6$ kPa)	$T_{\text{sat, boiler}}$ [C] ( $\pm 0.25^\circ\text{C}$ )	$T_{\text{m, inlet}}$ [C] ( $\pm 0.25^\circ\text{C}$ ) (State 1 in Fig. 1.5 (a))	$h_{\text{m, inlet}}$ [kJ kg <sup>-1</sup> ]	COP	$Q_{\text{evaporator}}$ [W] ( $\pm 15$ W) ( $T_{\text{cooling}} = 12^\circ\text{C}$ )
11.6	1604	110.9	122.5	496.4	0.141 $\pm$ 0.007	327.7
8.4	1546	109.1	117.5	490.9	0.143 $\pm$ 0.007	322.3
4.6	1550	109.3	113.9	485.9	0.146 $\pm$ 0.007	323.1
2.6	1517	108.2	110.8	482.4	0.154 $\pm$ 0.007	328.6
1.3	1475	106.9	108.2	479.8	0.156 $\pm$ 0.007	321.9
sat. ( $x=0.96$ )	1429	105.4	106.6	472.5	0.160 $\pm$ 0.008	321.0
sat. ( $x=0.91$ )	1415	105.0	105.8	464.7	0.152 $\pm$ 0.008	294.7
sat. ( $x=0.84$ )	1375	103.6	104.5	455.3	0.120 $\pm$ 0.008	222.7

understand such flows have been heavily dependent on empirical correlations based on data for humid air or steam flows. As such, there are no specific models available for R134a, R245fa, or other refrigerants of interest in ejector-based chillers. To address this problem, a model is developed to interpret the two-phase characteristics in the motive nozzle.

The characteristics along the motive nozzle axis are determined using a combination of two different methods that both assume 1D isentropic flow, where all wall boundary layer and heat loss effects are neglected. The first is the “frozen flow” model that treats the flow as an ideal gas with no condensation. Constant specific heats are assumed, approximated as the values at the motive nozzle inlet at the conventional condition. The second is the “equilibrium flow” model that assumes full thermodynamic equilibrium using the Tillner-Roth and Baehr (1994), and Lemmon and Span (2006) equations of state for R134a and R245fa, respectively. With this model, the flow is still modeled as dry, i.e., there is no mechanical coupling to liquid droplets that may form. But the bulk flow still

exhibits properties that are thermodynamically coupled to the formation of droplets. The final flow through the nozzle is a combination of these two models, where the frozen flow assumption is made up to the point where a condensation shock appears. After the shock, the flow is assumed to follow the equilibrium model. The criterion for transition from one model to the other is discussed below.

The motive nozzles of the ejectors under consideration are converging-diverging nozzles. For the purposes of the analytical 1D frozen and equilibrium flow models, the motive nozzle is discretized axially into  $< 0.9$  mm segments at which temperature, pressure, and density are evaluated along the nozzle flow axis (200 and 10 equal segments for the convergent and divergent sections, respectively). The inlet conditions for the models match the experimental conditions given in Tables 5.1 and 5.2 at the motive nozzle inlet. For cases where the motive inlet is saturated, an energy balance on the boiler is used to determine motive inlet enthalpy.

### **5.3.1.1 Frozen Flow Model**

The characteristic assumption of this model is that the superheated vapor entering the motive nozzle inlet behaves as an ideal gas, and this ideal gas behavior is maintained throughout the nozzle as the flow expands. At each discretized location along the motive nozzle axis, the isentropic flow assumption, as well as conservation of mass and energy are satisfied.

$$s = s_{inlet} \quad (5.2)$$

$$\dot{m} = \rho A_c V \quad (5.3)$$

$$h + \frac{1}{2}V^2 = h_{inlet} + \frac{1}{2}V_{inlet}^2 \quad (5.4)$$

For closure, an equation of state is needed to find density. Because the assumption made here is that the superheated refrigerant acts as an ideal gas, the final equation needed is the ideal gas equation of state. These equations are simplified further to form the basic relations for flow of an ideal gas with constant specific heats through an isentropic nozzle. The specific heat ratio,  $\gamma$ , is assumed to be at a constant value, and is evaluated as the ratio of specific heats at the motive nozzle inlet at the ~10 K superheat condition. The speed of sound,  $a$ , is found from  $a = \sqrt{\gamma RT}$ .

### **5.3.1.2 Equilibrium Flow Model**

The equilibrium flow model is similar to the frozen flow model in that it uses Equations 5.2-5.4 for conservation of mass and energy, and assumes isentropic flow. The major difference lies in the fourth equation. When assuming equilibrium flow, ideal gas behavior can no longer be assumed as phase change and non-ideal effects associated with the real gas properties of R134a and R245fa are expected. Therefore, density (and corresponding temperature and pressure) is found from the Tillner-Roth and Baehr (1994) equation of state for R134a and the Lemmon and Span (2006) equation of state for R245fa. The speed of sound is also taken from the appropriate EOS for superheated conditions, but for conditions where the flow is saturated, the formulation by Liu and Groll (2008) is used. This ensures that the calculated state from this model demonstrates the full thermodynamic equilibrium where, if the flow state is inside the saturation dome, the quality of the refrigerant reflects the maximum possible amount of condensation that can occur without any allowances for metastable effects related to flow kinetics.

To determine when the nozzle flow will switch from frozen flow behavior to equilibrium flow behavior, the location of the condensation shock must be determined. It is assumed that losses across the condensation shock are minimal, and need not be reflected in the equilibrium flow model for the purposes of this idealized analysis. As found in previous work by Grazzini *et al.* (2011) and Carey (2008), the onset of homogeneous droplet nucleation is attributed to a certain critical value of nucleation rate that is found to be approximately of the same order of magnitude across fluids and conditions. Carey cites this value as  $10^6 \text{ m}^{-3} \text{ s}^{-1}$ , whereas Grazzini *et al.* state that a sudden rise in nucleation rate marks the onset of condensation. In the present work, the transition is assumed to occur when the state of flow inside the nozzle, as predicted by the frozen flow model, passes the Wilson line. For flows of clean dry steam, this transition occurs at a quality,  $x$ , of approximately 0.955 (Korpela, 2011). Assuming similar behavior for the flow of clean dry refrigerant flow, the condensation shock is assumed to occur at the point at which the frozen flow model predicts  $x = 0.955$ . Quality is calculated using the temperature predicted by the frozen flow model, assuming it is a stronger function of temperature than of pressure. While using this transition value of quality is a major assumption, the ultimate purpose of this study is to determine the outlet condition of the nozzle, not necessarily the precise location of the condensation shock. As shown in the results, the location of the condensation shock was far enough upstream of the motive nozzle exit, or completely absent, such that small changes in the position of the condensation shock would not change the ultimate conditions at the motive nozzle outlet.



### **5.3.1.3 Motive Nozzle Numerical Model**

To assess the performance of readily available computational platforms and formulations, 2D simulations of flow through motive nozzles of the same geometry are performed and compared with the two 1D models above. Using the computational package ANSYS FLUENT v13 (2010), all calculations are set to be performed in the vapor phase using real gas properties for R134a and R245fa, omitting any droplet flow mechanics coupling and only including thermodynamic coupling. Using the  $k$ - $\varepsilon$  RNG turbulence model with enhanced wall functions and a second order upwind discretization, centerline profiles for temperature, pressure, and density are determined.

### **5.3.2 Control Volume Analysis**

As will be demonstrated in Section 5.4 and observed in Chapter 4, the equilibrium flow model provides the most accurate prediction of flow properties at the motive nozzle outlet. With this information, the control volume analysis can proceed and probe the behavior of the ejector flow under varying motive inlet conditions. Basic energy and entropy balances are used for two different control volumes to differentiate between various quantities that may affect ejector performance and the resulting system COP. Each balance uses values of temperature, pressure, and mass flow rate that are directly measured at the ejector inlets and outlet during experimental operation. While this model is relatively simple, it allows for an assessment of conditions inside the ejector mixing section to determine the roles of fluid properties and two-phase flow on ejector operational characteristics.

The two control volumes (CVs) used for the analysis are shown in Fig. 5.4. Control volume (a) includes the entire ejector, using inlet temperature, pressure, and mass flow rate values measured directly during experiments. This CV allows for the calculation of ejector

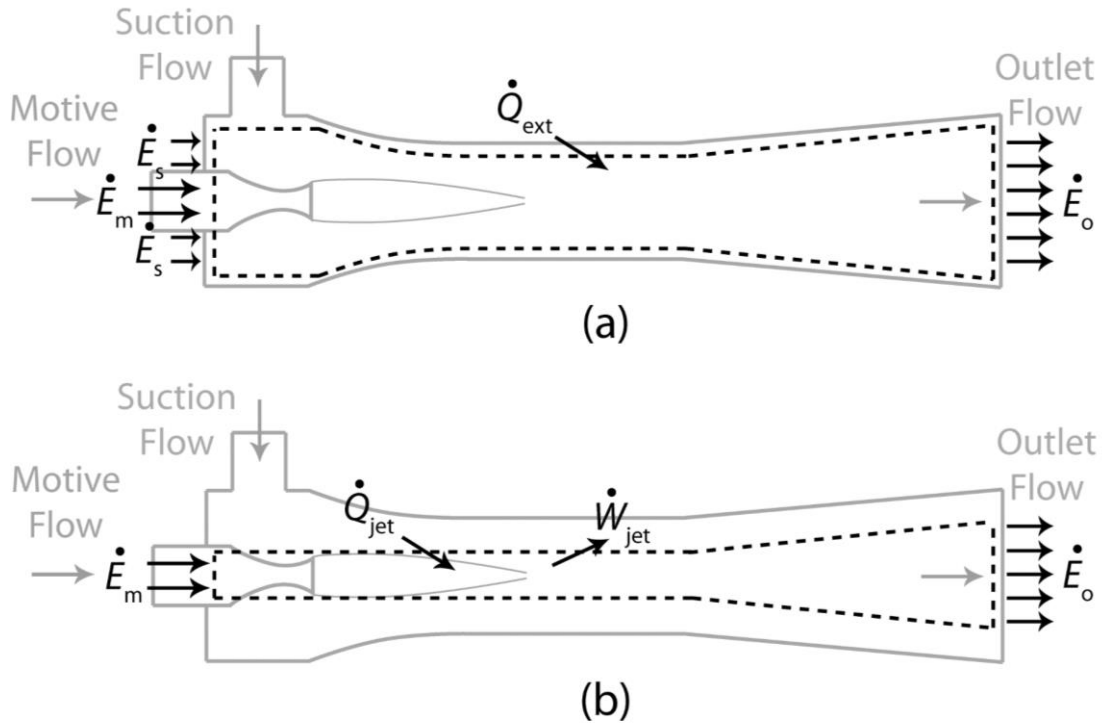


**Figure 5.4: (a) CV of whole ejector, (b) CV of motive jet flow only with zero mass flux boundary.**

outlet conditions as well as overall ejector exergy destruction. Control volume (b) is of the motive flow only from the motive nozzle inlet to the ejector outlet. The boundary of this control volume is specifically chosen as a boundary of zero mass flux. In practice, this boundary can be traced by following the streamline of flow exiting the very edge of the motive nozzle outlet, known in the literature as the dividing streamline (DSL). This CV allows for the calculation of work done by the motive jet on the suction flow,  $\dot{W}_{jet}$ , and heat transferred from the suction flow to the motive flow,  $\dot{Q}_{jet}$ . In this manner, the total energy available in the motive jet can be allocated to either beneficial suction entrainment effects ( $\dot{W}_{jet}$ ) or parasitic heat transfer effects ( $\dot{Q}_{jet}$ ).

### 5.3.2.1 Total Exergy Destruction

To determine the total exergy destroyed by the ejector, the control volume in Fig. 5.4 (a) is used with the following energy and entropy balances:

$$\dot{Q}_{ext} = \dot{m}_o \left( h_o + \frac{1}{2} V_o^2 \right) - \dot{m}_m \left( h_m + \frac{1}{2} V_m^2 \right) - \dot{m}_s \left( h_s + \frac{1}{2} V_s^2 \right) \quad (5.5)$$

$$\dot{S}_{gen} = \dot{m}_o s_o - \dot{m}_m s_m - \dot{m}_s s_s + \frac{\dot{Q}_{ext}}{T_K} \quad (5.6)$$

The subscripts  $o$ ,  $m$ , and  $s$  indicate properties at the ejector outlet, motive inlet, and suction inlet, as shown in Fig. 5.4 (a).  $\dot{Q}_{ext}$  is the heat exchanged with the ambient, where a negative value indicates that heat is lost to the surroundings.  $\dot{Q}_{ext}$  is approximated as the sum of convection and radiation heat transfer between the ejector surface and the surroundings. For all test conditions, the value of  $\dot{Q}_{ext}$  was low: < 6 W of heat loss for R134a and < 12 W of heat loss for R245fa. With the values of  $\dot{Q}_{ext}$  known,  $h_o$  was calculated using Equation 5.5.

Knowing all inlet and outlet conditions as well as the heat lost from the ejector, the total exergy destroyed by the ejector is determined from Equation 5.6 using  $\dot{X}_{destroyed} = \dot{S}_{gen} T_K$  with the boundary temperature,  $T_K$ , as  $\text{avg}(\text{avg}(T_s, T_o), T_{\text{ambient}})$ . The overall exergy destruction is not heavily dependent on the value of  $T_K$ . In the discussion below, these values of total exergy destruction are normalized by the total motive inlet energy available to drive the ejector,  $\dot{m}_m h_m$ . These values of normalized exergy destruction are a measure of irreversibilities inside the ejector, the sources of which are heat transfer

across a temperature difference ( $\dot{Q}_{jet}, \dot{Q}_{ext}$ ), turbulent mixing at the jet boundary, viscous dissipation, wall friction, and shocks.

### 5.3.2.2 Motive Jet Work and Heat Transfer

The use of the control volume in Fig. 5.4 (b) allows for the quantification of two values important for ejector operation, namely the work done by the motive jet on the suction flow to realize suction flow entrainment,  $\dot{W}_{jet}$ , and the heat transfer from the suction flow to the motive flow,  $\dot{Q}_{jet}$ . In this manner, the effect of changing motive jet inlet conditions can be quantified to help describe fluid flow properties that affect COP.

The total energy transferred to the suction flow,  $\dot{E}_{total}$ , is calculated using Equation 5.7 with an energy balance on the control volume.

$$\dot{E}_{total} = \dot{Q}_{jet} - \dot{W}_{jet} = \dot{m}_m \left( h_o + \frac{1}{2} V_o^2 \right) - \dot{m}_m \left( h_m + \frac{1}{2} V_m^2 \right) \quad (5.7)$$

It is assumed that the flow exiting the diffuser is fully developed such that the properties at the outlet are considered the same for both the  $\dot{m}_m$  and the  $\dot{m}_s$  portions of the exiting flow.

A positive value of  $\dot{Q}_{jet}$  indicates that heat is transferred from the suction flow to the motive flow, and a positive value of  $\dot{W}_{jet}$  indicates that work is done by the motive jet on the suction flow (i.e., suction flow entrainment occurs). To determine the portions of  $\dot{E}_{total}$  that contribute to entrainment and to heat transfer, the heat transfer portion can be approximated using the Strong Reynolds Analogy appropriate for turbulent boundary

layers (Grazzini *et al.*, 2015). For moderate temperature variations, the turbulent Prandtl number can be taken as 0.77, and used to approximate heat transfer across the jet boundary.

$$\dot{Q}_{jet} = \frac{\mu c_p}{Pr} \frac{\partial T}{\partial y} A_{s,jet} = \frac{c_p}{Pr} \frac{\partial T}{\partial y} \frac{\partial y}{\partial u} \tau A_{s,jet} \approx \frac{c_p}{0.77} \frac{(T_s - T_m)}{(V_m - V_s)} \tau A_{s,jet} \quad (5.8)$$

where  $A_{s,jet}$  is the surface area of the jet, calculated assuming the jet is cylindrical with a diameter 25% larger than the motive nozzle exit diameter (as was observed in the 2D numerical models).  $\tau$  is the shear stress on the dividing streamline (DSL), or jet boundary, and found using the empirical relation of Papamoschou and Roshko (1988):

$$\tau = K \frac{1}{2} (\rho_m + \rho_s) (V_m - V_s)^2 \left[ \frac{(1+\eta)(1+r)}{2(1+r\eta)} \right] f(M_c) \quad (5.9)$$

$$\begin{aligned} \eta &= \sqrt{\rho_s / \rho_m} \\ r &= V_s / V_m \\ f(M_c) &\approx 0.25 + 0.75e^{-3M_c^2} \\ M_c &= \frac{V_m - V_s}{a_m + a_s} \end{aligned} \quad (5.10)$$

Here,  $K$  is an empirical constant found to be 0.013 by Wygnanski and Fiedler (1970). The values used for  $c_p$ ,  $T$ ,  $V$ , and  $\rho$  in Equations 5.8-5.10 are taken as the average values between the motive nozzle outlet (as calculated by the equilibrium flow model in Section 5.3.1.2) and the ejector outlet for motive properties, and suction nozzle outlet and ejector outlet for suction properties. For the cases where two-phase flow is present,  $c_p$  cannot be defined, and is therefore approximated at a value calculated at conditions near saturation.  $a$ , the

speed of sound, is calculated from  $\rho$  and  $T$  using a relation developed by Liu and Groll (2008) for the speed of sound of a two-phase flow.

The validity of using average properties for  $T$ ,  $V$ , and  $\rho$  must be checked, because values change significantly along the length of the ejector. For this validation, a CFD simulation of the ejector flow, much like that from Section 4.3.2, was considered for the 10.6 K superheated case for R134a. In this case, the temperature and velocity differences between the motive and suction flows are the most extreme, making it an ideal case for validation because  $\dot{Q}_{jet}$  would be at its highest value. Values for  $T$ ,  $V$ , and  $\rho$  were tabulated along the length of the ejector for the ejector centerline (for the motive properties), and along a streamline in the fully-developed part of the suction flow (for the suction properties). At each point, heat transfer at that segment was calculated using Equations 5.8-5.10, and integrated over the entire length of the mixing section and diffuser sections. Using this method,  $\dot{Q}_{jet}$  was found to be 51 W, whereas using overall averaged properties for the same flow predicted  $\dot{Q}_{jet}$  to be 57 W. Therefore, overall averaging of properties from the motive or suction nozzle outlet to ejector outlet was deemed to be acceptable.

Once  $\dot{Q}_{jet}$  is approximated using the above analysis,  $\dot{W}_{jet}$  is found using Equation 5.7. In the discussion below, the value of  $\dot{W}_{jet}$  is normalized with respect to the total energy needed to drive the suction flow at maximum ejector operating conditions ( $MER_{max}$ , as defined in the next section) with  $\dot{m}_{s,max}(h_o - h_s)$ . This trend shows a comparison of the energy available in the motive jet to the energy needed for maximum performance. In the case of R134a, calculated  $\dot{W}_{jet}$  is able to provide  $\sim 1.5$  to  $7.5$  times the work needed to entrain

the suction flow, but in the case of R245fa, entrainment is much more difficult because  $\dot{W}_{jet}$  is only enough to provide ~0.8 to 1.3 times the energy needed.

### 5.3.2.3 Mass Entrainment Ratio

The maximum MER can be attained when there is perfect momentum transfer in the ejector such that the total change in energy in the motive jet is imparted to the suction flow in the form of suction flow entrainment. Such perfect momentum transfer would occur under the conditions of zero  $\dot{Q}_{jet}$ , zero viscous dissipation, and perfectly homogeneous flow. The maximum MER can be calculated as

$$MER_{max} = \frac{h_m - h_o}{h_o - h_s} \quad (5.11)$$

Comparison of the measured MER with this maximum MER is an indication of the effectiveness of momentum transfer inside the ejector. Large differences between the two values are indications that  $\dot{W}_{jet}$  is reduced because some energy is transferred as  $\dot{Q}_{jet}$  instead, and/or the available  $\dot{W}_{jet}$  is not being effectively transferred to the suction flow. Note that not all values of  $MER_{max}$  and MER ratio can be calculated because the value of MER cannot be defined after a certain point for R134a. This is due to the fact that at test conditions of low motive inlet enthalpy, the lower cycle produces a net energy output to the ejector, and the upper cycle has a net energy input from the ejector. In practice, a real MER value can still be measured because the kinetic energy component of the energy in the upper cycle is still greater than zero (as shown with a positive  $\dot{W}_{jet}$ ). This role-reversal

of the ejector is not desirable, and is a function of the fluid used. It does not occur for R245fa at the test conditions considered here.

#### **5.3.2.4 Quality**

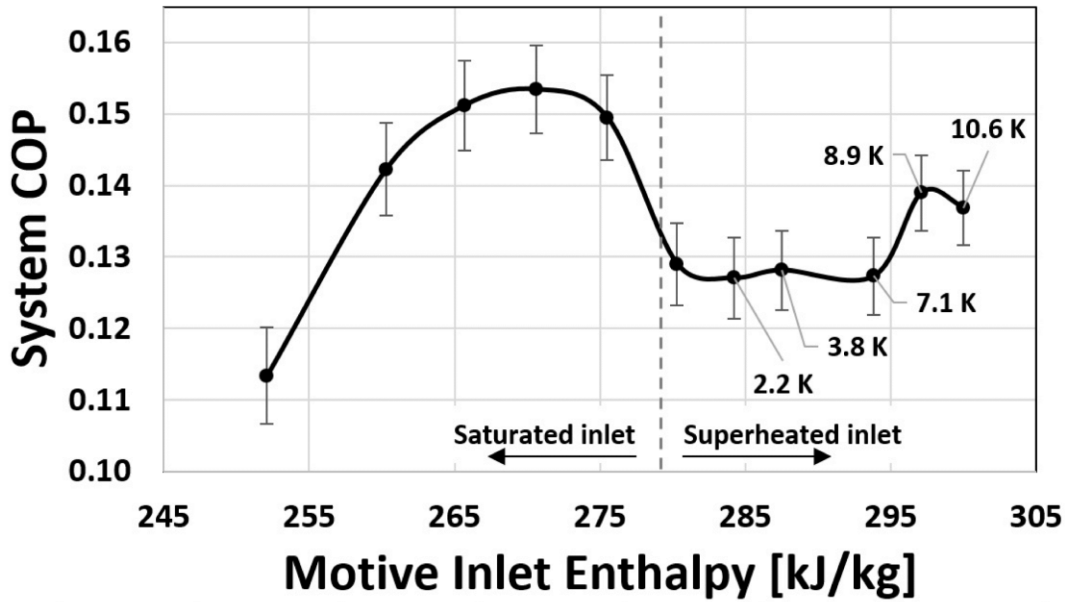
A major focus of this work is to determine the effect of two-phase flow on performance. To assess the onset and magnitude of these effects, qualities are determined assuming equilibrium at the motive nozzle inlet and outlet as well as the ejector outlet. For the wet R134a fluid, condensation in the motive nozzle is seen for higher motive inlet enthalpies with  $x_{m,outlet} < x_{m,inlet}$ . For the dry R245fa fluid, evaporation in the motive nozzle is seen for all conditions with  $x_{m,outlet} > x_{m,inlet}$ .

### **5.4 Results and Discussion**

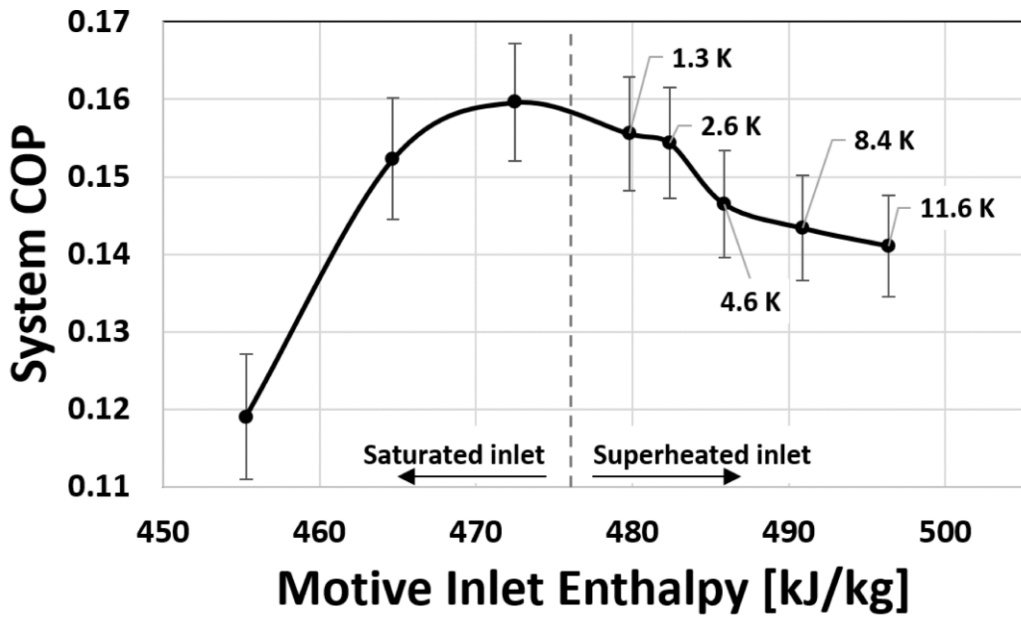
The experimental change in COP observed at different motive inlet conditions (state 1 in Fig. 1.5 (a)) is shown in Fig. 5.5 and in Tables 5.1 and 5.2. Data labels in Fig. 5.5 indicate the degree of superheat at each superheated test condition. For R134a, the maximum superheat tested was 10.6 K, which is considered the “conventional” operational point, yielding a COP of 0.137 at a motive inlet temperature of 98.4°C. As the motive inlet enthalpy is lowered, a drop in COP is seen first with a low of 0.127 at the 2.2 K superheat case. Once the motive inlet condition reaches saturation, the COP rises to a maximum of 0.153 at a motive inlet enthalpy  $\sim 270 \text{ kJ kg}^{-1}$  and temperature of 84.3°C. Below this value of motive inlet enthalpy, performance drops significantly, likely due to off-design operation of the ejector.

For R245fa, a similar trend is seen. The maximum superheat tested was 11.6 K, yielding a COP of 0.141 at a motive inlet temperature of 122.5°C for “conventional” operation. As the motive inlet enthalpy drops, the COP rises steadily to a maximum value





(a)



(b)

**Figure 5.5: Experimental change in COP vs. motive inlet enthalpy for (a) R134a and (b) R245fa. The degree of superheat for each superheated data point is indicated in data labels. System shows peak performance at saturated inlet conditions for both fluids.**

of 0.160 at a motive inlet enthalpy  $\sim 470 \text{ kJ kg}^{-1}$  and temperature of  $106.6^\circ\text{C}$ . Further reduction of enthalpy results in a dramatic drop in COP.

These data show a two-fold increase in performance. First, the COP increases by 12-13% with respect to the most superheated conventional operating condition. Second, the motive inlet temperature is significantly reduced by 14-16 K. This is of great practical importance because the motive inlet temperature is the maximum temperature of the cycle, thus defining the source temperature that can be used to drive the system. Experiments show that by simply forcing a saturated inlet condition at the motive nozzle inlet, not only is the COP increased, but a much lower waste heat temperature can be used, significantly widening the operational envelope of the cycle.

To understand this increase in COP, the idealized motive nozzle analytical models described in Section 5.3.1 were run at the experimental test conditions to determine the properties of the motive nozzle outlet flow when it enters the mixing section and comes into contact with the suction flow to realize entrainment. Then using the control volume analysis in Section 5.3.2, the effect of various parameters on ejector performance can be interpreted. The observed change in COP appears to be a combination of two effects: the choice of working fluid and the effect of phase change on the effectiveness of momentum transfer in the mixing section. The magnitude and nature of these two factors are discussed in the following sections.

#### **5.4.1 Motive Jet Properties**

##### ***5.4.1.1 Comparison of Properties***

Figure 5.6 provides a comparison of flow properties along the length of the motive nozzle in the vicinity of the nozzle throat (throat location being indicated by the vertical dotted line in all figures) according to the 1D analytical frozen and equilibrium flow models, as well as the 2D CFD model from Section 5.3.1. Starting with the upper graphs in Fig. 5.6

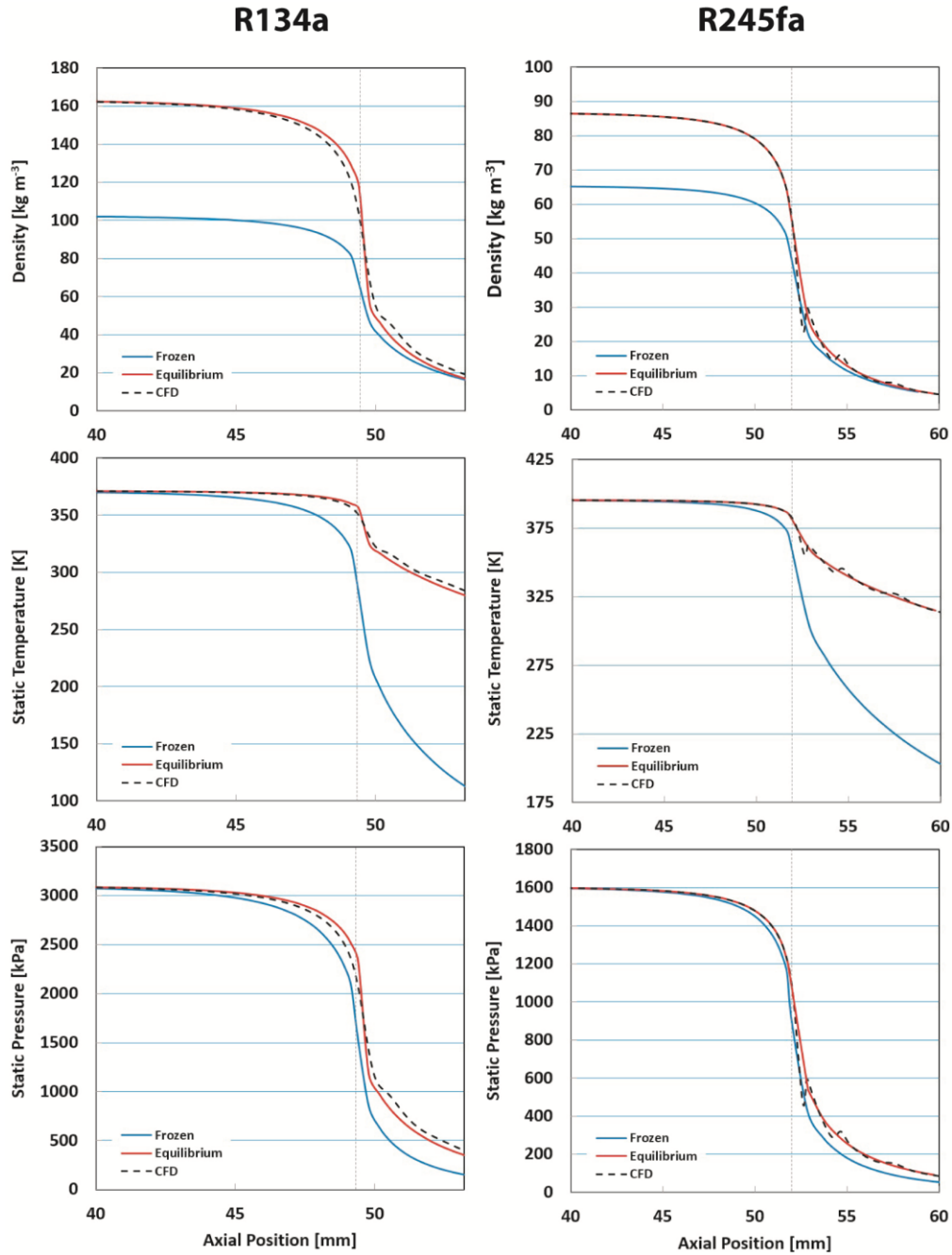


**Figure 5.6: Predicted variation in (top) density, (middle) temperature, and (bottom) pressure for R134a (left) and R245fa (right) near motive nozzle throat for the highest superheat case. Comparison is made between analytical frozen and equilibrium flow models as well as 2D CFD simulation in ANSYS FLUENT.**

comparing density, discrepancies between the models are significant at the motive nozzle inlet, but lesser after the nozzle throat. This discrepancy is due to the strongly non-ideal

behavior of R134a and R245fa gas near the critical point. Whereas the density of the refrigerant gas in the frozen flow case is calculated using the ideal gas law, density in the equilibrium case is taken from the refrigerant equation of state, accounting for non-ideal effects. At the most superheated conventional motive nozzle inlet condition shown in Fig. 5.6, the reduced temperature ( $T/T_{\text{critical}}$ ) and reduced pressure ( $P/P_{\text{critical}}$ ) are 0.99 and 0.76, respectively for R134a, and 0.93 and 0.44, respectively for R245fa. The compressibility  $Z$  factors, calculated as

$$Z = \frac{P}{\rho RT} \quad (5.12)$$

with  $\rho$  taken as the equilibrium value, are 0.63 and 0.75 for R134a and R245fa, respectively, implying significant non-ideal behavior. This is in contrast to a  $Z$  factor of 0.90 and 0.97 at the nozzle outlet for R134a and R245fa, respectively. It should be mentioned that while the density calculated by the frozen flow model is for that of pure vapor, the density for the equilibrium case incorporates that of any liquid that forms at states where  $x < 1$ .

In the middle figures of Fig. 5.6 comparing static temperature, the trend is reversed such that there is excellent agreement at the motive inlet, but drastic disagreement starting near the throat. The main contributor to this is the presence of condensation. In the frozen flow case, pure expansion of the flow draws the temperature of the flow down to extreme low values. However the equilibrium flow model assumes that there is ample time for condensation to occur along with the resulting heat release associated with the formation of liquid droplets. The effect is that the temperature of the flow is maintained at saturation

for the given pressure. Due to this, the temperature for the equilibrium case is significantly higher after the throat.

In the bottom figures of Fig. 5.6 comparing static pressure, a similar trend is seen where discrepancies are low at the motive nozzle inlet and higher at the outlet. The discrepancies are due to the link between temperature and pressure. In the frozen flow case, lower pressures are linked to lower temperatures from the ideal gas equation. Once the flow becomes saturated at the throat in the equilibrium case, the pressure stays at the saturation pressure for the given temperature, which is already elevated above the frozen flow temperature because of the heat addition to the bulk fluid from droplet condensation.

In Fig. 5.6, the prediction of the CFD model is shown in comparison with the results of the frozen and equilibrium models. It is interesting but not surprising to see that the CFD case almost exactly matches the equilibrium case with the exception of a few minor fluctuations. These fluctuations are evidence of 2D flow effects captured in the CFD model, namely oblique expansions emanating from the sharp edges produced by sudden rate of change in cross-sectional area at the motive throat. The 1D formulation of the equilibrium model is unable to capture these effects. Despite this fact, it can be seen that the greatly simplified 1D models are an excellent approximation of the nozzle flow field as defined by the equilibrium model. However, these results also show that caution should be used when applying such CFD models to flow that may experience phase change, as properties will be predicted assuming a thermodynamic equilibrium that may not be present in the real flow. It should be noted that potential improvement in two-phase CFD models is the subject of much current work as it is quite complex. The commonly-available “wet steam” model

in ANSYS FLUENT may be able to predict the real motive nozzle conditions if properly adapted for use with R134a and R245fa, but such development is not yet complete.

#### 5.4.1.2 Effect of Superheat on Motive Flow Wetness

Figure 5.7 shows static pressure profiles along the motive nozzle axis in the vicinity of the nozzle throat. For R134a, the three curves chosen for comparison are from the conventional condition at a 10.6 K superheat, as well as minimum and maximum COP conditions seen at the top of Fig. 5.5. For R245fa, the two chosen for comparison are the conventional condition at 11.6 K superheat, as well as the maximum COP condition seen in Fig. 5.5.

Starting with the R134a curves in Fig. 5.7 (a), the Wilson line condition (Korpela, 2011) dictates that the condensation shock forms at locations increasingly upstream with decreasing superheat, albeit still near the motive nozzle throat. At the saturated condition, there is no condensation shock in the nozzle because  $x$  is already  $< 0.955$  at the inlet of the motive nozzle such that flow along the entire length of the nozzle follows the equilibrium model. Therefore at all flow conditions, the flow exits the motive nozzle closer to its

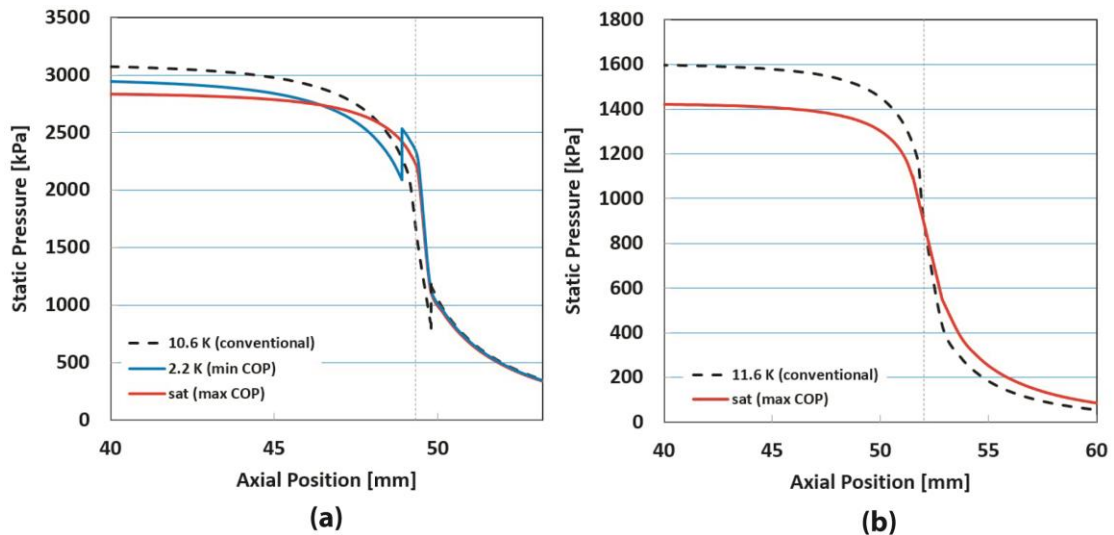


**Figure 5.7: Results from 1D analytical models for (a) R134a and (b) R245fa. Flow conditions transition from frozen flow conditions to equilibrium flow conditions across a condensation shock.**

equilibrium condition, as was observed from the visualization experiments in Chapter 4. As such, flow is still superheated at the exit for the conventional case. The minimum and maximum COP conditions exhibit outlet qualities 0.95 and 0.90, respectively.

For R245fa in Fig. 5.7 (b), the behavior is quite different because of dry fluid properties. In the conventional case, the thermodynamic state of the flow as predicted by the frozen model never enters the dome, and actually becomes more superheated. As a result, conditions inside the nozzle follow the frozen flow model all the way to the nozzle exit. For the maximum COP case, inlet conditions are already significantly saturated ( $x = 0.96$ ) such that the kinetics of droplet formation have already been overcome. Subsequent expansion through the nozzle actually causes the flow to evaporate rather than to condense. This implies that the flow follows the equilibrium case along the entire length of the nozzle. Therefore, no condensation shock forms for R245fa, and both cases show superheated (dry) conditions at the motive nozzle exit.

It should also be noted that the condensation shocks that do occur tend to form close to the nozzle throat where drastic changes in temperature and pressure are present. Such behavior has been noted by others (Berana *et al.*, 2009; Grazzini *et al.*, 2011; Nakagawa *et al.*, 2009) with some discussion related to the stability of the condensing flow. For cases of condensation immediately after the throat, stability is not easily maintained and may cause flow oscillations. Therefore, the flashing R134a flows are all subject to potential flow instabilities and decreased ejector performance.

### 5.4.2 Maximum Jet Power

To evaluate the ability of the motive jet to entrain suction flow and affect system performance, the transfer of jet kinetic energy to the suction flow is considered. The potential of the jet to do so can be evaluated by calculating total jet power, defined as

$$Power_{jet} = \frac{1}{2} \dot{m}_{motive} V^2 \quad (5.13)$$

where  $V$  is taken at the motive nozzle outlet. It is assumed here that the drag force exerted on the droplets will be negligible because of their small size ( $<1 \mu\text{m}$  (Carey, 2008)) such that the value of  $V$  is unaffected by condensation.

An increase in jet power would be the precursor for higher suction flow entrainment. It is expected that an increase in superheat will dry the flow and reduce density, but also accelerate it. Therefore the net effect on total available momentum is unclear. Furthermore, it is unclear how effectively that momentum would be transferred to the suction flow based on the changes in motive jet properties. Tables 5.3 and 5.4 show the values of density, velocity, and pressure at the outlet of the motive nozzle, and resulting power of the motive jet. Again, comparison is made for both the frozen and equilibrium

**Table 5.3: Motive jet properties at outlet of motive nozzle operating with R134a. Density values indicated as ‘wet’ calculated as average of liquid and vapor fractions. Speed of sound for frozen flow model is approximated as  $c=\text{sqrt}(\gamma RT)$ . Starred values are the conditions expected based on the analysis in Section 5.4.1.2.**

Superheat [K]	Model	$\rho$ [kg m <sup>-3</sup> ]	$V$ [m s <sup>-1</sup> ]	$P_{outlet}$ [Pa]	$Power_{jet}$ [W]
10.6 (conventional)	Frozen	16.22 (dry)	328	1.49E+05	794
	Equilibrium*	17.01 (dry)*	300*	3.51E+05*	637*
2.2 (min COP)	Frozen	17.82 (dry)	311	8.67E+04	744
	Equilibrium*	17.85 (wet)*	286*	3.46E+05*	580*
sat ( $x=0.91$ ) (max COP)	Frozen	17.71 (dry)	306	7.25E+04	704
	Equilibrium*	18.63 (wet)*	274*	3.42E+05*	532*



**Table 5.4: Motive jet properties at outlet of motive nozzle operating with R245fa. Density values indicated as ‘wet’ calculated as average of liquid and vapor fractions. Speed of sound for frozen flow model is approximated as  $c=\sqrt{\gamma RT}$ . Starred values are the conditions expected based on the analysis in Section 5.4.1.2.**

Superheat [K]	Model	$\rho$ [kg m <sup>-3</sup> ]	$V$ [m s <sup>-1</sup> ]	$P_{\text{outlet}}$ [Pa]	Power <sub>jet</sub> [W]
11.6 (conventional)	Frozen*	4.00 (dry)*	352*	4.94E+04*	488*
	Equilibrium	4.24 (dry)	343	7.97E+04	479
sat ( $x=0.96$ ) (max COP)	Frozen	3.84 (dry)	338	3.91E+04	415
	Equilibrium*	4.43 (dry)*	324*	7.74E+04*	422*

models at conventional conditions, as well as maximum and minimum COP conditions where applicable. Note that the frozen flow results are for completely dry flow such that the reported density is for pure gaseous flow. The equilibrium flow density is a mass-averaged density value, and includes the condensate. The actual power of the jet at a given condition will lie between the frozen and equilibrium model predictions.

Tables 5.3 and 5.4 show that at all conditions for both fluids, the equilibrium flow model predicts a lower or nearly equal jet power in comparison to the frozen flow model. This suggests that the presence of liquid droplets has a notable detrimental impact on the total energy available to entrain suction flow, with the effect being less notable for R245fa. As superheat decreases, jet power drops for both the frozen and equilibrium models.

This jet power indicates a maximum total energy available for transfer to the suction flow, but does not characterize the amount transferred to realize entrainment. The effectiveness of momentum transfer also changes based on jet properties. Grazzini *et al.* (2015) formulate a model of the compressible turbulent mixing layer between the motive and suction streams and provide insights into factors most important for improving mixing rate for suction flow entrainment. It is found that having an average suction flow density higher than the average motive flow density aids in flow entrainment. Furthermore, a

greater velocity mismatch between the motive and suction helps as well. This implies that a dry motive jet would be more beneficial for not only momentum transfer effectiveness, but also for producing maximum total momentum available for transfer.

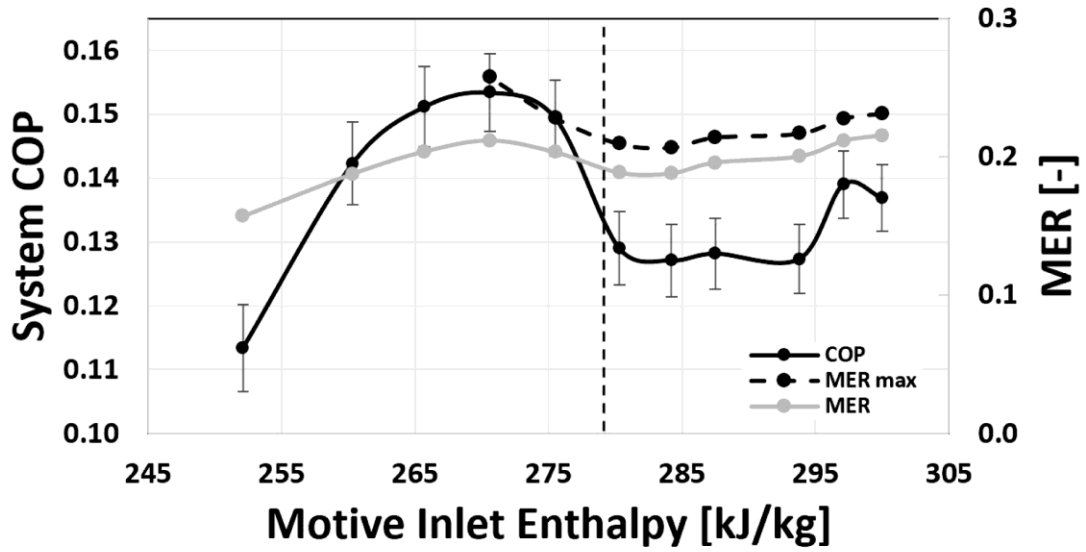
Even though it is not possible with the present analysis to determine exactly where in the range of predicted  $T$ ,  $P$ , and  $\rho$  values (from the frozen and equilibrium models) the real nozzle outlet condition lies, the analysis in Section 5.4.1 and visual observations from Chapter 4 suggest that the flow more likely resembles the conditions of the equilibrium model, except for the conventional R245fa case. If this is true, the ejector will perform the same or worse than if the flow had maintained frozen behavior. Despite this, Fig. 5.5 shows an increase in COP as the motive inlet enthalpy is decreased and equilibrium conditions are more likely to exist at the exit of the motive nozzle. Similarly, Tables 5.3 and 5.4 show a decrease in jet power with lowering motive inlet condition, and maxima or minima in COP do not correspond to maxima or minima of jet power. Therefore, this jet power analysis is limited in its ability to fully predict the behavior of the ejector and chiller system, especially when operating with R134a. To improve this analysis, the results from control volume analysis developed in Section 5.3.2 are discussed below.

#### **5.4.3 Effect of Fluid Type**

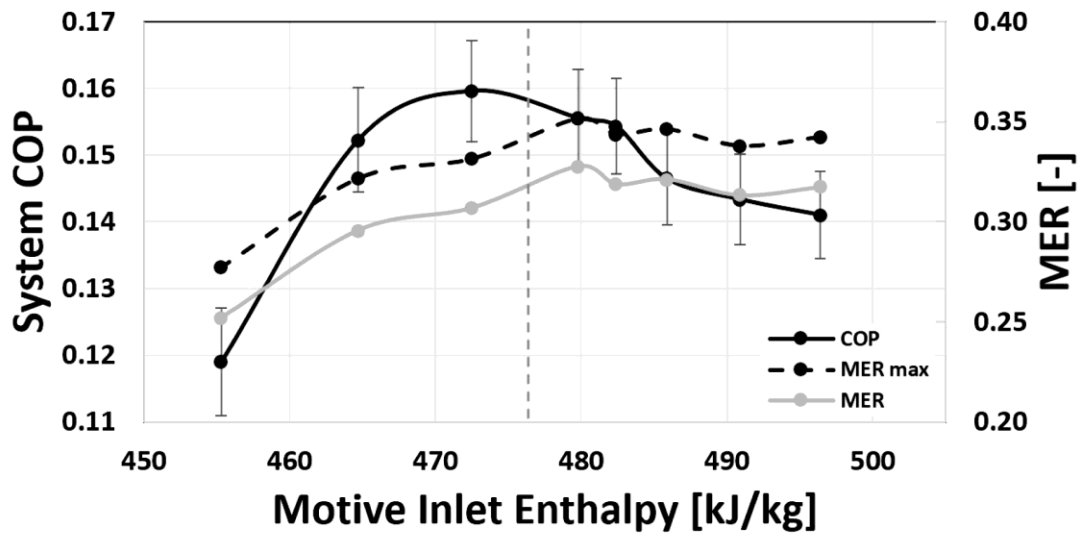
The theoretical maximum performance of the ejector is largely a factor of the fluid used. Differing shapes of the saturation domes for the wet R134a and the dry R245fa fluids define the total energy that can be extracted from the upper cycle, and energy needed to drive the compression process in the lower cycle. The functionality of the ejector can be subdivided into two parts: the behavior as a turbine, or work extraction device for the upper cycle, and behavior as a compressor to achieve cooling in the lower cycle. Looking at Equation 5.11

for  $MER_{max}$ , the numerator is the change in enthalpy across the turbine, while the denominator is the change in enthalpy across the compressor. In the case where the change in enthalpy between the motive inlet and ejector outlet is high, more work can be extracted to power the lower cycle, and similarly, when the enthalpy change between the ejector outlet and suction inlet is small, less work is needed to power the lower cycle. Both of these properties are beneficial for a high MER and related COP values. In Fig. 5.8, plots of  $MER_{max}$  show the best possible performance, given the properties of R134a and R245fa at the boiler, condenser, and evaporator pressures chosen for the test matrix. Because of the specific shape of the saturation dome for each of the fluids, R134a exhibits a slight drop in maximum performance at superheated motive inlet conditions near saturation. But after the motive inlet saturation condition is reached, there is a notable increase in maximum MER. This is due to the fact that the work needed to drive the lower cycle is significantly reduced, and the work available from the upper cycle allows for higher entrainment. But after this maximum in  $MER_{max}$ , the role-reversal occurs (as discussed in Section 5.3.2.3), and net negative energy output by the ejector in the upper cycle makes it impossible to properly define  $MER_{max}$ .

In Fig. 5.9 (a) for R134a, the difference between  $MER_{max}$  and measured MER increases gradually with decreasing motive inlet enthalpy, and then starts to increase dramatically after motive inlet saturation. In Fig. 5.9 (b) for R245fa, this difference is constant for superheated motive inlet enthalpies. Near saturated inlet enthalpies there is a small spike before the difference also increases at a constant rate with deeper saturation. This behavior suggests an optimum in momentum transfer efficiency at slightly



(a)

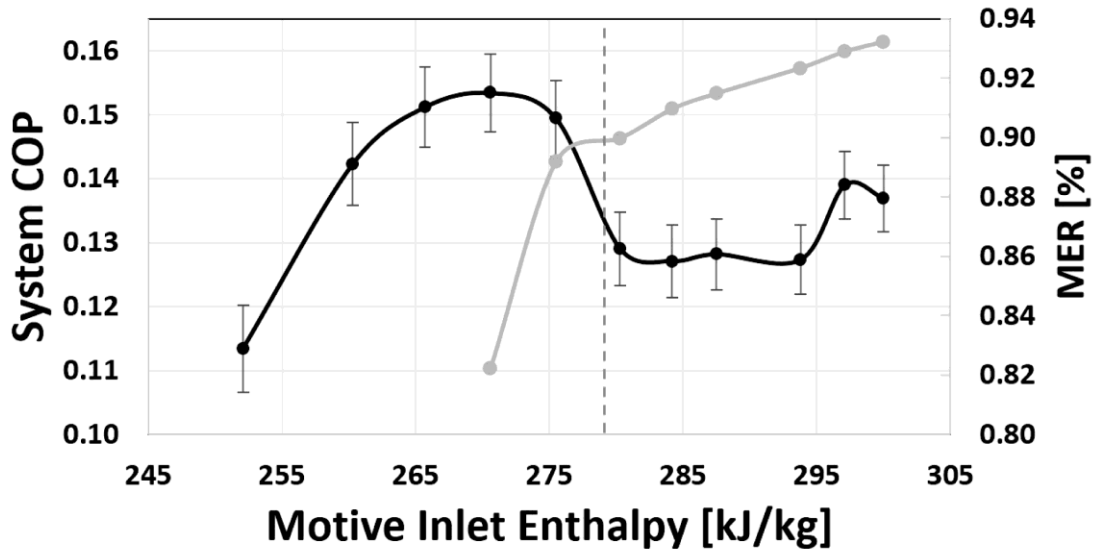


(b)

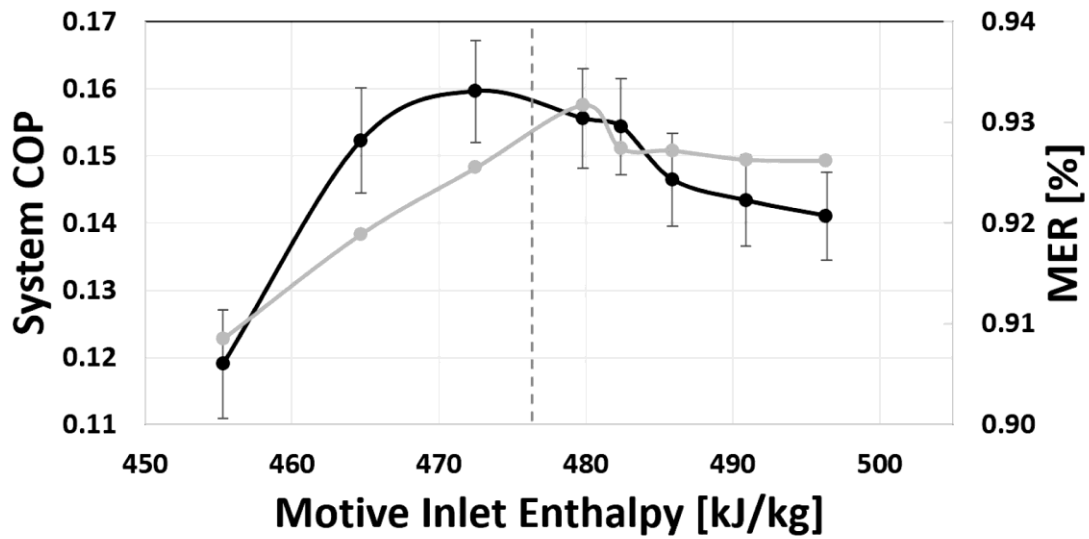
Figure 5.8: Plots of MER and MER<sub>max</sub> for (a) R134a and (b) R245fa.

superheated motive inlet conditions for R245fa. But for both R134a and R245fa, momentum transfer effectiveness ultimately decreases with decreasing superheat.

Because MER is related to COP with the Equation 5.14, it is initially expected that the trend of MER should follow the COP trend exactly.



(a)



(b)

Figure 5.9: MER/MER<sub>max</sub> for (a) R134a and (b) R245fa.

$$COP = \frac{\dot{m}_s}{\dot{m}_m} \left[ \frac{(h_{\text{evaporator outlet}} - h_{\text{evaporator inlet}})}{(h_{\text{boiler outlet}} - h_{\text{boiler inlet}})} \right] \approx MER \left[ \frac{(h_{fg, \text{evaporator}} + h_{\text{sup, evaporator}})}{(h_{fg, \text{boiler}} + h_{\text{sup, boiler}})} \right] \quad (5.14)$$

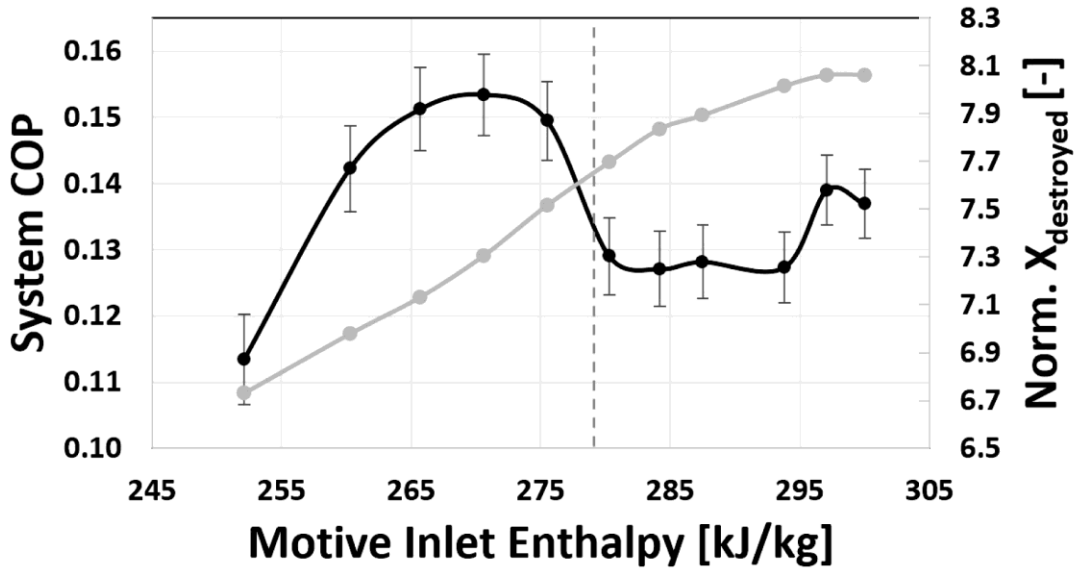
While the values of  $h_{fg, \text{evaporator}}$  and  $h_{\text{sup, evaporator}}$  remain about the same for all test conditions, the value of  $h_{fg, \text{boiler}}$  decreases slightly, and  $h_{\text{sup, boiler}}$  decreases significantly with decreasing

motive inlet enthalpy. As a result, the quantity in brackets increases. This explains the increase in COP while MER remains constant or decreases slightly. One way to conceptualize the combination of these factors is that MER represents phenomena internal to the ejector, whereas COP superimposes the cycle-level effect of energy savings at the boiler.

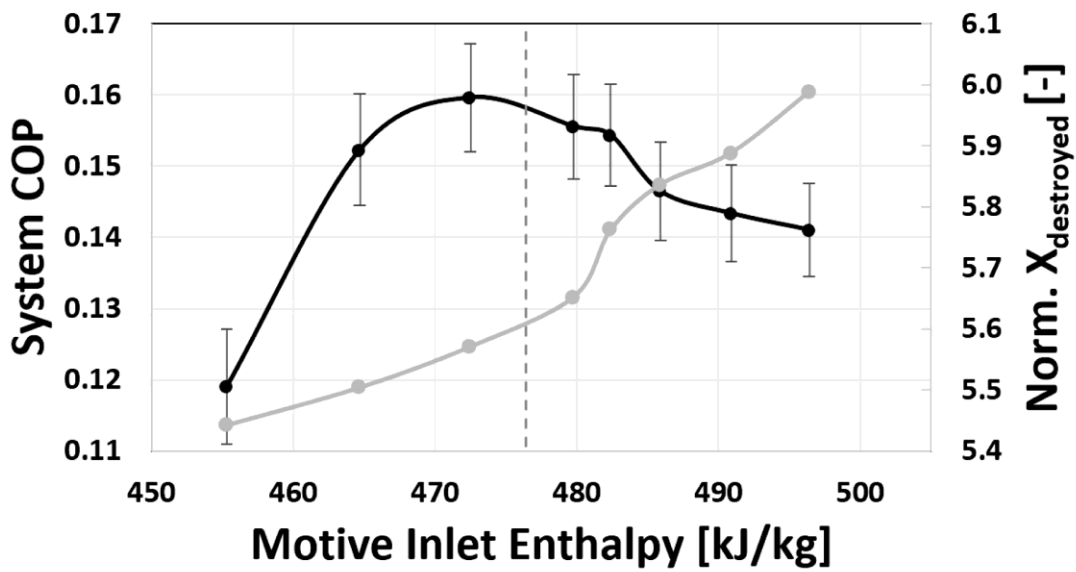
#### **5.4.4 Effect of Phase Change**

As mentioned in Section 5.3.2.3, differences between MER and  $MER_{max}$ , such as those seen in Fig. 5.8, are a result of reduced momentum transfer effectiveness inside the ejector. In general, any process that results in entropy generation and related exergy destruction reduces the effectiveness of momentum transfer. Figure 5.10 shows the change in normalized total exergy destruction in the ejector. As expected, exergy destruction decreases with reduced heat loss to the surroundings,  $\dot{Q}_{ext}$ , and reduced velocity mismatch in the mixing section when the motive flow condenses and decelerates. Exergy destruction is also expected to decrease as the strength of shocks in the motive jet decreases at conditions with lower jet velocities and/or two-phase flow. While COP does generally rise as exergy destruction decreases, this decrease does not explain the decreases in the effectiveness of momentum transfer. Therefore, it is inferred that the major factor influencing momentum transfer effectiveness is not due to the sources of irreversibility indicated above, but instead is due to factors influenced by the mechanics of two-phase flow.

MER is governed specifically by the work output of the motive jet, and it is expected that an increase in MER and COP would correspond to a higher available  $\dot{W}_{jet}$  in



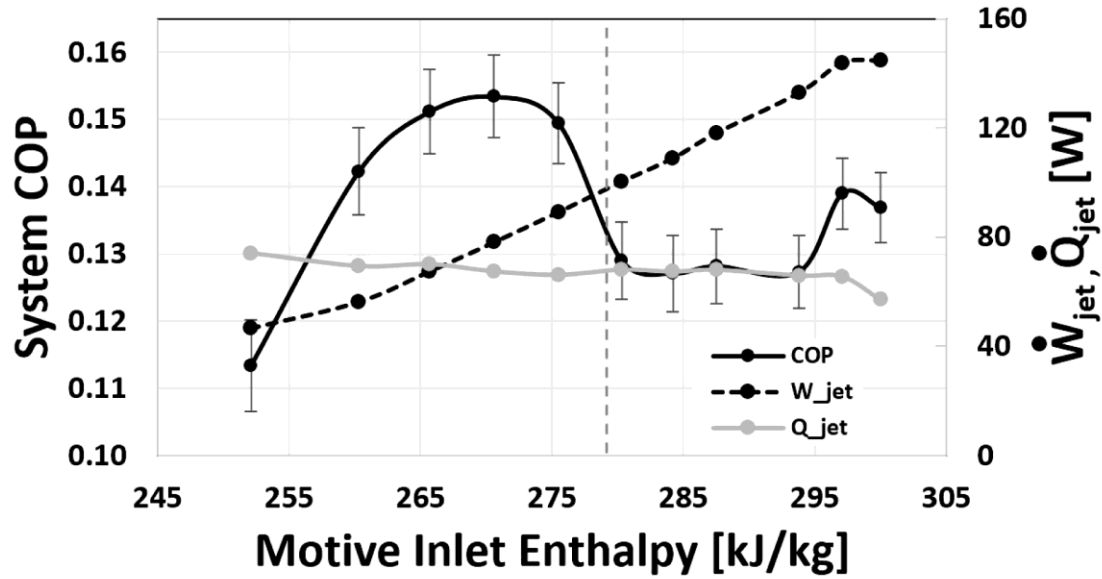
(a)



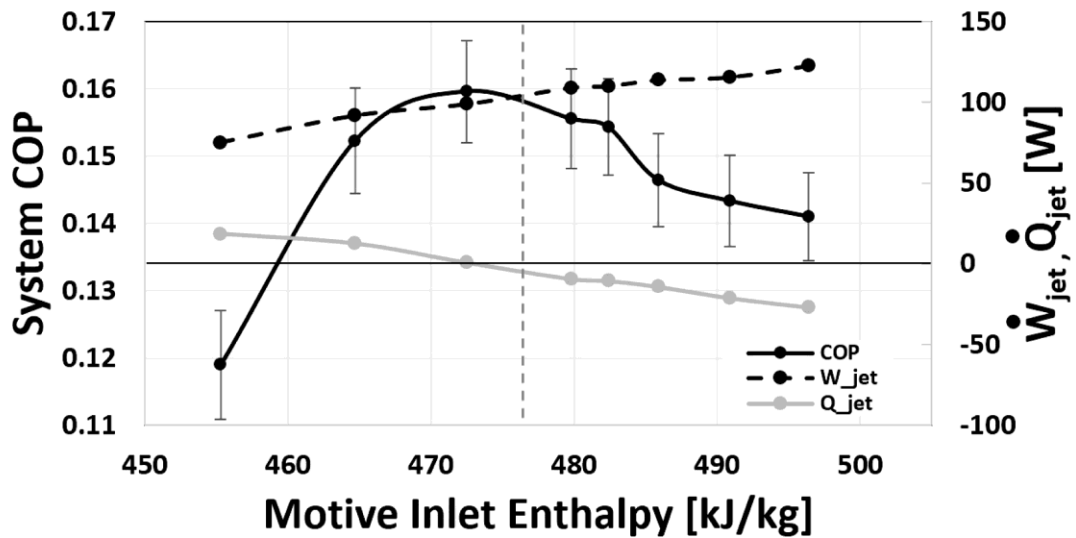
(b)

Figure 5.10: Plots of normalized exergy destroyed,  $\dot{X}_{destroyed} / (\dot{m}_m h_m)$ , for (a) R134a and (b) R245fa.

Fig. 5.11. While the absolute value of  $\dot{W}_{jet}$  actually decreases as COP increases, normalized  $\dot{W}_{jet}$ , given in Fig. 5.12, does generally increase with COP. At lower motive nozzle inlet enthalpies, less energy is needed to drive the lower cycle, and the  $\dot{W}_{jet}$  available is better



(a)



(b)

Figure 5.11: Plots of  $\dot{W}_{jet}$  and  $\dot{Q}_{jet}$  for (a) R134a and (b) R245fa.

able to supply the power needed for the lower cycle. However, as shown in Fig. 5.9, there is either a declining or constant momentum transfer efficiency with decreasing motive inlet enthalpy. This is an indication that a different mechanism between the motive jet and suction flow hinders the transfer of  $\dot{W}_{jet}$  to the suction flow.



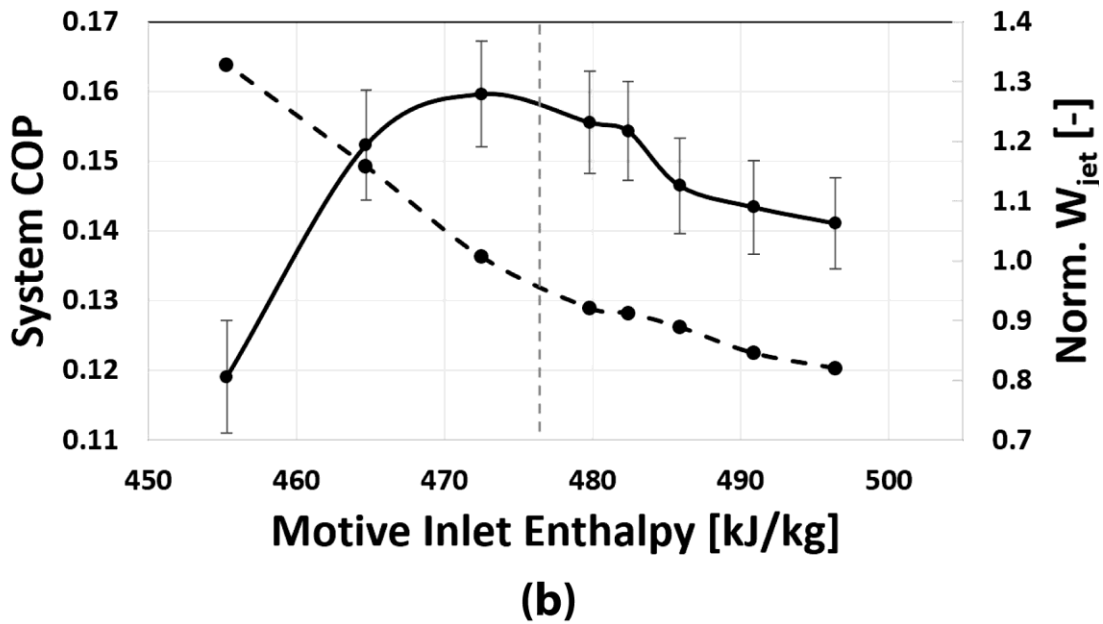
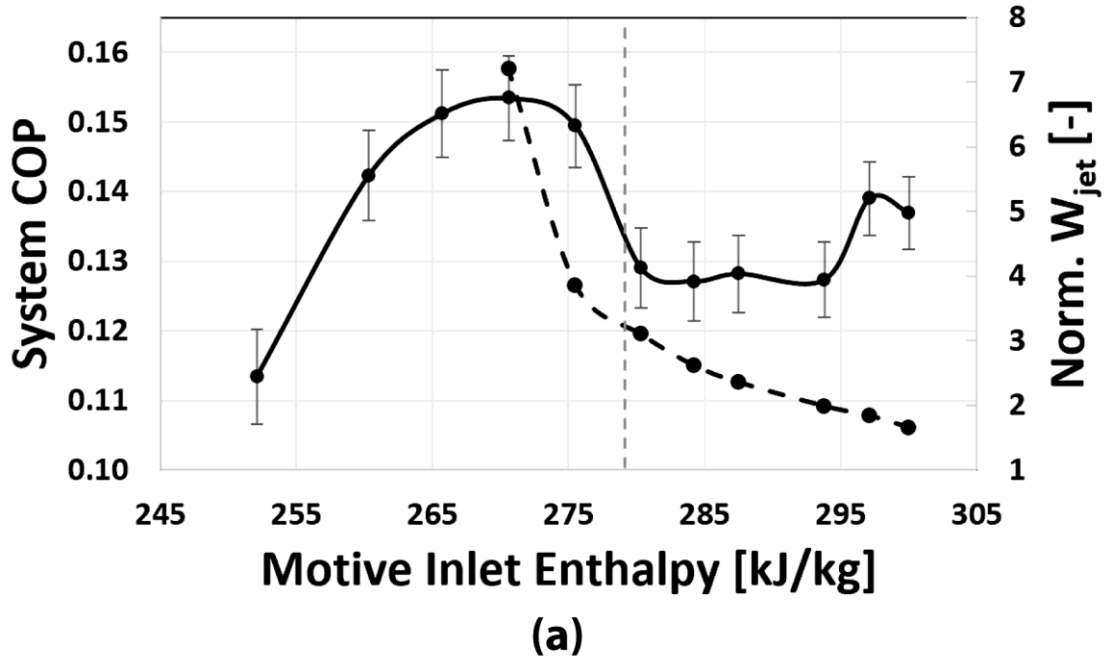
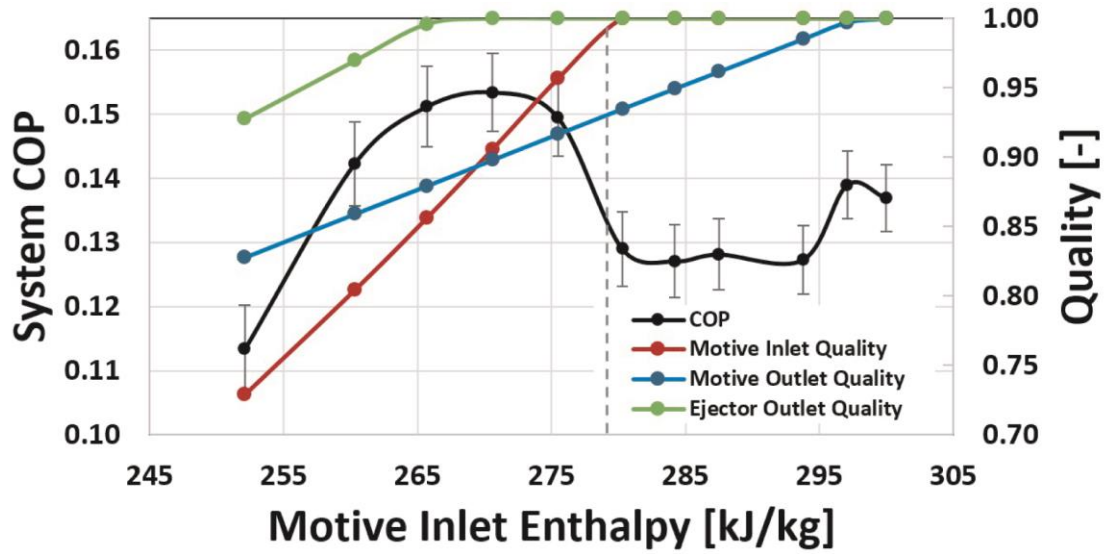
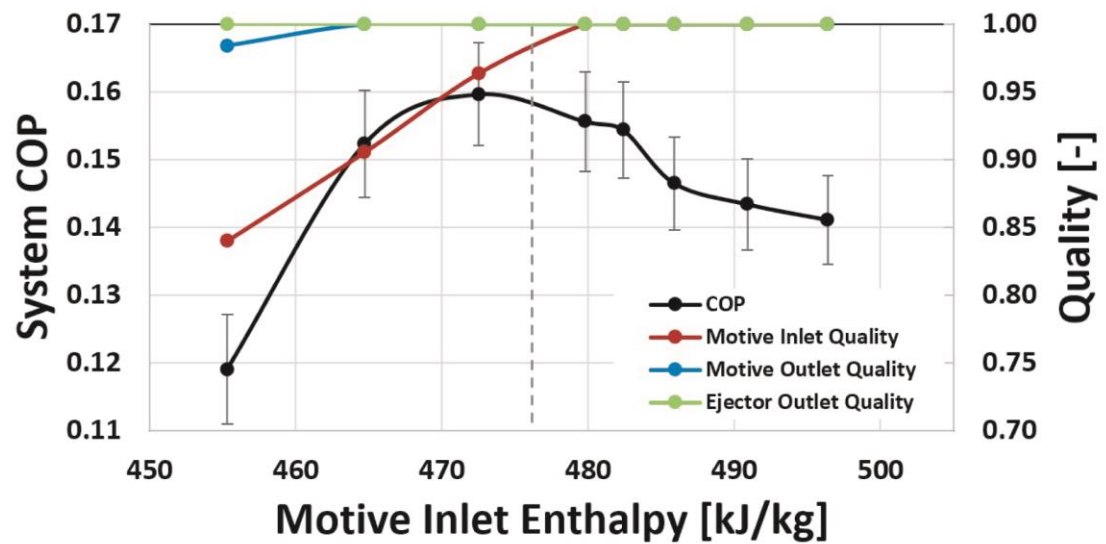


Figure 5.12: Plots of  $\dot{W}_{jet}$  normalized by the total energy needed to drive the suction flow at maximum entrainment conditions,  $\dot{W}_{jet} / (\dot{m}_{s,max} (h_o - h_s))$ , for (a) R134a and (b) R245fa.

From the values of quality at various points inside the ejector in Fig. 5.13, it can be seen that the onset of condensation at the various points in the ejector seems to coincide



(a)



(b)

**Figure 5.13: Plots of quality at the motive nozzle inlet, motive nozzle outlet, and ejector outlet for (a) R134a and (b) R245fa.**

with inflection points in the COP curve. This implies that condensation has an important influence on system operation. For R134a, the steady decrease of momentum transfer effectiveness in Fig. 5.9 (a) seems to coincide with a steady increase in the degree of condensation at the motive nozzle outlet, and decreases significantly as flow condenses so

much that condensation can be seen at the ejector outlet. Condensation also lowers the energy output of the upper cycle. At conditions where the motive nozzle inlet is superheated but the motive outlet is saturated, the values of  $MER_{max}$  are slightly lower. This causes the drop in COP seen for motive inlet enthalpies just before saturation.

R245fa does not exhibit this behavior because two-phase flow at the motive nozzle outlet only occurs to a small degree at very low motive inlet enthalpies. Performance is relatively constant for conditions of superheated motive nozzle inlet enthalpies, as seen in Fig. 5.8 (b), and COP rises because of reduced heat input at the boiler needed for superheating. When the nozzle inlet condition starts to become saturated and the nozzle outlet is still superheated, there is a small increase in maximum MER and momentum transfer effectiveness. But this is immediately negated as the nozzle outlet starts to become saturated, maximum MER drops, and momentum transfer efficiency decreases as a result.

The correlation between reduced momentum transfer effectiveness and decreasing motive nozzle outlet quality indicates that the presence of larger condensate droplets reduces performance. As droplet size increases, interactions between the motive and suction flows become less thermodynamically dominated and more mechanically dominated. In the mechanically dominated case, droplets are bigger and start to exhibit more pronounced drag effects. As such, droplet velocity decreases along with the ability of that droplet mass to transfer momentum to the suction flow, thereby decreasing MER.

The above discussion provides some explanations for the conflicting results pertaining to the effects of condensation in the literature. If considering only the ejector, the effect of condensation is negative (MER drops). However, when considering the ejector

in a chiller cycle, having conditions where condensation is present is beneficial because of energy savings in the boiler (COP rises), not because of benefits related to the condensation mechanism itself. The negative effects of condensation observed in this study may have been captured to some degree in simulations of two-phase flow by Hemidi *et al.* (2009a). The experimental performance increases seen in Hemidi *et al.* and Al-Ansary and Jeter (2004) are neither confirmed nor disputed by the present study, because they were only observed at off-design conditions. The present study observed performance at on-design conditions (except at very low motive inlet enthalpies).

Considering the practical use of ejectors in chiller systems, detrimental condensation conditions should not be avoided at all costs. Instead, the ejector can tolerate condensing flow conditions while maintaining reasonable levels of performance without damage. As a result, notable cycle-level benefits are attained when avoiding superheat at the motive nozzle inlet, both increasing cycle COP and decreasing the required the temperature of the driving waste heat source.

## **5.5 Conclusions**

The effect of flow condensation on ejector performance in cooling systems has been a topic of discussion among researchers in the field. Many initial studies have speculated that the presence of condensation would be detrimental to ejector component and ejector system performance, whereas subsequent experimental work has found some performance improvement with the insertion of liquid droplets. In an effort to gain further insights into these effects, this study enabled the observation of ejector performance at varying operating conditions in an ejector-based chiller system using wet R134a and dry R245fa as working fluids. Keeping suction inlet temperature and pressure as well as ejector outlet pressure

constant, the inlet condition of the motive inlet was changed to observe the effects of changing mixing section conditions on ejector performance. It was found that the overall COP of the cycle is a combination of two main factors: the use of a wet vs. dry fluid, and the effectiveness of momentum transfer inside the mixing section of the ejector.

Focusing first on the motive nozzle, two different models were formulated to predict the conditions within the nozzle as refrigerant expands from high temperature and pressure inlet conditions to ejector mixing section conditions. The “frozen flow” model predicts properties assuming the flow is completely dry and follows the ideal gas law equation of state. The “equilibrium flow” model does the opposite, assuming the flow comes to full equilibrium, incorporating the formation of any droplets that may occur at qualities  $< 1$ . It is found that commonly available CFD models closely follow the equilibrium flow conditions, and therefore do not account for any metastable effects that may be present and important in the high-speed flows seen in nozzles. The use of the frozen and equilibrium flow models provide preliminary tools for motive nozzle design such that the resulting condensation shock can be forced at the motive nozzle throat to best maintain stable ejector flow with wet fluids. A comparison of these models provides an expected range of flow properties at the motive nozzle outlet, and also highlights errors introduced when assuming either ideal gas or full equilibrium behavior.

In general, condensation effects, typically present for the wet R134a fluid, seem to cause two negative side-effects. First, the ratio of energy needed to energy provided by the lower and upper cycles, respectively, is unfavorable when motive nozzle flow expands into the saturation dome from a superheated state. Second, an increasing degree of condensation in the mixing section is detrimental for the momentum transfer from the motive to suction

flow as droplet size grows and drag effects become more dominant. A dry fluid like R245fa does not suffer from these effects. In summary, the general trend of MER and COP is primarily influenced by the specific shape of the vapor-liquid dome of the specific fluid used, with small changes due to the two-phase flow effects. In the case of R245fa, these two-phase flow effects are less pronounced, and occur only at the lowest motive inlet enthalpies.

To maximize MER, it is desirable to have a motive inlet condition that is superheated if using a wet fluid, and only slightly superheated if using a dry fluid. But MER and COP trends are dominated more by fluid selection, and the energy savings realized at the boiler by decreasing motive inlet superheat tend to override any performance decrease from two-phase effects. As such, it has been demonstrated in this study that reducing the degree of superheat at the ejector motive nozzle inlet actually improves system performance, and conditions where condensation may occur should not be avoided. Specifically, a 12-13% improvement in COP was realized by significantly reducing the enthalpy at the motive nozzle inlet. Additional system-level improvements lie in the ability to use significantly lower waste heat temperatures (at 84.3°C vs. 98.4°C for R134a, and 107°C vs. 123°C for R245fa) to drive the system, while maintaining a similar cooling load. These findings show that a change in the operational regime for ejector-based chillers can provide relatively simple and low cost ways to achieve notable overall system improvement.

## CHAPTER 6

### CONCLUSIONS AND RECOMMENDATIONS

A comprehensive study on ejectors for use in waste heat driven chillers was conducted, starting with an investigation of the influences of fundamental flow characteristics on component-level operation, and concluding with an exposition of the effects of these flow phenomena on system-level performance. Particular emphasis was given to the understanding of the effects of potential two-phase flow in the ejector on system performance, for which previous investigators have reported conflicting results. The majority of available analytical studies are limited by ideal gas flow, normal shock, and isentropic efficiency coefficient assumptions. Numerical models that use a variety of turbulence models have not yet been validated, and there is not, as yet, accurate modeling of two-phase flow effects.

This work addressed these gaps in the literature by providing a basis for numerical model validation with the development of combined visualization and data reduction techniques. A full ejector-based chiller was designed and fabricated for the purpose of examining different two-phase flow conditions inside the ejector, and a transparent ejector test section was designed and operated at the high temperature and pressure conditions representative of ejector-based chiller operation. Providing the first ever undistorted visual access to an ejector operating with refrigerant (rather than air-water mixtures), a direct comparison of real flow features with those predicted by CFD could be performed. From these experiments and the corresponding analyses, it appears that flow exiting the nozzle may be approximated as being at full equilibrium, and increasing degrees of condensation at the nozzle exit corresponded to a drop in MER and ejector component performance.

However, it was found that decreasing the degree of superheat at the motive nozzle inlet resulted in a COP increase of >12% while at the same time using waste heat temperatures >14 K below that of the conventional (~10 K superheat) case. This performance improvement was demonstrated for two different types of fluids: a wet fluid, R134a that is more prone to two-phase flow conditions, and a dry fluid, R245fa that is less likely to lead to two-phase flow conditions. Using the insights gained from flow visualization along with experimental inlet and outlet conditions, two different models of ejector flow with these fluids were developed, one predicting the onset and degree of condensation inside the motive nozzle, and one differentiating between the effects of two-phase flow, heat transfer, and momentum transfer effectiveness inside of the mixing section. It was found that while MER would drop with increased condensation because of decreased momentum transfer effectivenesses, overall cycle COP would increase because of significant energy savings and lower source temperature requirements at the boiler.

From these trends, the following suggestions are made for the design and operation of ejector-based chiller systems:

- To best balance the opposing influences of condensation and boiler energy savings on COP, the ejector-based chiller should be operated such that the motive nozzle inlet condition is near saturation, but inside the vapor-liquid dome.
- In general, the motive nozzle outlet diameter should be designed such that temperature and pressure at the motive nozzle outlet match suction inlet properties as closely as possible to avoid parasitic heat transfer effects.



- If possible, a dry fluid should be used to minimize the adverse effects of condensation. The use of R245fa is suggested because of its additional benefit of having a low Global Warming Potential.

With these simple changes in ejector geometry and operational paradigm, the COP of ejector-based chillers, whether operating with a wet or dry fluid, can improve by more than 12% with respect to the conventional operating condition while allowing the cycle to be used over a much wider range of applications with lower waste heat temperatures. Considering the simplicity of operation and fabrication, as well as compact package sizes facilitated by ejectors, these ejector-based chillers can find use in waste-heat-driven cooling systems, especially in remote or portable applications where electricity usage and package sizes are at a premium.

### **6.1 Recommendations for Future Work**

There are several additional opportunities for continued work in the area of two-phase flows in ejectors and ejector based chillers:

- While this work was able to successfully visualize ejector flows of refrigerant at conditions representative of ejector-based chillers, some imperfections in the transparent test section made validation of numerical models difficult. Further refinement of such transparent test sections capable of high pressure operation should be conducted, to yield better sealing within the ejector, especially at the motive nozzle tip where the ejector geometry is particularly critical to operation. Advanced manufacturing techniques for the test section that reduce the number of surfaces to be sealed would achieve such improved test sections.

- To conclusively determine the outlet state of the motive nozzle, a pressure tap at the motive nozzle exit should be incorporated into the ejector test section design. Pressure taps along the length of the ejector mixing section and diffuser would also be helpful for the purposes of numerical and analytical model validation.
- While the shadowgraph visualization technique used in this work was effective in imaging the flow, other visualization techniques should be explored to improve image quality. This is especially the case for conditions showing higher degrees of condensation where optical access to flow features was obstructed by the condensate. Schlieren, PIV, and Rayleigh scattering techniques should be explored for use with a transparent ejector test section offering undistorted visual access, much like the one developed in Chapter 4. PIV visualization would have the added benefit of resolving the velocity flow field, and Rayleigh scattering would be able to detect condensate droplet sizes and densities.
- The model used in this work to approximate condensation inside the motive nozzle employed many assumptions. While this was sufficient for the presented analysis, it should be developed further. First, the Wilson line for the refrigerant under consideration should be derived from a fundamental basis. Second, an approximation for entropy change across a condensation shock should be incorporated. Third, an approximation of frictional losses with the motive nozzle walls should be included. With these changes, it is expected that the accuracy of predicted outlet condition of the motive nozzle can be improved.
- Because of the complexity of ejector flows, the best available tools for predicting flow characteristics are numerical simulations. The major limitation to currently-available

modeling software is the inability to incorporate two-phase effects. New models must incorporate the formation of droplets, including the effects of metastable states and condensation shocks. Mechanical coupling of the condensate droplets with the bulk flow is also needed to reflect the observed changes in momentum transfer effectivenesses that are due to droplet drag effects. It may be possible to do this by augmenting the “wet steam” model in ANSYS FLUENT, and such work is currently underway. Once development is completed, it will be critical to validate the model with the visualization techniques developed in this work by specifically matching flow feature angles and the number of shock cells present. When this validation is performed, it has been found in previous work by the author that wall effects must be accounted for. Therefore, the CFD model for validation must include a full 3D simulation of the flow.

- There are other components in the ejector-based chiller cycle that have an influence on overall cycle COP. Namely, the effectivenesses of the condenser and boiler may change with a shift in motive nozzle inlet condition. While it is expected that combined effects of the condenser and boiler effectivenesses will be minor, this should be confirmed with further study.
- The transparent ejector (with rectangular cross-section) developed in this work was not only useful in providing undistorted visual access to the ejector, but it also has utility as an easily manufacturable geometry for specific ejector-based chiller configurations. The development of this chiller configuration with passive cycle concepts from the literature could lead to the commercialization of ejector-based chillers that can be used in a wide range of remote and mobile applications.

## APPENDIX A

### SHADOWGRAPH VISUALIZATION SETUP INSTRUCTIONS

All images in this work were taken using the shadowgraph visualization technique. While the Schlieren visualization technique is more commonly used for visualizing such flows, the shadowgraph visualization technique was chosen here for greater repeatability of the captured images. A Schlieren image captures the gradient of density in an air flow (whereas a shadowgraph image captures the Laplacian of density), and typically provides better contrast such that more subtle flow features can be visualized. But Schlieren images are also heavily dependent on the position and angle of the knife edge used to obstruct divergent light paths, consequently accentuating or obstructing different flow features at different knife positions. Because the shadowgraph method proved to be sufficient for identifying shock and expansion flow feature angle, it was used instead of the Schlieren method to avoid any unnecessary complications associated with knife edge placement. But it should be noted that Settles (2001) provides detailed guidance on correct placement of the knife edge to best accentuate the desired flow feature for a given Schlieren setup.

The setups used to capture the shadowgraph images in Chapters 3 and 4 were slightly different. In Chapter 3, there was some evidence of minor image distortion. The setup used in Chapter 4 (Fig. 4.6) included several improvements. First, it used a cube beam splitter rather than a plate beam splitter to avoid double-imaging effects. A plate beam splitter tends to reflect two images of the flow to the camera; one that reflects off the front surface of the plate and one that reflects off the back. A cube beam splitter avoids this effect because the reflective surface is a single interface between two pieces of glass.

Second, the light source was collimated to make sure parallel light rays would pass through the test section. This was done by positioning the point light source exactly at the focal point of convex side of the plano-convex lens. As such, the path of each light ray through the test section would be equal, and image distortion would be significantly reduced, especially at the edges of the visualization region. Third, a higher quality material was used for the window material. In Chapter 3, the test section had Plexiglas windows with a higher index of refraction as well as small cracks that could be seen in the images. The improved setup in Chapter 4 used borosilicate glass, chosen specifically for its lower index of refraction and improved optical clarity. Images showed minimal imperfections in the glass.

With these changes, there was notable improvement in flow image quality. Distortion effects and imperfections were greatly reduced. Best image quality can be obtained by using the following guidelines.

### **A.1 Attach components to optics rail**

To make alignment of the visualization components as easy as possible, they should all be attached to an optics rail. This allows for translation of the components forwards and backwards without changing axial alignment. Furthermore, once the optical components have been aligned, the whole rail can be moved easily to be aligned with the flat mirror in the back the test section, as discussed below.

### **A.2 Set up concentrated point light source**

For the clearest shadowgraph image, the brightest and smallest possible point light source should be used. The simplest way to make a point light source is to position the tip of a fiber-optic cable (connected to a fiber-optic illuminator) in the desired position, and cover it with foil that has a pin hole slit in it. While this technique works, a major portion of light

from the illuminator is blocked by the foil, and the shadowgraph images will be much dimmer and require a much lower shutter speed to capture the images. If a higher shutter speed can be used in combination with a brighter light source, sharper images of the flow can be obtained. Therefore, the light source is concentrated, allowing all the light from the illuminator to be focused at one point to produce a much brighter light source. To accomplish this, a microscope objective was positioned immediately in front of the fiber-optic cable and used to focus the light. The other side of the objective produced a much brighter point light source.

### **A.3 Find correct position of plano-convex lens**

The positioning between the point light source and the plano-convex lens is critical to produce a collimated light source for passage through the test section. Each lens has a different focal length, with the one used in Chapter 4 having a focal length of 300 mm. The end of the microscope objective must be placed 300 mm from the convex side of the plano-convex lens using a ruler. But because this spacing is critical, it must be checked. This can be done by placing a piece of paper immediately after the lens and tracing the circular outline of the light coming through. If the light is perfectly collimated, moving this piece of paper straight back on the optical rail does not change the diameter or shape of the light outline on the paper. If moving the paper back changes the diameter of the light, then the position between the light source and the lens must be adjusted. If the shape of the light changes, the angle of the lens within its holder must be adjusted to make sure it is perfectly perpendicular to the light path. Conversely, the position of the point light source can be changed up and down or left to right to ensure that it is along the same axis as the center

of the lens. Once this spacing is precisely set, the lens should be placed as close as possible to the front of the test section.

#### **A.4 Camera placement**

Keeping the plano-convex lens as close as possible to the test section enables the camera also to be as close as possible to the test section. This leads to the largest possible image projection on the CCD of the camera for the highest resolution image. The camera should also be roughly perpendicular to the collimated light path to allow for correct setup of the beam splitter.

#### **A.5 Insert cube beam splitter**

The cube beam splitter is placed between the point light source and the lens and in front of the camera, as shown in Fig. 4.6. Alignment of the beam splitter depends on the position of the camera. Once the camera is in place, the beam splitter should be rotated until the center the shadowgraph image is on the center of the CCD in the camera.

#### **A.6 Checking for image distortion**

Once the setup has been aligned, the shadowgraph image should be checked to confirm alignment of the optical components with respect to the flat mirror. Because the flat mirror is physically inside the test section, and the test section is connected to the overall system that vibrates during pump operation, this can be somewhat challenging.

To check for image distortion and correct alignment, a grid reticule is placed on the outer surface of the test section. If the grid is perfectly square throughout the shadowgraph image, the image is undistorted, and light passing through the test section is correctly collimated. If there are two images of the grid slightly offset from each other (or if there are two images of any other visible feature, such as the nozzle tip or any imperfections in

the image like a dust particle), the orientation of the optical rail with respect to the flat mirror must be changed. This can be done by translating the rail left or right, or tilting it slightly with shims. Consequently, the combination of camera and beam splitter position must be realigned as well.

Once image distortion has been eliminated and correct alignment verified, the setup is ready to take images of the flow. For subsequent analyses, it is recommended that an image be taken of the test section without flow, and without flow with the reticule in place. The reticule image provides a scale against which flow geometry and features can be measured. The image without flow can later be compared to an image with flow to distinguish between visualized flow features from imperfections in the test section and those from the motive flow.

More detailed information on the fundamentals of shadowgraph imaging, as well as related Schlieren imaging can be found in Settles (2001).

### **A.7 Checking for image resolution and optical aberration**

As mentioned above, the largest possible image was projected on the CCD of the high speed camera. At the magnification used, an image at a resolution of 448 x 688 pixels was captured. Using a grid reticule, it was found that at this resolution, one pixel would resolve flow features down to  $\sim 11 \mu\text{m}$ , and the visualized shock and expansion flow features measured between two and five pixels in width.

To rigorously check for any optical blurring effects, all optical components should be precisely aligned along a central axis, as depicted in Fig. A.1. Optical blurring or aberration effects would occur as the result of imperfections or changes in the index of



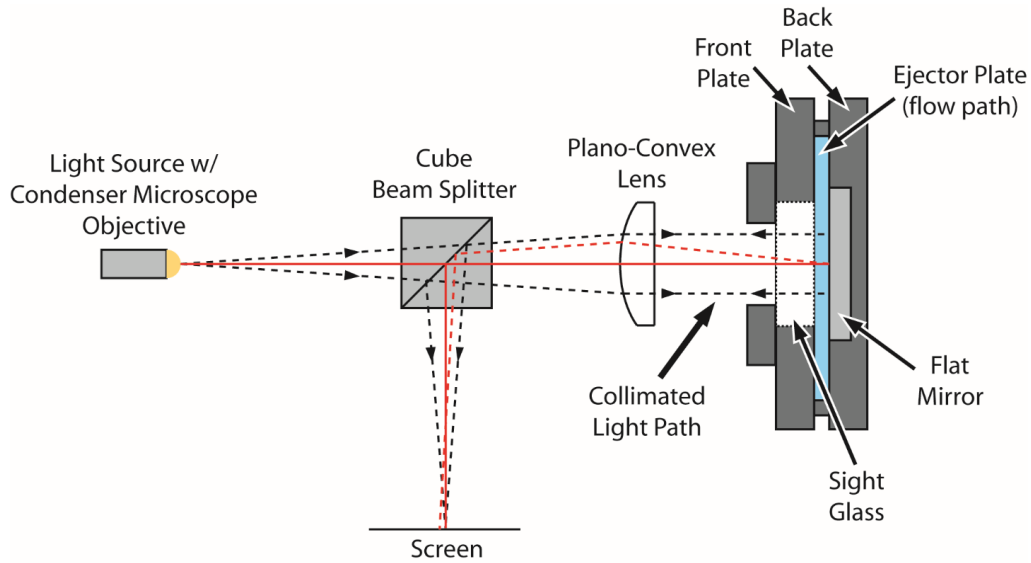


**Figure A.1: Sample precision alignment of optical components using laser guide. Dotted red line shows sample optical blurring effect that would occur from an imperfection in the flat mirror component.**

refraction of the various components. For example, in Fig. A.1, an imperfection in the flat mirror would have the effect of diverting a given ray. The effect would be a blurring of observed flow features, like that shown in Fig. A.2. On the left is the ideal clear flow image (for example a shock wave) with a given width at a given angle,  $\theta$ . After optical aberration

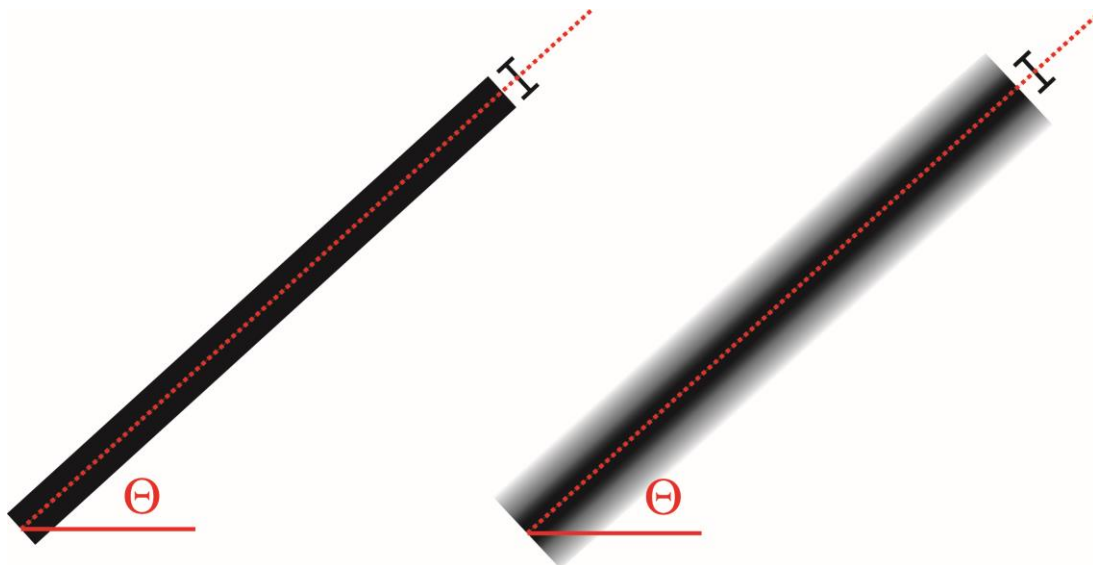


**Figure A.2: Sample optical aberration effect where a given flow feature (left) would be blurred (right). While this may lead to errors in measurement of the width of the flow feature, measuring the feature angle is not affected appreciably.**

effects, this distinct flow feature would be blurred and look more like the right side of the figure. In this case, the width of the flow feature becomes more difficult to measure, but angle can still be readily discerned. In this study, the angle of a flow feature, not the feature width, was important for interpretation of the data. Therefore, optical aberration effects are not expected to meaningfully affect the results. Despite this, to check for optical aberration, a grid reticule was used. The lines printed on the reticule were measured and compared with the specified width of  $25 \pm 13 \mu\text{m}$ . Images of the grid when placed in front of the flow path show this width to be about three pixels wide. Given the limitations of this visualization setup, it can be assumed that any optical aberration effects were minimal and led to negligible error when measuring the angle of flow features for the validation analysis performed.

## **APPENDIX B**

### **EJECTOR-BASED CHILLER OPERATIONAL PROCEDURES**

The ejector-based chiller test facility used to collect data in Chapters 4 and 5 is made specifically for the purpose of providing the desired inlet and outlet conditions to the transparent (rectangular cross-section) and non-transparent (circular-cross section) test sections used for visualization and cycle-level studies, respectively. The operational procedures of importance are detailed below.

#### **B.1 Test Facility Charging**

To ensure that the system operates with a pure refrigerant during testing, the test facility is first evacuated using a vacuum pump. During the evacuation process, all the valves in the system are opened and closed sequentially to ensure that any air trapped inside the valve packings is released and removed. A vacuum gauge connected to the system during evacuation is used to ensure that an appropriate vacuum is established, with a threshold of 400 Pa deemed suitable for charging. This evacuating process takes about 20 minutes.

The system is immediately charged with R134a or R245fa, depending on the experiment being conducted. To do so, the refrigerant tank is connected to the lowest point in the cycle, and inverted such that liquid refrigerant is drawn into the system. The changing weight of the tank is monitored with a refrigerant scale. After charging the refrigerant hose between the refrigerant tank and the system, the balance is zeroed. Opening the connection to the system, the total refrigerant entering the fluid loop is recorded. For both R134a and R245fa, the total fluid charge is measured to be ~ 2.3 kg. After charging the system with the appropriate amount of refrigerant, the refrigerant tank in the system is approximately

75% full of liquid at resting conditions, as could be checked with the level gauge on the refrigerant tank. At this point, the system is ready for startup.

## **B.2 Operational Procedure**

The basic startup procedure for the ejector-based chiller involves first getting the desired state points in the upper loop, and then slowly opening the lower loop to achieve cooling at the evaporator. To start this process, the expansion valve is closed to isolate the lower loop, and the fluid pump is started at a low speed ( $\sim 10$  Hz) until the motive flow meter registered a steady flow rate ( $\sim 0.2$  kg min<sup>-1</sup>), and flow could be seen in the sight glass at the ejector outlet. The chiller is then started and set to a temperature slightly below ambient ( $\sim 20^\circ\text{C}$ ). The superheater heat load is then increased incrementally to full power, and then the boiler heat load is also be increased. The speed of the pump is also increased as needed to ensure that the flow exiting the boiler is not significantly superheated (as this could lead to damage of the boiler heating element). This procedure continues until the desired high side boiler temperature and pressure is reached. The chiller set point temperature is then lowered incrementally until the desired condenser pressure is reached, where fine adjustment is made by adjusting the rotameter on the coupling fluid line to the condenser. Again, the boiler heat input and pump speed is adjusted to maintain high-side conditions while the condenser conditions changed.

At this point, the system is ready for suction flow entrainment. The expansion valve is opened slowly until a low, steady flow rate through the evaporator registers on the suction flow meter ( $\sim 0.1$  kg min<sup>-1</sup>). The evaporator heater is then turned on incrementally until a  $\sim 10$  K superheat is achieved at the exit of the evaporator. Opening of the suction

line requires constant adjustment of the pump speed, boiler heat input, and chiller temperature to maintain the desired boiler and condenser pressures.

To ensure that the ejector is operating at on-design conditions, the condenser pressure is lowered while maintaining evaporator pressure and motive nozzle inlet conditions. No change in entrained suction mass flow rate with decreasing condenser pressure indicates that the ejector is operating in the on-design regime.

### **B.3 Data Point Capture**

Once the desired boiler, condenser, and evaporator pressures are reached at the motive nozzle inlet condition of interest, the approach to steady state is monitored for 20 minutes. After this period, data point sets are recorded for 120 seconds at a sample rate of 1 Hz. To ensure that the collected data does not exhibit hysteresis effects and are repeatable, and to confirm steady-state operation, the test matrices are collected in forward (points of decreasing motive nozzle inlet enthalpy) and reverse order (increasing motive inlet enthalpy). While this is possible with the non-transparent ejector test sections used in Chapter 5, it is not possible for the transparent test section in Chapter 4 because of the imperfections in the test section described in Section 4.4.2.

## APPENDIX C

### SAMPLE CALCULATION AND UNCERTAINTY ANALYSIS

The important quantities for this work are the motive nozzle inlet enthalpy, as well as ejector component MER and overall cycle COP. The calculation of these values and associated uncertainties is described here.

#### C.1 Motive Nozzle Inlet Enthalpy

Accurate determination of the enthalpy at the motive nozzle inlet is important for subsequent calculations of motive nozzle outlet conditions. For conditions where the motive nozzle inlet is superheated, the motive inlet enthalpy can be calculated directly using measured values of temperature and pressure. But at conditions where the nozzle inlet is saturated, an energy balance on the boiler is necessary to determine enthalpy.

For example, at the lowest motive nozzle inlet enthalpy case for R134a (last row in Table 5.1), the inlet condition is saturated. The measured pressure at the motive nozzle inlet is 2680.7 kPa. The motive mass flow rate is 0.8504 kg min<sup>-1</sup>, the boiler inlet temperature 30.43°C, and the measured heat input at the boiler and superheater is 2223.7 W. For the lowest superheat condition (Row 5 in Table 5.1), heat loss between the boiler inlet and motive nozzle inlet,  $\dot{Q}_{loss,boiler\ line}$ , is measured to be -19.5 W (heat lost to the ambient) from a comparison between measured motive inlet enthalpy from directly measured  $T$  and  $P$ , and calculated enthalpy from an energy balance about the boiler line from the boiler inlet to ejector motive inlet.

A calculation of heat loss from the line between the boiler inlet thermocouple to the ejector motive inlet thermocouple takes into account thermal resistances of the convective pipe flow, wall and insulation conduction, as well as both convection and radiation heat transfer from the insulated surface of the pipes and heaters. The total thermal resistance from the fluid to the outer wall of the insulation is a sum of internal pipe flow convection resistance and two conduction resistances through the pipe and insulation:

$$R_{tot} = \frac{1}{h_{pipe} 2\pi r_{pipe,i} L_{section}} + \frac{\ln\left(\frac{r_{pipe,o}}{r_{pipe,i}}\right)}{2\pi L_{section} k_{pipe}} + \frac{\ln\left(\frac{r_{ins,o}}{r_{ins,i}}\right)}{2\pi L_{section} k_{ins}} \quad (C.1)$$

Here,  $h_{pipe}$  is taken to be 100, 300, and 10000 W m<sup>-2</sup> K<sup>-1</sup> for single-phase gas, single-phase liquid, and phase change flows inside the pipe. For the piping, the outer diameter and wall thickness are 12.7 mm and 0.9 mm, respectively. For the heater sections, the outer diameter and wall thickness are 38.1 mm and 0.9 mm, respectively. The insulation had a thickness of 38.1 mm. Thermal conductivities of the piping and insulation were taken as 16 and 0.035 W m<sup>-1</sup> K<sup>-1</sup>, respectively. The total heat loss is

$$\dot{Q}_{loss} = \frac{T_{flow} - T_{pipe,s}}{R_{tot}} \quad (C.2)$$

This total heat loss can be equated to total heat loss due to convection and radiation from the surface of the pipe insulation:

$$\dot{Q}_{loss} = \dot{Q}_{conv} + \dot{Q}_{rad} = h_{conv} A_{s,ins} (T_{ins} - T_{amb}) + \varepsilon_{ins} \sigma (T_{s,ins}^4 - T_{amb}^4) A_{s,ins} \quad (C.3)$$

Here,  $h_{\text{conv}}$  is found to be between 2 and 5 W m<sup>-2</sup> K<sup>-1</sup> using the correlation of LeFevre (1956) as an approximation for natural convection on a vertical tube. The surface emissivity  $\varepsilon_{\text{ins}}$  of the insulation is assumed to be 0.6. At an ambient temperature of 25°C, the total heat loss from the boiler inlet thermocouple to the ejector motive inlet thermocouple is about ~ -30 W for the lowest superheat condition, line Row 5 in Table 5.1. Of this, ~13 W is due to natural convection, while ~17 W is due to radiation. This loss of -30 W is in reasonable agreement with the measured value of -19.5 W reported above. Table C.1 shows the heat loss in each section of piping between these two thermocouples.

Assuming that the measured heat loss is approximately constant for all saturated motive inlet conditions (because the  $\Delta T$  between the boiler line and the ambient is almost constant), the enthalpy at the inlet to the motive nozzle is found as follows.

$$\dot{Q}_{\text{boiler}} + \dot{Q}_{\text{loss, boiler line}} = \dot{m}_{\text{motive}} (h_{\text{motive nozzle inlet}} - h_{\text{boiler inlet}}) \quad (\text{C.4})$$

**Table C.1: Piping heat loss values from the temperature measurement location at the boiler inlet to the motive nozzle inlet for the lowest superheat condition in Table 5.1 (Row 5).**

Pipe Section Description	Average Temperature [C]	$Q_{\text{loss}}$ [W]
$T_{\text{boiler inlet}}$ to boiler inlet	31	-0.29
Boiler heater section	58	-7.52
Boiler outlet to superheater inlet	87	-4.70
Superheater section	87	-3.64
Superheater outlet to $T_{\text{motive inlet}}$	88	-14.27
	$Q_{\text{loss,tot}}$	<b>-30.42</b>



$$2223.7 \text{ W} + (-19.5 \text{ W}) = (0.014 \text{ kg s}^{-1})(252100 \text{ J kg}^{-1} - 94190 \text{ J kg}^{-1}) \quad (\text{C.5})$$

The resulting motive inlet enthalpy for this case is 252.1 kJ kg<sup>-1</sup>.

## C.2 Ejector Component Heat Loss

Similarly, the heat loss from the ejector component is evaluated to determine the outlet condition of the ejector. Again using the lowest superheat condition (Row 5 in Table 5.1), the heat loss from the ejector,  $\dot{Q}_{loss,ejector}$  is measured to be -25.2 W (heat lost to the ambient) using

$$\dot{m}_{motive} h_{motive \text{ nozzle in}} + \dot{m}_{suction} h_{suction \text{ nozzle in}} = (\dot{m}_{motive} + \dot{m}_{suction}) h_{ejector \text{ outlet}} - \dot{Q}_{loss,ejector} \quad (\text{C.6})$$

$$\begin{aligned} & (0.014 \text{ kg s}^{-1})(284193 \text{ J kg}^{-1}) + (0.003 \text{ kg s}^{-1})(267063 \text{ J kg}^{-1}) \\ & = (0.017 \text{ kg s}^{-1})(279945 \text{ J kg}^{-1}) - (-25.2 \text{ W}) \end{aligned} \quad (\text{C.7})$$

Again, modeling the heat loss from the ejector considering all thermal resistances and convective and radiation heat losses to the ambient using the method described in Section C.1 above, the predicted value of heat loss is ~21 W. Of this overall heat loss, ~19 W are due to natural convection, while ~2 W are due to radiation. This is in reasonable agreement with the measured heat loss of -25.2 W reported above. Therefore, at all conditions where the ejector outlet is saturated, it is assumed that the heat loss from the ejector remains constant at the measured value.

## C.3 Uncertainty Analysis

Using the measurement accuracies for temperature, pressure, mass flow rate, and heat load indicated in Section 4.2.1, uncertainties in the calculated value of enthalpy as well as MER and COP are determined as follows.

$$U_Y = \sqrt{\sum_i \left( \frac{\partial Y}{\partial X_i} \right)^2 U_X^2} \quad (\text{C.8})$$

where  $Y=f(X_1, X_2, \dots, X_i)$ . For the values of enthalpy, the uncertainty was always  $< \pm 0.5\%$  of the calculated value. For MER and COP, uncertainties are tabulated in Tables 4.1, 5.1, and 5.2, as appropriate.

#### **C.4 Cycle State Point Calculations**

The table below gives a step-by-step calculation of different state point quantities and their uncertainties using the information supplied above. Values are given for the condition corresponding to the data point in the last row in Table 5.1 where the motive nozzle inlet condition is saturated. It should be noted that the COP values reported in this work are calculated directly from a ratio of heat input at the evaporator, to combined heat input at the boiler and superheater. As shown below, if heat losses and gains from the ambient are taken to account, COP values increase notably. For example, in Table C.2, the reported COP is 0.113 whereas after accounting for losses, this COP rises to 0.178. Future cycle construction should use smaller-diameter plumbing and increased insulation to decrease the negative effects of losses on measured cycle COP.

**Table C.2: Sample state point calculations for saturated condition given in last row of Table 5.1 for the R134a test matrix in Chapter 5.**

Cycle State Point Sample Calculation; Nov. 13, 2014, 4:22 PM		
Inputs	Equations	Results
<b>Boiler and Superheater</b>		
$T_{boiler\ inlet} = 30.43 \pm 0.25^\circ C$ $T_{boiler\ outlet} = 81.28 \pm 0.25^\circ C$ (saturated) $T_{superheater\ outlet} = 81.19 \pm 0.25^\circ C$ (saturated) $T_{motive\ inlet} = 81.31 \pm 0.25^\circ C$ (saturated) $\dot{Q}_{boiler} = 1889 \pm 20\ W$ $\dot{Q}_{superheater} = 334.7 \pm 5\ W$ $\dot{Q}_{loss,boiler\ line} = -19.5 \pm 5\ W$ (see Section C.1) $\dot{m}_{motive} = 0.0142 \pm 0.12\% \ kg\ s^{-1}$ $P_{boiler} = 2681 \pm 6\ kPa$	$T_{boiler\ sat} = f(P_{boiler})$ $h_{boiler\ inlet} = f(T_{boiler\ inlet}, P_{boiler})$ $\dot{m}_{motive} (h_{motive\ inlet} - h_{boiler\ inlet}) = \dot{Q}_{boiler} + \dot{Q}_{superheater} + \dot{Q}_{loss,boiler\ line}$	$T_{boiler\ sat} = 80.8 \pm 0.11^\circ C$ $T_{boiler\ outlet} - T_{boiler\ sat} = 0.48 \pm 0.36\ K$ $h_{boiler\ inlet} = 94.2 \pm 0.36\ kJ\ kg^{-1}$ $h_{motive\ inlet} = 252.2 \pm 1.5\ kJ\ kg^{-1}$
<b>Ejector</b>		
$T_{suction\ inlet} = 22.87 \pm 0.25^\circ C$ $P_{evaporator} = 468 \pm 0.2\ kPa$ $P_{condenser} = 765 \pm 0.8\ kPa$ $\dot{m}_{suction} = 0.0022 \pm 1.6\% \ kg\ s^{-1}$ $\dot{Q}_{loss,ejector} = 25.2 \pm 5\ W$ (see Section C.1)	$T_{evaporator\ sat} = f(P_{evaporator})$ $T_{condenser\ sat} = f(P_{condenser})$ $h_{suction\ inlet} = f(T_{suction\ inlet}, P_{evaporator})$ $Superheat_{suction\ inlet} = T_{suction\ inlet} - T_{evaporator\ sat}$ $\dot{m}_{motive} h_{motive\ inlet} + \dot{m}_{suction} h_{suction\ inlet} = (\dot{m}_{motive} + \dot{m}_{suction}) h_{ejector\ outlet} - \dot{Q}_{loss,ejector}$ $x_{ejector\ outlet} = f(h_{ejector\ outlet}, P_{condenser})$ $MER = \frac{\dot{m}_{suction}}{\dot{m}_{motive}}$	$T_{evaporator\ sat} = 13.62 \pm 0.01^\circ C$ $T_{condenser\ sat} = 29.76 \pm 0.04^\circ C$ $h_{suction\ inlet} = 267.0 \pm 0.24\ kJ\ kg^{-1}$ $Superheat_{suction\ inlet} = 9.3\ K \pm 0.25\ K$ $h_{ejector\ outlet} = 252.6 \pm 1.4\ kJ\ kg^{-1}$ $x_{ejector\ outlet} = 0.92 \pm 0.01$ $MER = 0.155 \pm 0.002$ $SPR = 1.638 \pm 0.002$

**Table C.2: Sample state point calculations for saturated condition given in last row of Table 5.1 for the R134a test matrix in Chapter 5.**

Cycle State Point Sample Calculation; Nov. 13, 2014, 4:22 PM		
Inputs	Equations	Results
	$SPR = \frac{P_{condenser}}{P_{evaporator}}$	
<b>Condenser</b>		
$T_{condenser\ TS\ inlet} = 29.8 \pm 0.25^\circ C$ (saturated) $T_{condenser\ TS\ outlet} = 26.3 \pm 0.25^\circ C$	$h_{condenser\ outlet} = f(T_{condenser\ outlet}, P_{condenser})$ Subcooling <sub>condenser outlet</sub> = $T_{condenser\ sat} - T_{condenser\ outlet}$ $(\dot{m}_{motive} + \dot{m}_{suction})(h_{ejector\ outlet} - h_{condenser\ outlet}) = \dot{Q}_{condenser\ line}$	$h_{condenser\ outlet} = 88.3 \pm 0.36\ kJ\ kg^{-1}$ Subcooling <sub>condenser outlet</sub> = $3.5\ K \pm 0.25\ K$ $\dot{Q}_{condenser\ line} = 2695 \pm 24.2\ W$
<b>Pump</b>		
	$\dot{W}_{pump} = \dot{m}_{motive} (h_{boiler\ inlet} - h_{condenser\ outlet})$ $v = f(T_{condenser\ outlet}, P_{condenser})$ $\eta_{pump} = \frac{v(P_{boiler} - P_{condenser})}{h_{boiler\ inlet} - h_{condenser\ outlet}}$	$\dot{W}_{pump} = 83.6 \pm 7.2\ W$ $v = 0.00083 \pm 6.7E-7\ m^3\ kg^{-1}$ $\eta_{pump} = 0.27 \pm 0.02$
<b>Evaporator</b>		
$T_{evaporator\ inlet} = 14.00 \pm 0.25^\circ C$ (saturated) $T_{evaporator\ outlet} = 22.47 \pm 0.25^\circ C$ $\dot{Q}_{evaporator} = 252.2 \pm 15\ W$	$h_{condenser\ outlet} = h_{evaporator\ inlet}$ $\dot{m}_{suction} (h_{suction\ inlet} - h_{evaporator\ inlet}) = \dot{Q}_{evaporator} + \dot{Q}_{loss, suction\ line}$	$h_{evaporator\ inlet} = 88.3 \pm 0.36\ kJ\ kg^{-1}$ $\dot{Q}_{loss, suction\ line} = 140.9 \pm 16.3\ W$
<b>Cycle Metrics</b>		
	$COP = \frac{\dot{Q}_{evaporator}}{\dot{Q}_{boiler} + \dot{Q}_{superheater}}$ $COP_{perfect\ insulation} = \frac{\dot{Q}_{evaporator} + \dot{Q}_{loss, suction\ line}}{\dot{Q}_{boiler} + \dot{Q}_{superheater} + \dot{Q}_{loss, boiler\ line}}$	$COP = 0.113 \pm 0.007$ $COP_{perfect\ insulation} = 0.178 \pm 0.010$

## APPENDIX D

### NUMERICAL MODEL CONSIDERATIONS

#### D.1 Mesh Development

For all CFD simulations, adequate attention must be given to the development of a mesh that is refined enough to capture the complex flow phenomena inside the ejector device, and provide mesh-independent results. In this work, multiple CFD models were employed for flows with different properties. In Chapter 3, 2D simulations of an air ejector with a rectangular cross-section were performed. In Chapter 4, a similar 2D rectangular cross-sectional geometry was used, but with refrigerant vapor as the working fluid instead of air. Finally, in Chapter 5, refrigerant vapor was again used as the working fluid, but a conventional circular cross-section was considered.

Despite the differences between models, the method used to generate the mesh in each case was the same. A coarse quadrilateral mesh was used to generate a general solution, and then refined to precisely capture shock and expansion flow features, as well as near-wall flow when needed. This was done using the mesh adaptation tool in ANSYS FLUENT. After convergence had been reached with the coarse mesh, it was refined twice for both gradients of static pressure ( $\sim 1000$  Pa) and Mach number ( $\sim 0.2$ ). In the cases where a  $k-\omega$  turbulence model was used, further refinement would be necessary at the ejector walls to resolve near-wall flow such that  $y^+ < 1$ . A sample refined mesh is shown in Fig. D.1, and in this case, notable refinement of the mesh can be seen at the motive nozzle throat, and at the position of the first shock at the outlet of the motive nozzle. For all CFD

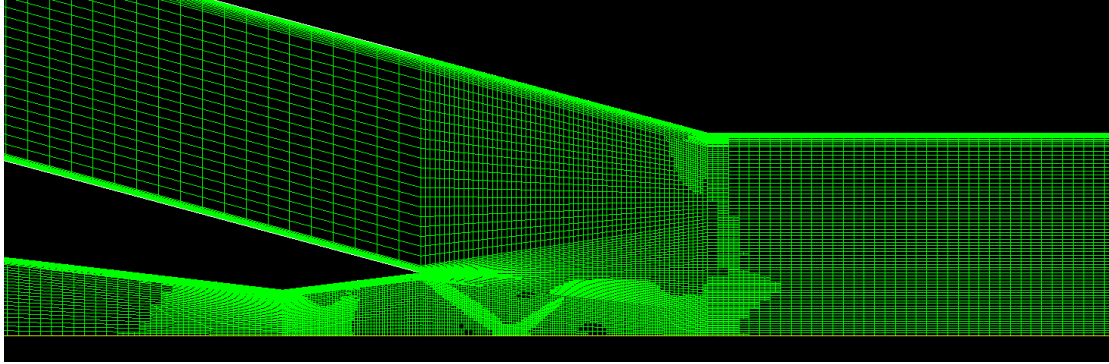


**Figure D.1: Sample mesh at the exit of the motive nozzle for the ejector from Chapter 3 operating with air in a rectangular cross-section ejector. Conditions are  $P_{\text{motive}} = 3.5$  bar,  $P_{\text{suction}} = 1$  bar, and  $P_{\text{outlet}} = 1.2$  bar using the  $k$ - $\epsilon$  RNG turbulence model. Mesh includes  $\sim 108$  k elements, and the maximum face area is  $7.5\text{E-}3$  m<sup>2</sup>.**

simulations in this work, the initial coarse meshes used ranged from  $\sim 60$ - $100$  k elements, while the refined meshes ranged from  $\sim 100$ - $130$  k elements. A check for mesh independent results was performed, with a sample shown in Figs. 3.4 and 3.5.

It should be mentioned that the computational domain used for all simulations in this work included the full length of the suction nozzle and motive nozzle. As shown in Chapter 4, flow through the motive nozzle could be predicted to a very high degree of accuracy using simple 1D equilibrium flow models for the geometry considered. Similarly, properties at the outlet of the suction nozzle could be predicted accurately. Because the majority of flow features of interest in this study occur in the mixing section and diffuser, the size of the computational domain could be significantly decreased to exclude the motive and suction nozzles. In this way, predicted nozzle outlet conditions from the 1D equilibrium model could be used as inlet parameters to the targeted domain of the mixing section and diffuser sections.

## **D.2 Three-Dimensional Flow Effects**

All simulations included in this work were performed in two dimensions. In the case of the ejectors with a circular cross-section (Chapter 5), axisymmetric simulations were performed, which made them effectively quasi-3D. But in the case of rectangular cross-section ejectors (Chapters 3 and 4), planar simulations were performed, which therefore does not address any front and back wall effects. In other work by the author (Mazzelli *et al.*, 2015), an assessment of 3D effects was performed. It was found that 3D effects are important to capture when trying to predict global inlet and outlet properties of the ejector at off-design conditions, and forthcoming work will explore the role of 3D effects on the prediction of local flow features. This discrepancy is probably due to the fact that the portion of the motive jet in contact with the front and back walls loses momentum to the walls and does not contribute to suction flow entrainment. As a result, the value of suction flow mass flow rate predicted by 2D simulations is higher than what is seen in experiments.

## **D.3 Unsteady Flow Effects**

All simulations in this work were conducted assuming steady-state conditions. This is physical for all on-design conditions, as well as most off-design conditions. At significantly off-design conditions approaching malfunction, there is some evidence of unsteady flow effects from experimental and computational work, as discussed in Mazzelli *et al.* (2015). Because this unsteady flow regime is not particularly important for most practical applications, it was not considered in this work, and therefore, temporal resolution issues were not relevant.

## REFERENCES

- Abdulateef, J.M., Sopian, K., Alghoul, M.A., Sulaiman, M.Y., 2009. Review on solar-driven ejector refrigeration technologies, *Renewable and Sustainable Energy Reviews* 13, 1338-1349.
- Al-Ansary, H.A.M., Jeter, S.M.J., 2004. Numerical and Experimental Analysis of Single-Phase and Two-Phase Flow in Ejectors., *HVAC&R Research* 10, 521-538.
- Alkislar, M.B., Krothapalli, A., Lourenco, L.M., 2003. Structure of a screeching rectangular jet: a stereoscopic particle image velocimetry study, *J. Fluid Mech.* 489, 121-154.
- Arbel, A., Sokolov, M., 2004. Revisiting solar-powered ejector air conditioner--the greener the better, *Solar Energy* 77, 57-66.
- ASHRAE, 1983. Steam-jet Refrigeration Equipment, *Equipment Handbook*.
- ASME, 1992. Gas Turbine Fuels.
- Bakhtar, F., Young, J.B., White, A.J., Simpson, D.A., 2005. Classical nucleation theory and its application to condensing steam flow calculations, *Journal of Mechanical Engineering Science* 219, 1315-1333.
- Balamurugan, S., Gaikar, V.G., Patwardhan, A.W., 2006. Hydrodynamic Characteristics of Gas-Liquid Ejectors, *Chemical Engineering Research and Design* 84, 1166-1179.
- Balamurugan, S., Lad, M.D., Gaikar, V.G., Patwardhan, A.W., 2007. Hydrodynamics and mass transfer characteristics of gas-liquid ejectors, *Chemical Engineering Journal* 131, 83-103.
- Bartosiewicz, Y., Aidoun, Z., Desevaux, P., Mercadier, Y., 2005. Numerical and experimental investigations on supersonic ejectors, *International Journal of Heat and Fluid Flow* 26, 56-70.
- Beithou, N., Aybar, H.S., 2000. A mathematical model for steam-driven jet pump, *International Journal of Multiphase Flow* 26, 1609-1619.
- Bejan, A., Vargas, J.V.C., Sokolov, M., 1995. Optimal allocation of a heat-exchanger inventory in heat driven refrigerators, *International Journal of Heat and Mass Transfer* 38, 2997-3004.
- Berana, M.S., Nakagawa, M., Harada, A., 2009. Shock Waves in Supersonic Two-Phase Flow of CO<sub>2</sub> in Converging-Diverging Nozzles, *HVAC&R Research* 15, 1081-1098.
- Bergander, M.J., 2006. Refrigeration Cycle with Two-Phase Condensing Ejector, 11th International Refrigeration and Air Conditioning Conference, West Lafayette, IN.



- Bouhanguel, A., Desevaux, P., Gavignet, E., 2011. Flow visualization in supersonic ejectors using laser tomography techniques, *International Journal of Refrigeration* 34, 1633-1640.
- Boyce, M.P., 2006. *Gas Turbine Engineering Handbook*, 3rd ed. Gulf Professional Publishing.
- Bulinski, Z., Smolka, J., Fic, A., Banasiak, K., Nowak, A.J., 2010. A comparison of heterogenous and homogenous models of two-phase transonic compressible CO<sub>2</sub> flow through a heat pump ejector, *WCCM/APCOM*. IOP.
- Butrymowicz, D., 2009. Model of Two-Phase Water-Air Ejector, International seminar on ejector/jet-pump technology and applications, Louvain-la-Neuve, Belgium.
- Carey, V.P., 2008. *Liquid-Vapor Phase-Change Phenomena : An Introduction to the Thermophysics of Vaporization and Condensation Processes in Heat Transfer Equipment*. Taylor & Francis Series Group, LLC, New York, N.Y.
- Carroll, B.F., Lopez-Fernandez, P.A., Dutton, J.C., 1993. Computations and experiments for a multiple normal shock/boundary-layer interaction, *J. Propul. Power* 9, 405-411.
- Chen, S.-L., Yen, J.-Y., Huang, M.-C., 1998. Experimental investigation of ejector performance based upon different refrigerants, *Proceedings of the 1998 ASHRAE Annual Meeting*. ASHRAE, Atlanta, GA, United States, Toronto, Canada, pp. 153-160.
- Chen, W., Liu, M., Chong, D., Yan, J., Little, A.B., Bartosiewicz, Y., 2013. A 1D model to predict ejector performance at critical and sub-critical operational regimes, *International Journal of Refrigeration* 36, 1750-1761.
- Chunnanond, K., Aphornratana, S., 2004. Ejectors: applications in refrigeration technology, *Renewable and Sustainable Energy Reviews* 8, 129-155.
- Cizungu, K., Groll, M., Ling, Z.G., 2005. Modelling and optimization of two-phase ejectors for cooling systems, *Applied Thermal Engineering* 25, 1979-1994.
- Cizungu, K., Mani, A., Groll, M., 2001. Performance comparison of vapour jet refrigeration system with environment friendly working fluids, *Applied Thermal Engineering* 21, 585-598.
- Dahmani, A., Aidoun, Z., Galanis, N., 2011. Optimum design of ejector refrigeration systems with environmentally benign fluids, *International Journal of Thermal Sciences* 50, 1562-1572.
- Deberne, N., Leone, J.F., Duque, A., Lallemand, A., 1999. A model for calculation of steam injector performance, *International Journal of Multiphase Flow* 25, 841-855.

- Desevaux, P., 2001a. Formation de nano-gouttelettes d'eau au sein d'un éjecteur à air induit: une étude qualitative par visualisation de l'écoulement, *Can. J. Chem. Eng.* 79, 273-278.
- Desevaux, P., 2001b. A method for visualizing the mixing zone between two co-axial flows in an ejector, *Optics and Lasers in Engineering* 35, 317-323.
- Desevaux, P., Lanzetta, F., 2004. Computational fluid dynamic modelling of pseudo-shock inside a zero-secondary flow ejector, *AIAA Journal* 42, 1480-1483.
- Desevaux, P., Prenel, J.P., Jacquet, P., 1994. Static Pressure Measurement Along the Centerline of an Induced Flow Ejector, *Experiments in Fluids* 16, 289-291.
- Dutton, J.C., Mikkelsen, C.D., Addy, A.L., 1982. Theoretical and Experimental Investigation of the Constant Area, Supersonic-Supersonic Ejector, *AIAA Journal* 20, 1392-1400.
- Dvorak, V., Safarik, P., 2005. Transonic instability in entrance part of mixing chamber of high-speed ejector, *Journal of Thermal Science* 14, 258-264.
- Eames, I.W., Ablwaifa, A.E., Petrenko, V., 2007. Results of an experimental study of an advanced jet-pump refrigerator operating with R245fa, *Applied Thermal Engineering* 27, 2833-2840.
- Eames, I.W., Aphornratana, S., Haider, H., 1995. A theoretical and experimental study of a small-scale steam jet refrigerator, *International Journal of Refrigeration* 18, 378-386.
- Elbel, S., 2010. Historical and present developments of ejector refrigeration systems with emphasis on transcritical carbon dioxide air-conditioning applications, *International Journal of Refrigeration* 34, 1545-1561.
- Elbel, S., Hrnjak, P., 2008. Ejector Refrigeration: An Overview of Historical and Present Developments with Emphasis on Air Conditioning Applications, 12th International Refrigeration and Air Conditioning Conference, West Lafayette, IN.
- Fabri, J., Siestrunk, R., 1958. Supersonic Air Ejectors, in: Dryden, H.L., von Karman, T. (Eds.), *Advances in Applied Mechanics*. Academic Press, New York, pp. 1-34.
- FLUENT, 2010. ANSYS, Inc., 13.0.
- Grazzini, G., Mazzelli, F., Milazzo, A., 2015. Constructural design of the mixing zone inside a supersonic ejector, *Constructural Law & Second Law Conference*, Parma, Italy.
- Grazzini, G., Milazzo, A., Paganini, D., 2012. Design of an ejector cycle refrigeration system, *Energy Conversion and Management* 54, 38-46.
- Grazzini, G., Milazzo, A., Piazzini, S., 2011. Prediction of condensation in steam ejector for a refrigeration system, *International Journal of Refrigeration* 34, 1641-1648.

- Grazzini, G., Rocchetti, A., 2002. Numerical optimisation of a two-stage ejector refrigeration plant, *International Journal of Refrigeration* 25, 621-633.
- Guo, J., Shen, H.G., 2009. Modeling solar-driven ejector refrigeration system offering air conditioning for office buildings, *Energy and Buildings* 41, 175-181.
- Hataue, I., 1989. Computational study of the shock-wave/boundary-layer interaction in a duct, *Fluid Dynamics Research* 5, 217-234.
- Hemidi, A., Henry, F., Leclaire, S., Seynhaeve, J.-M., Bartosiewicz, Y., 2009a. CFD analysis of a supersonic air ejector. Part I: Experimental validation of single-phase and two-phase operation, *Applied Thermal Engineering* 29, 1523-1531.
- Hemidi, A., Henry, F., Leclaire, S., Seynhaeve, J.-M., Bartosiewicz, Y., 2009b. CFD analysis of a supersonic air ejector. Part II: Relation between global operation and local flow features, *Applied Thermal Engineering* 29, 2990-2998.
- Huang, B.J., Chang, J.M., Wang, C.P., Petrenko, V.A., 1999. 1-D analysis of ejector performance, *International Journal of Refrigeration* 22, 354-364.
- Huang, B.J., Hu, S.S., Lee, S.H., 2006. Development of an ejector cooling system with thermal pumping effect, *International Journal of Refrigeration* 29, 476-484.
- Huang, B.J., Jiang, C.B., Hu, F.L., 1985. Ejector Performance Characteristics and Design Analysis of Jet Refrigeration System, *Journal of Engineering for Gas Turbines and Power* 107, 792-802.
- Jelinek, M., Levy, A., Borde, I., 2002. Performance of a triple-pressure-level absorption cycle with R125-N,N'-dimethylethylurea, *Applied Energy* 71, 171-189.
- John, J.E.A., 1984. *Gas Dynamics*, 2 ed. Prentice Hall, Englewood Cliffs, New Jersey.
- Keenan, J.H., Neumann, E.P., 1942. A Simple Air Ejector, *Journal of Applied Mechanics* 9, A75-A81.
- Keenan, J.H., Neumann, E.P., Lustwerk, F., 1950. An Investigation of Ejector Design by Analysis and Experiment, *Journal of Applied Mechanics* 17, 299-309.
- Korpela, S.A., 2011. *Principles of Turbomachinery*. John Wiley & Sons, Inc., Hoboken, New Jersey.
- Lear, W., Parker, G., Sherif, S., 2002. Analysis of two-phase ejectors with Fabri choking, *Proceedings of the Institution of Mechanical Engineers, Part C: Journal of Mechanical Engineering Science* 216, 607-621.
- Lemmon, E.W., Span, R., 2006. Short Fundamental Equations of State for 20 Industrial Fluids, *Journal of Chemical and Engineering Data* 51, 785-850.

- Levy, A., Jelinek, M., Borde, I., 2002. Numerical study on the design parameters of a jet ejector for absorption systems, *Applied Energy* 72, 467-478.
- Lin, P., Rao, G.V.R., O'Connor, G.M., 1991a. Numerical analysis of normal shock train in a constant area isolator, AIAA Paper No. 91-2162.
- Lin, P., Rao, G.V.R., O'Connor, G.M., 1991b. Numerical investigation on shock wave/boundary layer interactions in a constant area diffuser at Mach 3, AIAA Paper No. 91-1766.
- Little, A., Bartosiewicz, Y., Garimella, S., 2012. Optical Validation of Ejector Flow Characteristics Predicted by Computational Analysis, ASME International Mechanical Engineering Congress & Exposition, Houston, Texas.
- Little, A., Garimella, S., 2015. Ejector Refrigeration Systems for Waste Heat Recovery Applications: Effects of Condensation on Performance, 24th IIR International Congress of Refrigeration, Yokohama, Japan.
- Little, A.B., Bartosiewicz, Y., Garimella, S., 2015. Visualization and Validation of Ejector Flow Field with Computational and First-Principles Analysis, *Journal of Fluids Engineering* 137.
- Little, A.B., Garimella, S., DiPrete, J.P., 2016. Combined Effects of Fluid Selection and Flow Condensation on Ejector Operation in an Ejector-Based Chiller, *Applied Thermal Engineering* In review.
- Liu, F., 2014. Review on Ejector Efficiencies in Various Ejector Systems, International Refrigeration and Air Conditioning Conference, Purdue.
- Liu, F., Groll, E.A., 2008. Analysis of Two Phase Flow Ejector for the Transcritical CO<sub>2</sub> Cycle, 12th International Refrigeration and Air Conditioning Conference West Lafayette, IN.
- Marsano, F., Magistri, L., Massardo, A.F., 2004. Ejector performance influence on a solid oxide fuel cell anodic recirculation system, *Journal of Power Sources* 129, 216-228.
- Matsuo, K., Miyazato, Y., Kim, H.-D., 1999. Shock train and pseudo-shock phenomena in internal gas flows, *Progress in Aerospace Sciences* 35, 33-100.
- Matsuo, K., Sasaguchi, K., Kiyotoki, Y., Mochizuki, H., 1982. Investigation of supersonic air ejectors, Part 2, Effects of throat-area-ratio on ejector performance, *Bulletin of Japan Society of Mechanical Engineers* 25, 1898-1905.
- Mazzelli, F., Little, A.B., Garimella, S., Bartosiewicz, Y., 2015. Computational and Experimental Analysis of Supersonic Air Ejector: Turbulence Modeling and Assessment of 3D Effects, *International Journal of Heat and Fluid Flow*.

- Moreno, D., Krothapalli, A., Alkisar, M.B., Lourenco, L.M., 2004. Low-dimensional model of a supersonic rectangular jet, *Physical Review E* 69.
- Munday, J.T., Bagster, D.F., 1977. A New Ejector Theory Applied to Steam Jet Refrigeration, *Industrial & Engineering Chemistry, Process Design and Development* 16, 442-449.
- Nakagawa, M., Berana, M.S., Kishine, A., 2009. Supersonic two-phase flow of CO<sub>2</sub> through converging-diverging nozzles for the ejector refrigeration cycle, *International Journal of Refrigeration* 32, 1195-1202.
- Nguyen, V.M., Riffat, S.B., Doherty, P.S., 2001. Development of a solar-powered passive ejector cooling system, *Applied Thermal Engineering* 21, 157-168.
- Ouzzane, M., Aidoun, Z., 2003. Model development and numerical procedure for detailed ejector analysis and design, *Applied Thermal Engineering* 23, 2337-2351.
- Papamoschou, D., Roshko, A., 1988. The compressible turbulent shear layer: An experimental study, *Journal of Fluid Mechanics* 197, 453-477.
- Pollerberg, C., Heinzl, A., Weidner, E., 2009. Model of a solar driven steam jet ejector chiller and investigation of its dynamic operational behaviour, *Solar Energy* 83, 732-742.
- Rao, S.M.V., Jagadeesh, G., 2014. Observations on the non-mixed length and unsteady shock motion in a two dimensional supersonic ejector, *Physics of Fluids* 26, 036103.
- Rogdakis, E.D., Alexis, G.K., 2000. Design and parametric investigation of an ejector in an air-conditioning system, *Applied Thermal Engineering* 20, 213-226.
- Saad, M.A., 1993. *Compressible Fluid Flow*, 2nd ed. Prentice-Hall, Inc., Englewood Cliffs, New Jersey.
- Scarano, F., 2008. Overview of PIV in Supersonic Flows, *Topics in Applied Physics* 112, 445-463.
- Settles, G.S., 2001. *Schlieren and Shadowgraph Techniques*. Springer, New York.
- Sokolov, M., Hershgal, D., 1990a. Enhanced ejector refrigeration cycles powered by low grade heat. Part 1. Systems characterization, *International Journal of Refrigeration* 13, 351-356.
- Sokolov, M., Hershgal, D., 1990b. Enhanced ejector refrigeration cycles powered by low grade heat. Part 2. Design procedures, *International Journal of Refrigeration* 13, 357-363.
- Sokolov, M., Hershgal, D., 1991. Enhanced ejector refrigeration cycles powered by low grade heat. Part 3. Experimental results, *International Journal of Refrigeration* 14, 24-31.

- Srisastra, P., Aphornratana, S., 2005. A circulating system for a steam jet refrigeration system, *Applied Thermal Engineering* 25, 2247-2257.
- Srisastra, P., Aphornratana, S., Sriveerakul, T., 2008. Development of a circulating system for a jet refrigeration cycle, *International Journal of Refrigeration* 31, 921-929.
- Stoecker, W.F., 1958. *Refrigeration and Air-conditioning*. McGraw-Hill, New York, NY.
- Sun, D.-W., Eames, I.W., 1995. Recent developments in the design theories and applications of ejectors - a review, *Journal of the Institute Energy* 68, 65-79.
- Tillner-Roth, R., Baehr, H.D., 1994. An International Standard Formulation for the Thermodynamic Properties of 1,1,1,2-Tetrafluoroethane (HFC-134a) for Temperatures From 170 K to 455 K and Pressures up to 70 MPa, *Journal of Physical and Chemical Reference Data* 23, 657-729.
- Tischendorf, C., Lucas, C., Koehler, J., Tegethoff, W., 2010. Visual Investigation of an Ejector Motive Nozzle, *International Mechanical Engineering Congress & Exposition, Vancouver, British Columbia*.
- Wang, J.H., Wu, J.H., Hu, S.S., Huang, B.J., 2009. Performance of ejector cooling system with thermal pumping effect using R141b and R365mfc, *Applied Thermal Engineering* 29, 1904-1912.
- Wynanski, I., Fiedler, H.E., 1970. The two-dimensional mixing region, *Journal of Fluid Mechanics* 41.
- Yamane, R., Oshima, S., Nakamura, Y., Ishii, T., Park, M.K., 1995. Numerical simulation of pseudo-shock in straight channels, *JSME International Journal Series B* 38, 549-554.
- Yapici, R., Yetisen, C.C., 2007. Experimental study on ejector refrigeration system powered by low grade heat, *Energy Conversion and Management* 48, 1560-1568.
- Yu, J., Ren, Y., Chen, H., Li, Y., 2007. Applying mechanical subcooling to ejector refrigeration cycle for improving the coefficient of performance, *Energy Conversion and Management* 48, 1193-1199.
- Zare-Behtash, H., Gongora-Orozco, N., Kontis, K., 2011. Effect of primary jet geometry on ejector performance: A cold-flow investigation, *International Journal of Heat and Fluid Flow* 32, 596-607.
- Zhu, Y., Cai, W., Wen, C., Li, Y., 2007a. Fuel ejector design and simulation model for anodic recirculation SOFC system, *Journal of Power Sources* 173, 437-449.
- Zhu, Y., Cai, W., Wen, C., Li, Y., 2007b. Shock circle model for ejector performance evaluation, *Energy Conversion and Management* 48, 2533-2541.

Zhu, Y., Cai, W., Wen, C., Li, Y., 2009. Numerical investigation of geometry parameters for design of high performance ejectors, *Applied Thermal Engineering* 29, 898-905.